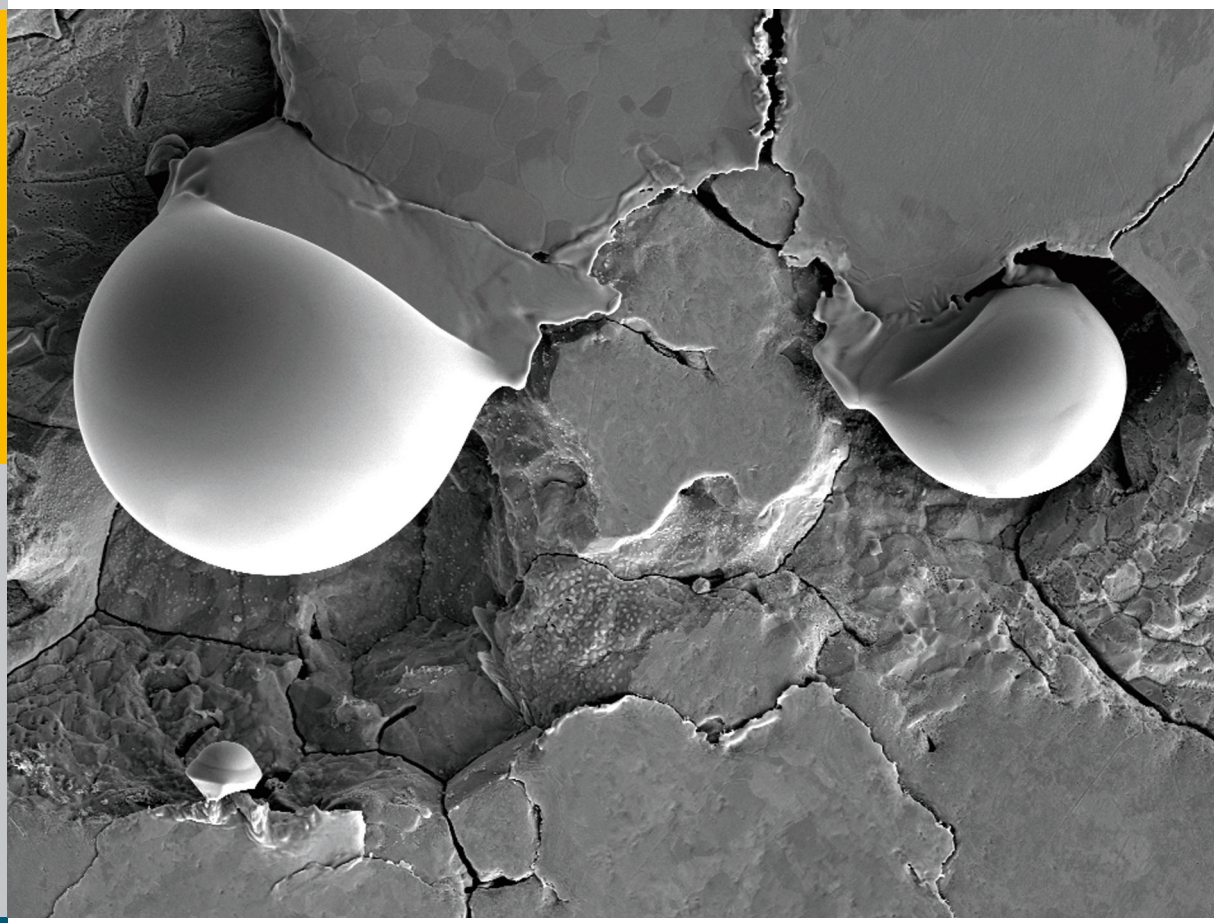
Performance of Plasma Facing Materials under Thermal and Plasma Exposure

Isabel Steudel



Mitglied der Helmholtz-Gemeinschaft

Energie & Umwelt / Energy & Environment
Band / Volume 370
ISBN 978-3-95806-226-9

JÜLICH
FORSCHUNGSZENTRUM

Schriften des Forschungszentrums Jülich
Reihe Energie & Umwelt / Energy & Environment Band / Volume 370

Forschungszentrum Jülich GmbH
Institute of Energy and Climate Research (IEK)
Microstructure and Properties of Materials (IEK-2)

Performance of Plasma Facing Materials under Thermal and Plasma Exposure

Isabel Steudel

Schriften des Forschungszentrums Jülich
Reihe Energie & Umwelt / Energy & Environment Band / Volume 370

ISSN 1866-1793 ISBN 978-3-95806-226-9

Bibliographic information published by the Deutsche Nationalbibliothek.
The Deutsche Nationalbibliothek lists this publication in the Deutsche
Nationalbibliografie; detailed bibliographic data are available in the
Internet at http://dnb.d-nb.de.

Publisher and Distributor: Forschungszentrum Jülich GmbH
Zentralbibliothek
52425 Jülich
Tel: +49 2461 61-5368
Fax: +49 2461 61-6103
Email: zb-publikation@fz-juelich.de
www.fz-juelich.de/zb

Cover Design: Grafische Medien, Forschungszentrum Jülich GmbH

Printer: Grafische Medien, Forschungszentrum Jülich GmbH

Copyright: Forschungszentrum Jülich 2017

Schriften des Forschungszentrums Jülich
Reihe Energie & Umwelt / Energy & Environment, Band / Volume 370

D 82 (Diss. RWTH Aachen University, 2017)

ISSN 1866-1793
ISBN 978-3-95806-226-9

The complete volume is freely available on the Internet on the Jülicher Open Access Server (JuSER)
at www.fz-juelich.de/zb/openaccess.



This is an Open Access publication distributed under the terms of the Creative Commons Attribution License 4.0,
which permits unrestricted use, distribution, and reproduction in any medium, provided the original work is properly cited.

List of symbols and abbreviations

Symbols

ΔT	Temperature rise	[K]
Δt	Pulse duration	[s]
ϵ	Absorption coefficient for electrons	[-]
λ	Thermal conductivity	$[WK^{-1}m^{-1}]$
μ	Poisson´s ratio	[-]
ν	Frequency	[Hz]
ρ	Density	$[kgm^{-3}]$
σ	Nuclear cross section	[barn]
τ_E	Energy confinement time	[s]
F_{HF}	Factor of heat flux	$[MWm^{-2}s^{1/2}]$
R_a	Arithmetic mean roughness	[µm]
a	Thermal diffusivity	$[m^2s^{-1}]$
C	Heat capacity	$[JK^{-1}]$
c	Speed of light	$[ms^{-1}]$
c_p	Specific heat capacity	$[Jkg^{-1}K^{-1}]$
d	Distance	[m]
I	Current	[A]
I_{abs}	Absorbed current	[A]
I_{inc}	Incident current	[A]
K_D	Kinetic energy	$[kgm^2s^{-2}]$

K_x	Correlation constant	[-]
m	Mass	[kg]
n	Ion density	[m^{-3}]
n_e	Electron density	[m^{-3}]
P	Power	[W]
P_{abs}	Absorbed power density	[Wm^{-2}]
S	Area	[m^2]
T	Temperature	[K]
t	Time	[s]
T_1	Correction factor	[-]
T_e	Electron temperature	[eV]
U_a	Acceleration voltage	[V]

Abbreviations

BCC	Body Centered Cubic
BSE	Backscattered Electron
DBTT	Ductile-to-Brittle Transition Temperature
EBSD	Electron Backscattered Diffraction
EDM	Electric Discharge Machining
EDX	Energy-Dispersive X-ray
EHF	Enhanced Heat Flux
ELM	Edge Localized Mode
FIB	Focused Ion Beam
FM	Ferritic Martensitic
FW	First Wall
FWHM	Full-Width-Half-Maximum
HIP	Hot Isostatic Pressing
IPF	Inverse Pole Figure

JET	Joint European Torus
JUDITH	Juelicher Divertor Test Facility in Hot Cells
L	Longitudinal Grain Structure (in loading direction)
LM	Light Microscopy
MGI	Massive Gas Injection
MHD	Magnetohydrodynamics
NHF	Normal Heat Flux
ODS	Oxide Dispersion Strengthened
PFC	Plasma Facing Component
PFM	Plasma Facing Material
PSI	Plasma Surface Interaction
QMB	Quartz Microbalance
R	Recrystallised Grain Structure
RAFM	Reduced Activation Ferritic Martensitic
RE	Runaway Electron
RT	Room Temperature
SE	Secondary Electron
SEM	Scanning Electron Microscopy
SOL	Scrape-Off Layer
SPI	Shattered Pellet Injection
T	Transversal Grain Structure (in loading direction)
VDE	Vertical Displacement Event
WT%	Weight Percentage

List of publications

Parts of the results presented in this work have already been published in the following articles:

I. Steudel, A. Huber, J. Linke, G. Sergienko, M. Wirtz; Thermal Shock Behaviour of Tungsten Under Different Simulation Methods; *Proceedings of the 45th Annual Meeting on Nuclear Technology* art. no. 9287 (6pp), (2014)

A. Huber, A. S. Arakcheev, G. Sergienko, I. Steudel, M. Wirtz, A. V. Burdakov, J. W. Coenen, A. Kreter, J. Linke, Ph. Mertens; Investigation of the impact of transient heat loads applied by laser irradiation on ITER-grade tungsten; *Physica Scripta* T159, (2014).

A. Huber, M. Wirtz, G. Sergienko, I. Steudel, A. S. Arakcheev, A. V. Burdakov, G. Esser, M. Freisinger, A. Kreter, J. Linke, Ch. Linsmeier, Ph. Mertens, S. Möller, V. Philipps, G. Pintsuk, M. Reinhart, B. Schweer, A. A. Shoshin, A. Terra, B. Unterberg; Combined Impact of Transient Heat Loads and Steady-State Plasma Exposure on Tungsten; *Fusion Engineering and Design* 98-99, pp. 1328-1332 (2015).

I. Steudel, J. Linke, Th. Loewenhoff, G. Pintsuk, R. A. Pitts, M. Wirtz; Melt layer formation in stainless steel under transient thermal loads; *Journal of Nuclear Materials* 463, pp. 731-734 (2015).

M. Wirtz, S. Bardin, A. Huber, A. Kreter, J. Linke, T.W. Morgan, G. Pintsuk, M. Reinhart, G. Sergeinko, I. Steudel, G. De Temmerman, B. Unterberg; Impact of combined hydrogen and transient heat load exposure on the performance of tungsten as PFM; *Nuclear Fusion* 55 no. 12, art. no. 123017 (2015).

A. S. Arakcheev, A. Huber, M. Wirtz, G. Sergienko, I. Steudel, A. V. Burdakov, J. W. Coenen, A. Kreter, J. Linke, Ph. Mertens, V. Philipps, G. Pintsuk, M. Reinhart, U. Samm, A. A. Shoshin, B. Schweer, B. Unterberg, A. A. Vasilyev; Theoretical investigation of crack formation in tungsten after heat loads; *Journal of Nuclear Materials* 463, 246-249 (2015).

I. Steudel, A. Huber, A. Kreter, J. Linke, G. Sergienko, B. Unterberg, M. Wirtz; Sequential and Simultaneous Thermal and Particle Exposure of Tungsten; *Physica Scripta* T167, 014053 (2016).

A. Huber, G. Sergienko, M. Wirtz, I. Steudel, A. S. Arakcheev, S. Brezinsek, A. Burdakov, T. Dittmar, H. G. Esser, A. Kreter; Impact on the deuterium retention of simultaneous exposure of tungsten to a steady state plasma and transient heat cycling loads; *Physica Scripta* T167, 014046 (2016).

I. Steudel, A. Huber, A. Kreter, J. Linke, G. Sergienko, B. Unterberg, M. Wirtz; Melt-layer formation on PFMs and the consequences for the material performance; *Nuclear Materials and Energy* Volume 9, 153-156 (2016).

A. Huber, G. Sergienko, M. Wirtz, I. Steudel, A. Arakcheev, S. Brezinsek, A. Burdakov, T. Dittmar, H.G. Esser, M. Freisinger, A. Kreter, J. Linke, Ch. Linsmeier, Ph. Mertens, S. Möller, M. Reinhart, A. Terra, B. Unterberg; Deuterium retention in tungsten under combined high cycle ELM-like heat loads and steady-state plasma exposure; *Nuclear Materials and Energy* Volume 9, 157-164 (2016).

I. Steudel, A. Huber, A. Kreter, J. Linke, G. Sergienko, B. Unterberg, M. Wirtz; Influence of the base temperature on the performance of tungsten under thermal and particle exposure; *Nuclear Materials and Energy* (under review), (submitted June 2016).

Kurzfassung

Thermonukleare Fusion stellt eine vielversprechende saubere und sichere Energiequelle dar, die den weltweit wachsenden Energiebedarf decken und Energieversorgungsproblemen entgegenwirken könnte. In den vergangenen Jahrzehnten wurde zielstrebig an diesem ambitionierten Projekt, die Fusion als Energiequelle nutzbar zu machen, gearbeitet und der Bau des experimentellen Fusionsreaktors ITER (lat.: der Weg) in Cadarache, Südfrankreich, repräsentiert hierbei einen wichtigen Schritt bei der Erreichung dieses Ziels. ITER soll die wissenschaftliche und technische Realisierbarkeit der Kernfusion demonstrieren und alle Schlüsseltechnologien erproben, die für den nächsten Schritt, einen Prototyp eines Fusionsreaktors (DEMO), und schlussendlich die kommerzielle Nutzung der Kernfusion notwendig sind. Dies beinhaltet, dass die Plasma-Wand-Materialien für Applikationen innerhalb der Plasmakammer extremen Wärmeflüssen, volumetrischer Aufheizung durch Neutronen und Neutronenaktivierung, Plasmabelastung (hauptsächlich Wasserstoffisotope und Helium), elektromagnetischer Belastung standhalten und den Umwelt- und Sicherheitsanforderungen etc. gerecht werden müssen. Geeignete Kandidaten sind hierbei Beryllium (ITER), Wolfram (ITER und DEMO), sowie gegebenenfalls ferritisch martensitische Stähle (DEMO).

Dies als Grundlage nehmend wurden im Rahmen dieser Arbeit zwei Materialien, Wolfram und Stahl, ITER und DEMO relevanten Wärme- und Teilchenflüssen ausgesetzt und deren Auswirkungen aus materialwissenschaftlicher Sicht untersucht. Aufbauend auf den Resultaten vorangegangener Arbeiten wurde reines Wolfram im Plasmagenerator PSI-2 sequentiell als auch gleichzeitig transienten thermischen Belastungen und Wasserstoff- bzw. Wasserstoff-Helium Plasma ausgesetzt. Durchgeführt wurden die Experimente bei Basistemperaturen von 400 °C und 730 °C mit absorbierten Leistungsdichten bis zu 0,76 GW/m², einer Pulsdauer von 1 ms und einer maximalen Pulsanzahl von 1000 Pulsen, um ein möglichst weites Spektrum an Belastungsbedingungen im Rahmen der zur Verfügung stehenden Experimentierzeit an der Testanlage abzudecken. Aufgrund dieser Untersuchungen konnte gezeigt werden, dass die Mikrostruktur, die Belastungsreihenfolge und die Belastungsparameter einen erheblichen Einfluss auf die Oberflächenveränderungen und das Schädigungsverhalten ausüben und darüber hinaus, dass Deuterium und Helium die Materialeigenschaften und damit die Belastungsgrenzen von Wolfram wesentlich herabsetzen.

Des Weiteren wurden Hochpulstests ($\leq$ 100.000 Pulse) mit einer absorbierten Leistungsdichte von 0,38 GW/m² bei gleichzeitiger Wasserstoff-Helium Plasmabelastung

zur Untersuchung von Ermüdungseffekten an Wolfram durchgeführt. Diese führten nicht nur zu enormen plastischen Verformungen, Mikrostrukturumwandlungen wie Subkornentstehung und Rekristallisation sondern auch zur Entstehung von Nanostrukturen und Heliumbläschen unterhalb der Probenoberfläche. In Bezug auf ITER mit mehr als 10^6 erwarteten transienten Ereignissen deuten diese Ergebnisse schwerwiegende Beeinträchtigungen des Betriebs der Anlage und der plasmabegrenzenden Bauteile an.

Neben den bereits beschriebenen Experimenten an Wolfram wurden aufeinander aufbauende Experimente an ferritisch martensitischem Stahl P92 durchgeführt. Mit Hilfe der Elektronenstrahlanlage JUDITH 1 wurde die Oberfläche von Proben bei Raumtemperatur aufgeschmolzen und anschließend am Plasmagenerator PSI-2 sequentiell und gleichzeitig mit Laser und Deuteriumplasma beaufschlagt, um die Auswirkungen von vorgeschädigten Oberflächen auf das Leistungsvermögen und Schädigungsverhalten zu erforschen. Die Erkenntnisse dieser Tests verdeutlichen, dass je nach Vorschädigung der Oberfläche das Schädigungsverhalten signifikant beeinflusst wird, was zu vorzeitigen Ermüdungseffekten und somit zum Versagen von plasmabegrenzenden Bauteilen führen kann.

Die im Rahmen dieser Arbeit ausgearbeiteten und durchgeführten Experimente ergaben, dass das Schädigungsverhalten von Wolfram äußerst komplex ist und durch eine Vielzahl von Parametern beeinflusst wird. Die Auswirkungen von thermischen Belastungen in Kombination mit Teilchenflüssen sowie einer hohen Anzahl von transienten Ereignissen konnten sehr gut mit Hilfe des Plasmagenerators PSI-2 simuliert und charakterisiert werden. So wurden der Einfluss der Mikrostruktur auf die Rissbildung und -ausbreitung sowie der Einfluss von Wasserstoff bzw. Helium auf das Thermoshockverhalten ausgearbeitet. Durch die schrittweise Annäherung an die zu erwartenden Bedingungen in einem Fusionsreaktor konnte eine detaillierte Übersicht über die Einflüsse der einzelnen Belastungsparameter und die zu erwartenden Schädigungen des Materials abgeleitet werden. Die Ergebnisse der Stahlexperimente haben gezeigt, dass eine Vorschädigung der Oberfläche das Schädigungsverhalten massiv beeinflusst und somit die Lebensdauer der plasmabegrenzenden Bauteile beachtlich herabsetzen könnte. Die in dieser Arbeit festgestellten Schädigungen und Oberflächenveränderungen zeigen deutlich die Risiken für einen reibungslosen Betrieb zukünftiger Fusionsanlagen wie ITER und DEMO auf, bieten jedoch auch einen Ansatzpunkt zur Optimierung und Weiterentwicklung von fusionsrelevanten Materialien.

Abstract

A relatively clean, safe, and promising solution to cover the globally increasing energy demand but also to avoid energy supply problems could be nuclear fusion. In recent decades, this ambitious project, to make energy generation via fusion possible, demanded a lot of work and the construction of the experimental fusion reactor ITER (latin for ″the way‟) in Cadarache, South France, plays an important role to the next big step forward. ITER, a large scale experiment, will demonstrate the scientific and technological feasibility of nuclear fusion and should test all key technologies that are necessary for the next steps, which will be a demonstration power plant (DEMO) and finally a commercial fusion power plant. Furthermore, potential plasma facing materials (PFMs) for in-vessel components have to sustain heat fluxes, neutronic volumetric heating and neutron activation, electromagnetic loads, and environment and safety requirements just to list the most significant ones. At this time beryllium and tungsten are the PFMs in ITER, for DEMO it could be ferritic martensitic steel in addition to tungsten.

In this context, this work examines two materials, tungsten und stainless steel, from the material scientific point of view under ITER and DEMO relevant heat and particle fluxes. Building on the results of former works, pure tungsten was exposed in the linear plasma device PSI-2 to sequential and simultaneous transient thermal loads with absorbed power densities up to 0.76 GW/m² and pure deuterium plasma and deuterium plasma with 6 % helium content, respectively. Furthermore, base temperatures of 400 °C and 730 °C were used and the pulse number was limited to a maximum of 1000 to cover a wide range of loading conditions within the available machine time. The results of this campaign identified that the microstructure, the order of exposure as well as the loading parameters have a substantial impact on the surface modification and damage behaviour and furthermore, that deuterium and helium exacerbates the material performance considerably.

In addition, high pulse number tests ($\leq 100,000$ pulses) with deuterium plasma background and an absorbed power density of 0.38 GW/m² were executed to quantify fatigue effects. These experiments led not only to tremendous plastic deformations, microstructural changes like subgrain formation and recrystallisation, but also to the formation of nanostructures and helium induced bubbles below the sample surface. In matters of ITER, where more than 10^6 transient events are expected, these results indicate severe disturbances of the operation as well as detractions of plasma facing components (PFCs).

Beside the sequential and simultaneous experiments on tungsten, the electron beam facility JUDITH 1 was used to create molten/solidified surfaces on ferritic martensitic steel P92 samples, which were afterwards sequentially and simultaneously exposed to laser pulses and deuterium plasma at PSI-2, to analyse the impact of preloaded surfaces on the material performance and damage behaviour. The results showed that dependent on the pre-damage the performance and damage behaviour was significantly influenced, which could accelerate fatigue effects and, therefore, shorten the lifetime of PFCs or lead to a complete failure.

The experiments, which were elaborated and executed in the frame of this work exhibited that the damage behaviour of tungsten is extremely complex and influenced by a large number of parameters. The impact of thermal loads in combination with particles fluxes as well as the effect of a high number of transient thermal events was beneficially simulated and characterised by the linear plasma generator PSI-2. The influence of the microstructure on the crack formation and propagation was revealed just as the exacerbating effect of deuterium and helium on the thermal shock behaviour. Due to the gradual approach to the expected conditions within a fusion device, a detailed summary about the individual impacts of single exposure parameters and the consequential material damages was elaborated. The results of the steel tests showed that the preloading had a massive influence on the damage behaviour, which could reduce the lifetime of PFCs significantly. In conclusion, the results of this work, regarding the investigated surface modifications and damages, illustrated considerably the risks for a smooth operation of future fusion devices like ITER and DEMO but provide also starting points for improvement and further development of fusion relevant materials.

Contents

1 Introduction **1**

1.1 Nuclear fusion . . . 3

1.2 Tokamak . . . 5

1.3 Plasma wall interaction . . . 9

1.4 Plasma facing materials . . . 13

1.5 Scope of work . . . 17

2 Materials **21**

2.1 Tungsten . . . 21

2.2 9-12%Cr ferritic martensitic steels . . . 24

3 Research facilities and analysing techniques **27**

3.1 JUDITH 1 . . . 27

3.2 PSI-2 . . . 30

3.3 Analysing techniques . . . 34

3.3.1 Laser profilometry . . . 34

3.3.2 Scanning electron microscopy (SEM) . . . 34

3.3.3 Electron backscatter diffraction (EBSD) . . . 34

3.3.4 Focused ion beam (FIB) . . . 35

3.3.5 Metallography . . . 35

4 Performance of tungsten under normal operation scenarios **37**

4.1 Summary of previous experiments . . . 37

4.1.1 Results of the electron beam tests . . . 38

4.1.2 Results of the laser beam tests . . . 38

4.2 Sequential and simultaneous experiments with deuterium plasma . . . 39

4.2.1 Sequential and simultaneous tests at 400 °C 40
4.2.2 Sequential and simultaneous tests at 730 °C 51
4.3 Sequential and simultaneous experiments with deuterium helium (6 %) plasma 59
4.3.1 Sequential and simultaneous tests at 400 °C 59
4.3.2 Sequential and simultaneous tests at 730 °C 68
4.4 Summary and conclusion 77
4.5 High pulse number experiments 82
4.5.1 Results and discussion 83
4.5.2 Conclusion 97

5 Performance of steel under off-normal events 101
5.1 Melting experiments in JUDITH 1 101
5.1.1 Results and discussion 102
5.2 Subsequent sequential and simultaneous tests at PSI-2 104
5.2.1 Results and discussion 105
5.3 Conclusion 109

6 Overall conclusion and outlook 111

A Appendix: Detailed measurement results of sequential and simultaneous tests 115
A.1 Tests with deuterium plasma at 400 °C 115
A.2 Tests with deuterium plasma at 730 °C 116
A.3 Tests with deuterium helium(6 %) plasma at 400 °C 119
A.4 Tests with deuterium helium(6 %) plasma at 730 °C 120

B Appendix: Detailed analysis results of sequential and simultaneous tests 123
B.1 Tests with deuterium plasma at 400 °C 123
B.2 Tests with deuterium plasma at 730 °C 125
B.3 Tests with deuterium helium(6 %) plasma at 400 °C 127
B.4 Tests with deuterium helium(6 %) plasma at 730 °C 129

C Appendix: Detailed measurement results of high pulse number tests **131**

D Appendix: Detailed measurement results of tests on steel **133**

D.1 Melting tests at JUDITH 1 133

D.2 Subsequent sequential and simultaneous tests at PSI-2 133

Bibliography **135**

1 Introduction

The immense daily energy consumption not least due to the technological and economical progress forces governments and scientists to find suitable solutions for potential energy supply problems in the future. If nothing else, the limitation of accessible and available fossil fuels converts the energy supply into one of the exceedingly important topics of the century. Furthermore, not only the limitation of fossil fuels but also the correlation between the combustion and the environmental pollution and its consequences is another vital aspect, which has to be kept in sight.

Certainly, even if a big percentage of the available power today is coming from non sustainable resources, i.e. from the burning of fossil fuels, it is not the only energy source. Equally, nuclear fission contributes a significant amount of energy to the overall power supply. Indeed, the serious problem with nuclear fission is the highly radioactive waste, which is produced albeit and has to be stored for thousands of years. Another disadvantage is that an accident, independent of the catalyst, which could be malfunction, natural disasters, or terrorism, would have disastrous consequences for mankind and nature. On these grounds, the federal government of germany decided that a change of energy supply is urgently required and inevitable. The keypoints of this energy transition are the decommissioning of nuclear power plants in stages by the end of 2022, the extension and promotion of the use of renewable energy sources so that they occupy the largest share in the future energy mix in Germany, the energy research not least for higher efficiency, and the mitigation of climate change by secure and environmentally friendly energy suppliers.

As it turned out above, renewable energies are one big alternative concerning the energy supply. Equally, fission, although only for a limited time according to the energy transition plan, will still be used for energy production. However, none of them can redress the energy problems by itself but there is another alternative, videlicet nuclear fusion. Of course, fusion is the least developed technology but nevertheless, it is a potential source of safe, non-carbon emitting, and virtually limitless energy [1]. And that is the reason why fusion is one of the most promising alternative.

This work illuminates and studies nuclear fusion from the point of view of material

science by investigating materials for applications in future fusion devices under the expected environmental conditions. Thereby, this work does one's bit to the advancement of fusion towards a commercially usable energy source.

1.1 Nuclear fusion

A nucleus consists of protons and neutrons, which are bound together due to the highly attractive strong force. The strong nuclear force is intensive at very short distances, at greater distances the electrostatic force dominates. In addition, the mass of the nucleus is less than the sum of the masses of its single components. This difference Δm_K is called mass defect. By using Albert Einstein's formula of the equivalence of energy and mass $E = mc^2$, it can be seen that the difference in mass corresponds to the binding energy. Moreover, this implies that the bigger the mass defect of the nucleus and as a consequence the binding energy per nucleon is, the more stable the nucleus becomes because more energy must be injected to separate the system of particles into its single constituents. However, ^{62}Ni has the maximum binding energy per nucleon as figure 1.1 illustrates and consequentially all nuclei lighter than ^{62}Ni release energy by fusion and the heavier ones by fission [2].

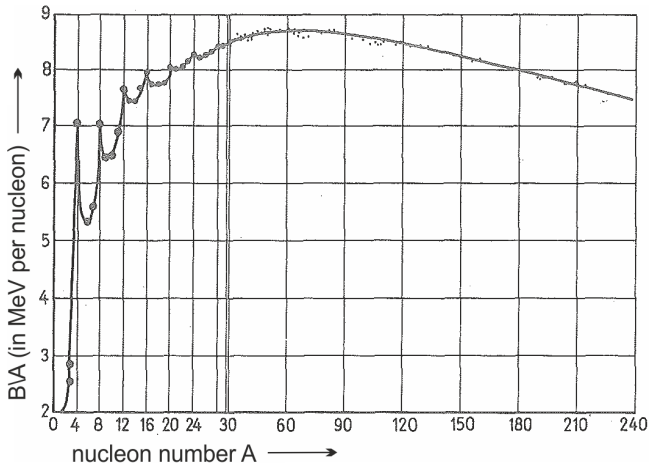


Figure 1.1: Schematic illustration [3] of the binding energy per nucleon B/A as a function of the nucleon number A. The abscissa is spread from A = 30. Nuclei lighter than ^{62}Ni release energy by fusion, the heavier ones by fission [2].

Before fusion can occur, the Coulomb-barrier between the positively charged nuclei must be overcome. For example, in a deuterium-tritium fusion reaction, 0.1 MeV of energy is necessary to overcome this barrier. Therefore, the nuclei need enough kinetic energy or nearly enough energy to tunnel through the remaining barrier (quantum tunneling) [3]. The required kinetic energy will be reached by exterior energy input. In detail, temperatures of several million degree celsius are needed to heat the matter sufficiently. As a consequence, the atoms will be seperated in unbound electrons and nuclei, which leads to the formation of an ionised gas, a so

called plasma. The nuclear fusion reaction that is the most interesting and promising for terrestial fusion is the reaction between deuterium ^{2}H (heavy hydrogen) and tritium ^{3}H (super heavy hydrogen) due to the highest reaction rate at a relatively low temperature. The cross section of this reaction is ten times bigger than for example for the reaction of deuterium and deuterium at the same temperature. The two hydrogen isotopes deuterium and tritium form an intermediate state ^{5}H (half life time $\sim 5.5 \cdot 10^{-22}$ s) [4] that decomposes into a helium nucleus with a kinetic energy of 3.5 MeV and a neutron with 14.1 MeV. The associated equation as well as a schematic illustration can be found in figure 1.2.

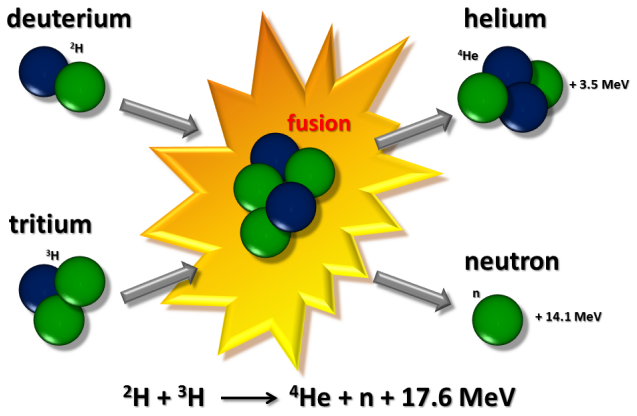


Figure 1.2: The fusion reaction of deuterium and tritium generates a helium nucleus, a free neutron, and releases 17.6 MeV of energy. The neutron can be used for tritium breeding from lithium and for electricity generation from heat conversion.

Deuterium, the second most common stable hydrogen isotope is abundant in nature. For example, 33 g of deuterium can be found in every cubic metre of water [5]. Tritium is not stable (half life time $\sim$ 12 a) and has to be produced from lithium. The two technically feasible reactions of tritium breeding are [6]:

$$^6\mathrm{Li} + \mathrm{n} \rightarrow ^4\mathrm{He} + \mathrm{T} + 4.8\ \mathrm{MeV} \tag{1.1}$$

$$^7\mathrm{Li} + \mathrm{n} \rightarrow ^4\mathrm{He} + \mathrm{T} + \mathrm{n} - 2.5\ \mathrm{MeV} \tag{1.2}$$

The exothermic reaction between ^{6}Li and a slow neutron releases 4.8 MeV of energy, whereas the ^{7}Li reaction with a fast neutron is endothermic and absorbes 2.5 MeV.

The requirements, which have to be fulfilled in order to reach ignition, the point where the nuclear fusion reaction becomes self-sustaining, are that the heating by the products of the fusion reaction is adequate to maintain the temperature of the plasma without external input. These demands like a high temperature T, particle density n, and confinement time τ_E are specified in the Lawson criterion:

$$n \cdot \tau_E \cdot T \geq 6 \cdot 10^{28}\ \mathrm{sKm^{-3}} \tag{1.3}$$

Since the plasma primarily consists of charged particles, it is possible to control the movement and expansion of the plasma via electric and magnetic fields. Therefore, the plasma is confined magnetically via a toroidal configuration with drilled field lines. Two examples of toroidal machines are the tokamak and the stellarator. The stellerator uses a single coil system to create the magnetic cage and, thereby, a stellerator can be operated continuously in contrast to a tokamak that works in a pulsed mode due to the transformer coil, which is needed to induce the plasma current. The next section will solely describe the structure, mechanics, and benefits/drawbacks of the tokamak concept in dependence on the context of the dissertation.

1.2 Tokamak

Since the 1960s, when the tokamak concept was invented in the Soviet Union, scientists from all over the world worked on the understanding of the plasma physics behind fusion and the technical advancement of the tokamak design. In a tokamak, the plasma is confined in a torus-shaped vacuum vessel that is surrounded by two sets of magnetic coils. These coils create a toroidal and poloidal field, which act as magnetic cage and ensure that the plasma is kept away from the walls. Both fields are needed due to the change of the magnetic field ∇B and curvature drifts that lead to charge separation, which produces a downward electric field, which in turn leads to an outward drift of the particles and a float of the plasma away from the axis of rotation to the vessel walls [7]. For this reason, the field lines need to be twisted so that the particles primarily spiral along them and do not rapidly escape the magnetic cage. Regarding this, a plasma current is induced by the inner central solenoid magnetic field coil to stabilise the plasma. At this, the magnetic coil in the centre of the machine acts as primary winding of the transformer while the plasma acts as secondary winding. The induced plasma current is the reason for the pulsed operation mode of a tokamak. The schematic illustration 1.3 gives an overview of the structure.

The continuous development of heating and confining the plasma sufficiently led to the first experiments with a controlled release of fusion energy (Joint European Torus (JET)), which proved the technical feasibility of the deuterium tritium fusion. Then scientists researched on the power plant scale and finally, a group of

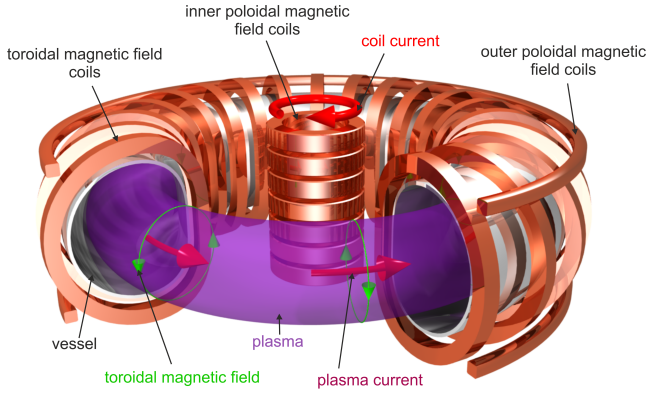


Figure 1.3: Schematic illustration of the tokamak design [8]. The vacuum vessel is surrounded by two types of coils which ensure that the plasma is confined and kept away from the vessel walls.

industrial nations (European Union (Euratom), Japan, USA ect.) made an effort to develop fusion as a sustainable source of energy [1]. This led to the agreement to jointly pursue the design and building of the experimental fusion facility ITER (latin: "way"; originally an acronym for International Thermonuclear Experimental Reactor). ITER is a tokamak with a vacuum vessel with a diameter of 6 meters that is twice as large as any previous tokamak. The vacuum vessel is surrounded by the cryostat that guarantees the cooling of the superconducting toroidal and poloidal field coils, diagnostics, and external systems [1]. Figure 1.4 shows a model of the machine.

One scientific goal of this large scale experiment is to investigate and demonstrate a burning plasma that is characterised by alpha-particle heating and long pulse operation (300-500 s). The alpha-particle heating enables the plasma to regulate its own profile [9]. Furthermore, ITER shall deliver ten times the power it consumes for heating (input power 50 MW) [1]. The ratio of energy that is achieved in a nuclear fusion device to energy that is required to maintain the plasma is expressed by the fusion energy gain factor (Q-factor). This fusion energy gain factor is thus defined as [10]:

$$Q \equiv \frac{P_{\text{fusion}}}{P_{\text{heat}}} \tag{1.4}$$

Other objectives of ITER are the prove of key technologies, the investigation of the components, and the control of plasma wall interactions. Not at least, the know-

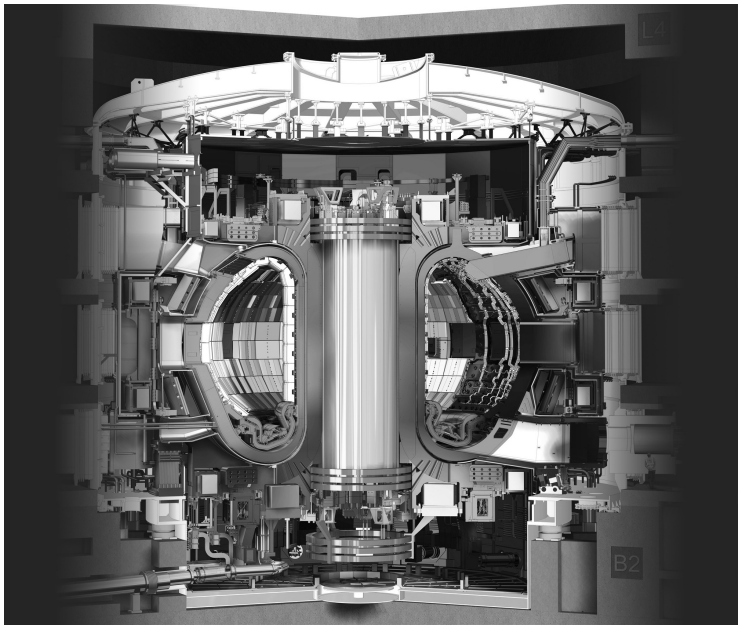


Figure 1.4: A model of the experimental fusion reactor ITER [1]. The ITER tokamak will not only be the world's largest tokamak with a plasma radius of 6.2 meters and a plasma volume of 840 m^3 but also its constituent parts will be first-of-a-kind. The entire reactor will count thirty meters in diameter and nearly as many in height [1].

how gained with ITER is to fetch all necessary information to construct the next-generation machine, a demonstration power plant (DEMO), that will bring fusion research to the threshold of a prototype fusion reactor [1]. Therefore, ITER will be equipped with numerous diagnostic systems to study plasma physics and to control and optimise the plasma performance, but it will not have an electricity conversion system. The plasma performance is, among others, linked to the confinement mode. In ITER, the high confinement mode (H-mode) is assumed as the reference scenario for operation [11]. Moreover, the edge transport barrier in such an H-mode plasma has steep edge gradients, which are affected by quasi-periodic barrier relaxations, so called edge localised modes (ELMs) [12, 13]. In addition to ELMs, there are vertical displacement events (VDEs) and plasma disruptions, which can occur if the plasma current gets disturbed. The uncontrolled termination of plasma instabilities implies the necessity of the conscientious selection of plasma facing materials (PFMs), researches of the performance of the PFMs and plasma facing components (PFCs), and as a consequence thereof the control of plasma wall interactions.

The most affected part of the in-vessel components will be the divertor and, there-

fore, of special relevance in terms of performance, durability, and cost efficiency. The divertor, which is situated along the bottom of the vacuum vessel is made up of 54 remotely removable cassettes that will act as a huge power and particle exhaust system [1]. This exhaust system has the task to remove the helium atoms and heat, both products of the fusion reaction, and other impurities from the plasma to avoid a break down of the fusion reaction rate. Each of the removable divertor cassettes are equipped with three PFCs that transform the kinetic energy of the plasma particles and neutralise them. The neutralised particles will be removed by vacuum pumps. Figure 1.5 shows a schematic view of an ITER divertor cassette.

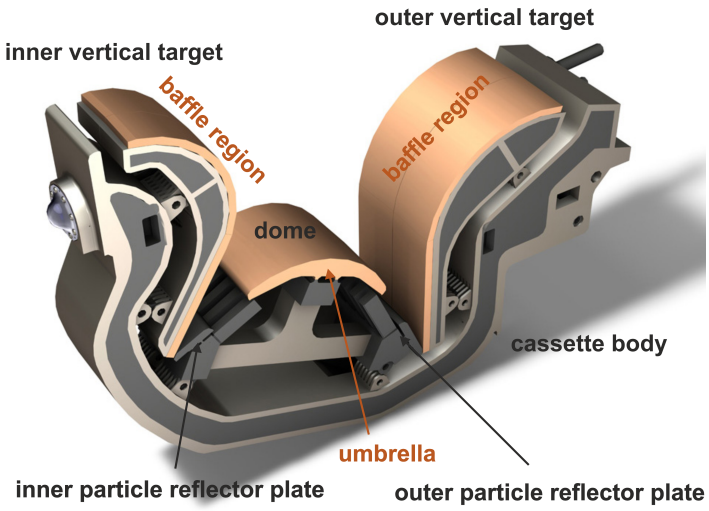


Figure 1.5: Schematic of one of 54 ITER divertor cassette [14] that is equipped with three PFCs. The choice of the amour material for the PFCs is difficult, because only very few materials are able to withstand the extraordinary loads [1].

The ITER divertor will be the most advanced and most complex of its kind. Due to the naturally imperfect plasma confinement, it is possible that the electrically charged particles move across the separatrix, which is the boundary between closed and open field lines to the region where the field lines meet the PFMs of the divertor. The region characterised by open field lines is called scrape-off layer (SOL). It becomes apparent that the combination of high thermal and particle fluxes, which deposit huge heat loads on the PFCs, influence the material properties and thus the lifetime of the PFCs. Consequentially, the previously mentioned aspects lead to high requirements on the PFMs that translate the selection of suitable materials

into an extremely tough decision.

1.3 Plasma wall interaction

As previously mentioned, the magnetic confinement is not perfect. During a plasma discharge there are fluxes of particles like electrons, hydrogen alpha particles etc. from the edge plasma that transfer their energy to small areas on the PFCs. In detail, the steady state heat flux for the first wall is assumed to be up to 1 MW/m^2 and for the divertor region up to 10 MW/m^2 (20 MW/m^2 during slow transients with a duration < 10 s) [15, 16]. This energy will be transfered to the near-surface lattice atoms of the PFMs, which in turn excite to collisions with other lattice atoms that lead to physical sputtering if the transfered energy exceeds the binding energy. Additionally, sputtering by fast neutrals and chemical sputtering result in erosion processes of the plasma facing materials. The eroded atoms could enter the plasma and increase the concentration of impurities in the plasma. In the worst case scenario, the tolerable amount of impurities will be exceeded, which will cause a loss of confinement, lead to energy deposition on the surface of the vacuum vessel, and, therefore, limit the lifetime of the PFCs [7, 17]. Moreover, if the eroded atoms get ionized this will degrade the energy or rather temperature of the plasma, which could result in a break down of the fusion reaction.

Furthermore, erosion can also be caused by blistering, which means that energetic particles, which intrude the material, produce vacancies and odd particles. When these odd particles agglomerate and interact with e.g. vacancies, bubbles will be formed in the near-surface area, which are called blister [18, 19]. Moreover, this process implicates not only local swelling but also a degradation of the mechanical properties. Complemental, the different PFMs have varying erosion yields. In particular, the materials with a low atomic number Z show higher yields than the high-Z materials like tungsten. Moreover, the impurity ions interact with the plasma electrons, which results in the production of electromagnetic radiation that changes the plasma temperature and plasma pressure gradients. This will negatively affect the plasma stability and confinement. In addition, the eroded particles will be redeposited on the PFCs and form layers and/or disintegrate into dust. The negative consequences arising thereby are the retention of tritium in these layers and the accumulation of dust. It is essential to limit both, the in-vessel tritium retention and the dust production, to minimize the impact of possible accidents and consequently the extent of polluting releases [15, 16, 20].

On top of the previously mentioned heat loads, the materials have to withstand high ion, electron, and neutral fluxes. For example, in the divertor region there will be fluxes of $> 10^{24}$ m^{-2}s^{-1} that lead to total fluences of $> 10^{26}$ m^{-2}, plasma densities of around 10^{21} m^{-3} and plasma temperatures of up to 3 eV for each pulse in ITER.

This will heat the surface of the PFCs at the divertor to up to 1500 °C and the first wall to up to 300 °C. However, for the first wall the ion flux is three orders of magnitude smaller and the neutral flux is in the range of $10^{19} - 10^{21}$ $m^{-2}s^{-1}$ [21]. Furthermore, the hydrogen isotopes will interact with the PFMs by diffusion along the grain boundaries into the bulk material. The implanted hydrogen atoms will then either diffuse back to the surface or deeper into the bulk material. Anyhow, this interaction will alter the mechanical properties of the PFMs e.g. in terms of embrittlement and hence could promote the formation of cracks [22, 23]. Certainly, not only the hydrogen isotopes have an influence on the PFMs, but helium as well. Studies have shown that the formation of helium bubbles decreases the thermal conductivity and could also affect the PFMs resilience to transient events like ELMs [24]. Moreover, the accumulation of helium in the near-surface region accounts for the development of nanovoids, which in turn lead to the formation of nano structures (fuzz) [25, 26]. These aspects have to be taken into account for the long-term material evolution during the plasma operation in a fusion device because they can detrimentally influence the material performance.

Additionally, neutron irradiation is a serious concern due to the changes of the structure of the material. The neutron radiation induces defects/displacements in the lattice (vacancies, interstitials) and leads to changes of the microstructure. Another important fact is transmutation that involves a change of the chemical composition. If the chemical composition changes, also the mechanical and physical properties will alter and thereby, the performance of the plasma facing materials could deteriorate significantly [27]. Beside the steady state conditions, there are transient events, which are the result of plasma instabilities that in turn occur due to fluctuations and eletromagnetic forces in the plasma confinement. These transient events deposit energy densities of several tens of MJ/m^2 with a pulse duration of a fraction of ms to tens of ms on a localised surface area. The absorbed energy density L_{abs} during a transient event in ITER in combination with the pulse duration Δt of such a transient heat pulse can be expressed by the heat flux factor (F_{HF}), which is quantified by the formular $F_{HF} = L_{abs} \cdot \Delta t^{0.5}$. Moreover, the temperature increase ΔT during a thermal shock can be expressed by $\Delta T = 2 \cdot L_{abs} \cdot (\frac{\Delta t}{\pi \lambda \rho c_p})^{0.5}$ where λ is the thermal conductivity, ρ the density, and c_p the specific heat capacity of the material. F_{HF} is used in the fusion community as quantity to compare the influence of the different kinds of transient heat loads on the material performance and to define threshold values. Figure 1.6 shows the different stationary and transient power loads expected in ITER.

Edge localised modes (ELMs) are a common feature of H-mode operation and count among normal events. ELMs are periodic disturbances of the plasma edge region, accompanied by a rapid expulsion of edge plasma and the degradation of the confinement. They occure when the plasma pressure gradient inside the separatrix

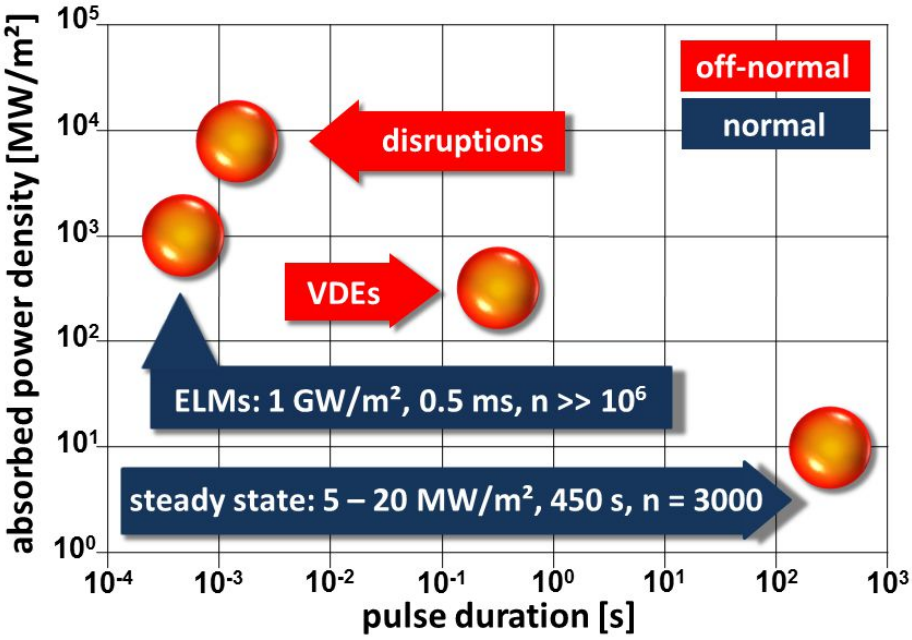


Figure 1.6: The diagram shows the expected steady state loads as well as the transient events for the divertor in ITER. Edge localised modes (ELMs) occur during normal ITER operation and deposit huge amounts of energy and particles on the PFMs. Addionally, there are so called off-normal events, namely vertical displacement events (VDEs) and plasma disruptions [16, 28, 29].

builds up and exceeds a critical threshold. In that case, energy and particles will be released into the SOL on a very short timescale (< 1 ms) and finally, by following the magnetic field lines, this heat and particle fluxes will be deposited on the divertor targets [30]. Several ELMs are expected during each ELMy H-mode discharge. Each ELM event will cause a very fast increase of the PFCs surface temperature and lead to surface modifications, high levels of erosion, associated with an increased impurity concentration of the core plasma [15,30]. Edge localised modes can be differentiated into three groups, Type I (giant) ELMs, Type II (grassy) ELMs, and Type III (small) ELMs, in dependence of their repetition frequency on the heating power, the occurrence of magnetic precursors, and the stability of the plasma (magnetohydrodynamics (MHD) stability). Typ I ELMs are expected to drive the main process of wall erosion in ITER. The energy losses from the core plasma during Typ I ELMs in H-mode are in the range of 2 - 10 %, which was measured on tokamaks like JET, ASDEX-Upgrade, and DIII-D. This result indicates that ELMs in ITER will have a frequency of $\sim$ 1 - 5 Hz and energies between 25 and 80 MJ [13, 30]. Events with such high energy densities will entail irreversible damage and have to

be mitigated.

Besides the prior mentioned normal events, the PFCs will be affected by so called off-normal events like VDEs and plasma disruptions. A plasma disruption is caused by a strong stochastic magnetic field that leads to a sudden breakdown of the plasma. A disruption (0.1 - 5 ms) starts with the precursor phase in which the distortion of the plasma and magnetic field is induced [31]. This distortion leads to an immediate energy loss (called thermal quench) followed by the decay of the plasma current that is called current quench. Moreover, the current inside a tokamak plasma decays fairly quickly and generates a voltage in the plasma, called loop voltage. That loop voltage in turn can cause electrons that are already in the plasma to speed up to very high kinetic energies. These electrons are known as runaway electrons (RE) [32,33]. Another kind of off-normal event, namely vertical displacement events, is the result of the loss of vertical control of the plasma position. As a consequence, the plasma drifts vertically and affects the vessel wall by depositing up to 60 MJ/m^2 within 100 ms - 300 ms [34,35].

This all amounts to the fact that normal and off-normal events as well as runaway electrons caused by abnormal plasma behavior have the potential to seriously damage the plasma facing components and limit their life time, accompanied by the degradation of the reactor performance and safety. Therefore, a number of technologies have been developed to mitigate these events. Nevertheless, even mitigated transient events with intense energy deposition over very short periods may result in surface modifications like roughening, erosion losses of surface material, crack formation, and/or a high temperature rise that could lead to recrystallisation or even melting [36]. For that reason, it is vital to develop approaches to reduce these loads to tolerable values and/or to avoid the effects of plasma disruptions. Two approaches are under consideration, massive gas injection (MGI) and shattered pellet injection (SPI). The MGI introduces huge amounts of noble gases such as neon, argon, deuterium etc. or mixtures of these into the vacuum chamber within several ms. This MGI application into the disruptive plasma converts the thermal energy into radiation that is homogeneously distributed inside the vacuum chamber [37,38]. Shattered pellet injection uses cryogenic pellets, mostly consisting of neon and deuterium. The cryogenic pellets will shatter against a plate in order to disperse the material better into the plasma. Furthermore, the injected material will inhibit the formation of RE that could lead to fast and localised heat loads of several MJ on the PFC [1,38].

In conclusion, the previously mentioned plasma wall interactions are a serious problem for the PFCs/PFMs and associated with an efficient, economical and safe operation of a fusion device like ITER.

1.4 Plasma facing materials

One of the numerous challenges of the ambitious project to design and build a practical fusion device is the selection of the right materials for the internal components that will directly face the fusion plasma. These PFMs will be joined onto an actively cooled substrate (precipitation hardened copper based alloy CuCrZr will be used in ITER), the heat sink, which transfers the surface heat to the cooling channels. In ITER the plasma facing surface will cover an area of about 830 m^2 [39]. The materials used for this area (PFMs) should ensure a sufficient plasma compatibility, an adequate heat exhaust capability, and corrosion resistance as well as radioprotection requirements. Table 1.1 lists the most important requirements.

Table 1.1: Requirements for the materials to be used as plasma facing materials in fusion devices [28, 40–42].

properties	**requirements**
thermal / mechanical	high thermal conductivity
	high thermal shock resistance
	high melting/sublimation temperature
	high cycle thermal fatigue resistance
plasma compatibility	low atomic number (Z)
	low tritium inventory
	low erosion rate/high sputter resistance
	low vapor pressure
neutron irradiation	low neutron activation
	neutron induced degradation resistance
	no critical elements in the transmutation chain
others	acceptable costs
	availability of the material
	workability
	availability of joining techniques
	injurious to health & nonpolluting

Additionally, as mentioned in the previous section, the materials have to withstand vast thermal and particle fluxes from the core plasma over the time of operation without maintenance in the best case. Consequentially, the PFMs have to fulfil a wide range of requirements containing thermal, mechanical, atomistic, etc. parame-

ters that restrict the contemplable materials [28,40]. Besides the required properties, the PFMs must have to withstand high cyclic heat, neutron, and ion fluxes. Hence, the selection will furthermore depend on the position, the function, and the need in the machine. In other words, various materials will be used as amour for the in-vessel components like first wall and divertor due to the different exposure conditions of these in-vessel regions. Moreover, the PFMs may have a specially tailored design (to ensure protected leading edges [43]), microstructure as well as chemical composition to avoid the loss of the thermo-mechanical integrity that could cause devastating consequences. Thereby, the fabrication method of the materials, the impurities and alloying elements, the pre- and postthermomechanical treatments, and the final shape and geometry sustainably influence the obtained microstructure [44].

Further on, the plasma will be contaminated with atoms from the PFMs that lead to a deteriorated plasma performance. The permitted amount of impurities decreases with the atomic number (Z) of the impurities, in detail, a high Z-number is connected to a large energy loss when these atoms became ionised and, therfore, are associated with a far lower tolerable impurity concentration. In addition, the excitation and deexcitation as well as bremsstrahlung cause the previously mentioned radiation losses and involve the risk of a complete plasma breaking down. At this point, the low Z-materials are more beneficial, but their big disadvantage is the higher erosion rate [41].

As a remark, fusion processes involve radioactive materials like tritium, a radioactive isotope of hydrogen with a half-life of 12.3 years, that will be absorbed by the in-vessel materials and give rise to their radioactivity. Additionally, the fast neutrons produced by the fusion reaction will interact with the PFMs and activate them. Also, a contamination with radioactive dust of the in-vessel materials has to be taken into account in the context of safety limits. Most of the generated radioisotopes have a half-life lower than ten years, which is a beneficial aspect compared with the long living products in nuclear fission. The low half-lifes of the generated radioisotopes imply the opportunity of a local storage of the generated waste materials in hot cells. Within 100 years, the radioactivity must have decreased in a considerable way that the materials can be recycled. The safety limit of ITER for mobilisable dust is ≤ 1000 kg and for dust on hot surfaces $\leq 11/76$ kg (Be/W). The limit of tritium in dust and co-deposited in layers on the in-vessel components is ≤ 1 kg [1,21].

All the requirements like performance in terms of erosion lifetime, thermal shock and thermal fatigue resistance, vacuum compatibility as well as design, safety, and administrative limits reduce the list of possible materials remarkably. In the current design of ITER, beryllium (Be) will be used for the FW panels as PFM and a full-W divertor will be installed from the first day of operation [16]. The next

step after ITER, the demonstration power plant (DEMO), is proposed to have two operation phases, phase one in which the breeding blanket and divertor concepts will be refined and phase two, where the final concepts will be proven. Moreover, in DEMO the PFMs for the first wall could be made of stainless steels (e.g. reduced activation ferritic-martensitic (RAFM) steels, oxide dispersion strengthened (ODS) RAFM steels) with water or more likely with a helium cooled design and with or without a protection layer of tungsten or tungsten alloys. The most promising materials in general are tungsten, tungsten alloys, a SiC matrix with embedded SiC fibres and the steels mentioned [45, 46].

Table 1.2: Main advantages and disadvantages of Be, W and RAFM/ODS steel for fusion applications [41, 42, 45, 47–51].

material	advantages	disadvantages
beryllium	high thermal conductivity	low melting point
	oxygen getter	low neutron radiation resistance
	plasma compatibility (low Z)	short erosion lifetime
	low activation	toxicity
	no chemical sputtering	
tungsten	high melting point	high Z
	high thermal conductivity	recrystallisation
	low tritium retention	high DBTT
	low swelling	neutron/hydrogen embrittlement
	low erosion rate	high radioactivity
RAFM steels	high thermal conductivity	irradiation hardening
	good resistance to swelling	embrittlement T $<$ 675 K
	corrosion resistance	low creep strength T $\geq$ 875 K
	favourable cost	softening during cyclic loading
ODS steels	high creep strength	low fracture toughness
	operation T up to 700 °C	non-isotropic grain shape
	good oxidation resistance	difficult fabrication

Table 1.2 outlines the most important advantages and disadvantages of the plasma facing material candidates for future fusion devices. Additionally, the listed advantages and disadvantages of stainless steels are general-purposed and may be less marked or vary in dependence on the chemical composition and microstructure. The selection of the materials for different applications listed in table 1.2 is based

on current experience and enables ITER to proof and test the PFMs for DEMO and the ensuing prototype fusion reactor in a broad range of burning plasma scenarios. However, for DEMO many different industrial grades of these materials will be developed to meet a variety of requirements.

Considering the high heat fluxes at some areas of the FW, the necessity of two types of FW panels, enhanced heat flux (EHF) panels, which are capable of removing an incident heat flux of up to 4.7 MW/m² and normal heat flux (NHF) panels, which have been tested for a heat flux up to 2 MW/m², is clearly indicated [39]. The benefits of using beryllium for the first wall are the high thermal conductivity and an appropriate plasma compatibility due to the low Z that permits a relatively high concentration in the plasma ($\sim$ 15 %). Furthermore, it will act as an oxygen getter to clean the plasma and does not suffer chemical sputtering. The drawbacks of Be are the relatively low melting point ($\sim$ 1280 °C) that will lead to enhanced melting, the short erosion lifetime due to physical sputtering, the toxicity, and the poor resistivity against neutron radiation induced damages, like e.g. swelling [27, 48, 52].

As mentioned in section 1.2, the divertor will be affected by the highest surface heat loads. On this account, tungsten, with the highest melting point of all elements and at the same time one of the best thermal conductivities, has been chosen. Additionally, the low erosion rate is also beneficial, whereas the high ductile-to-brittle transition temperature (DBTT), the high Z, and the remarkable activation induced by neutron irradiation are the disadvantages of tungsten [16, 42, 47].

In terms of structural and armour materials for DEMO, RAFM steels, ODS steels, and tungsten could be appropriate candidates [45, 53, 54]. The decision, which material will be used for which in-vessel application, will be even more challenging than in ITER due to the long pulse or steady-state operation. So far, tungsten seems to be again the favored material for the divertor, caused by its aforementioned advantages, where the heat loads can be $\geq$ 20 MW/m² and the particle fluxes $> 5 \times 10^{22}$ m^{-2}s^{-1} [45, 55, 56]. At this point, the most promising structural materials for DEMO are ferritic martensitic steel. The benefits of ferritic-martensitic steels are a relatively high thermal conductivity and mechanical properties, the low sensitivity to radiation-induced swelling, the high compatibility with major cooling/breeding materials, and the broad industrial experience.

EUROFER, which is one leading candidate for structural applications, shows besides its advantages some issues. The most serious issue is the limited temperature operation window and tightly connected with it, the low-temperature embrittlement and the loss of the creep strength [45, 46]. Furthermore, the radiation hardening also counts as main drawback and lets EUROFER appear as a structural material in the case of low or moderate wall temperatures. On the contrary, ODS steels may po-

tentially and considerably increase the limited temperature window of RAFM steels and improve the strength and creep resistance at high temperatures [46]. Here, the major drawback is the manufacturing by powder metallurgy via mechanical alloying, and HIPping (Hot Isostatic Pressing) that is not only time consuming but expensive. Furthermore, this processing leads to the formation of coarse oxide particle with non-uniform size, a non-isotropic grain shape, and a residual porosity [51].

1.5 Scope of work

The ambitious experimental project ITER will test technologies, physics, and materials, which are needed for initiating the aspired commercial generation of fusion-based electricity. The path to fusion power plants involves plenty of challenges and one of the main challenges is the selection of appropriate materials or the development of high performance materials that satisfy the requirements. These requirements imply that the materials for in-vessel applications, the so-called plasma facing materials for the first wall and the divertor, have to resist and/or to survive the combination of high paticle fluxes, steady state heat loads, and transient events to guarantee a reasonable lifetime (see subsection 1.3).

The list of contemplable materials is short, since the in-vessel conditions are so provoking and the economical criteria, like availability, cost, machining, and the safety-related requirements play an decisive role and can not be neglected. Consequential, the materials, which seem to fulfill most of the criteria (see section 1.4), are beryllium and tungsten as well as possibly ferritic martensitic steel (DEMO). In ITER, beryllium is the material for the first wall and tungsten will shield the divertor. For the next step, DEMO, tungsten will most likely be used again to face the plasma in the divertor region and could also be an appropriate candidate for the first wall. The decisive benefits of tungsten are the high thermal conductivity, the high melting temperature, the low tritium retention, and erosion rate, whereas the high atomic number, the relatively poor mechanical properties at low temperatures (high DBTT), and the neutron irradiation induced activation are considered as some of its disadvantages (see subsection 1.4). Ferritic martensitic steel that is used in ITER for remote areas, will be inserted as structural material in DEMO but could also be promoted as PFM for the FW. Its advantages in dependence on the application are the good resistance to swelling, corrosion, and oxidation etc. but there are disadvantages like irradiation hardening as well as low fracture toughness (see subsection 1.4).

The decision for tungsten as plasma facing material contains the indispensable examination of the performance under the expected conditions in future fusion devices as well as the implementation of the gained results and experience in subsequent experiments and development processes. This applies also to ferritic martensitic steel that will be exposed to repeated intense photon pulses evoked by protection

procedures (MGI) [57, 58] and if it will be promoted as PFM the conditions for the material will become even worst. Consequently, not only the impact of single loading parameters (steady state heat loads, ELMs, etc.) but synergistic effects of thermal and particle loads have to be examined. Accessory, the influence of material-specific properties like e.g. the microstructure on the damage behaviour has to be included in the evaluation and interpretation of experiments and results. For that reason, sequent tests on industrially produced pure tungsten in the as received and recrystallised state, which were elaborated in this work, approached gradually to more realistic conditions in order to understand the underlying mechanisms of the thermal shock and damage behaviour as well as synergistic effects. In this connection, the experiments on tungsten can be divided in two sections (chapter 4).

In the first experiments, the influence of thermal (Nd:YAG laser) and particle (plasma) exposure on the material performance is investigated by varying the power densities, the compositions of the plasma, on the one hand pure deuterium plasma (section 4.2) and on the other hand mixed deuterium helium plasma (section 4.3), and the loading order as well as the base temperature and pulse number. Afterwards, the results are evaluated and compared with reference to significant differences in the thermal shock and damage behaviour (section 4.4). The determined distinctions of the material performance are related to the microstructure (e.g. grain orientation to the loaded surface) and, therefore, to particular material parameters/properties, interactions between particles and the tungsten lattice, and to the influence of the loading order and base temperature.

Furthermore, to investigate the impact of transient thermal loads on the performance of tungsten high pulse number experiments with plasma background are executed (section 4.5). With regard to the expected amount of ELMs ($\gg 10^6$) onto the divertor during its service time in ITER an analysis of the effects of high numbers of stress cycles is irremissible to detect e.g. fatigue effects and to forecast the peformance and lifetime of plasma facing materials. Therefore, a continuous deuterium helium (6%) plasma background is used corresponding to the operation conditions in ITER, while the number of applied laser pulses is raised to 10,000 and 100,000, respectively. These tests shall give information about material modifications, degradations, and damages, how the plasma exposure affects the thermal shock behaviour in comparison with high thermal loads solely, and about lifetime estimations. Thereby, the tungsten tests are enclosed and the next chapter addresses oneself to the examination of steel.

In particular, the fifth chapter of this work researches the formation of melt layers and their consequences for the material performance. Here, ferritic martensitic steel P92 that is intended as structural material but could also become a possible plasma facing material for the first wall in DEMO is tested in JUDITH 1 and PSI-2 suc-

cessively. The electron beam facility is used to generate melt-layers by using two different power densities and afterwards thermal and particle loads are applied on the solidified surfaces, again by varying the power density and loading sequence. The surface modifications and microstructural changes will be investigated dependent on the pre-exposure, loading sequence, and power density to predict statements about the material peformance or degradation during DEMO operation.

Finally in chapter 6, the most important facts of expected material modifications and damages of both chapters are outlined, how the loading conditions and parameters affect the material performance, and whether these damages are acceptable or have to be prevented. Moreover, the influence of the gained results and experiences on the operation of ITER, the development of new materials, and/or the improvement of existing PFMs will be discussed in detail.

2 Materials

In the frame of this work, two different materials that are auspicious candidates for applications in future fusion devices were investigated. As pointed out in the previous chapter, the tremendous loads impose high requirements on the materials and one of the most important requirement, considering the application and/or component lifetime, is definitely the thermal shock resistance. On that account, this chapter outlines essential facts, like manufacturing, microstructure, thermal and mechanical properties etc., about the examined tungsten and stainless steel grades.

2.1 Tungsten

Tungsten is a metallic transition element with the atomic number Z = 74 and a body centered cubic (bcc) crystal structure. There are also other crystal structures but those are less energetically stable. The density of tungsten is nearly equal to the density of gold and thus one of the highest. The advantages of tungsten are the high thermal conductivity, the high melting temperature (3422 °C), the low tritium inventory, and the low sputter yield due to hydrogen or helium bombardment, which let tungsten appear as an attractive material for fusion applications. Nevertheless, the main drawbacks are the restricted operation window and the poor workablility. Both result from the brittle behaviour at low temperatures and recrystallisation processes that arise at temperatures above 1200 °C. Thereby, the high ductile to brittle transition temperature (DBTT) is not a precise and reproducible value, it varies between 100 - 600 °C depending on the mechanical and structural properties of the material as well as on the loading conditions, e.g. strain rate. In addition, the higher the degree of plastic deformation of the material, the lower is the DBTT [59].

The tungsten grade used in this work was commercially available, double forged pure tungsten in the stress relieved and recrystallised state. It was manufactured and delivered by the Austrian company Plansee SE. This tungsten grade had a guaranteed purity of 99.97 wt% (metallic purity excluding molybdenum < 100 μg/g) and was produced by powder metallurgy. The general production process is schematically illustrated in figure 2.1.

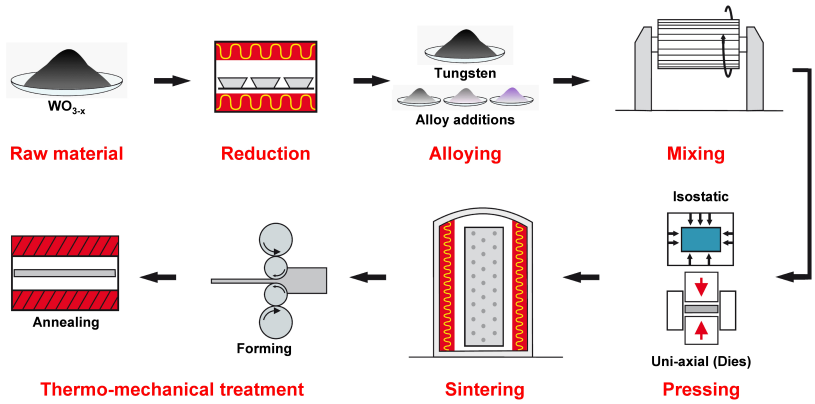


Figure 2.1: Overview of the main steps of the powder metallurgical production process of commercially available tungsten grades and alloys [60].

The production starts with the raw material, which is enriched tungsten oxide ($30 - 70\%$ WO_3) that is seperated from the ores by crushing, grinding, floating, and roasting and by using chemical reduction. This process results in particularly homogeneous powders. Moreover, it is possible to add doping or alloying elements either in the raw material or after the reduction process to improve the material performance. Afterwards, the tungsten powder is sieved, homogenised, and densified by cold isostatic pressing. Subsequently, the pressed blanks are sintered at temperatures between 2000 °C and 2500 °C [59, 60]. To increase the density of the sintered blanks and additionally, to improve their mechanical properties, the blanks are mechanically deformed by rolling, forging, or swaging at temperatures up to 1600 °C. A final heat treatment, namely annealing, removes the induced, residual stresses. In this connection, the annealing temperature depends on the degree of deformation [59].

The tungsten grade that was investigated was forged in the radial direction and along the cylinder axis. The forged blank had a disc shaped geometry [61] and was stress relieved at 1000 °C. Furthermore, the forging caused an anisotropic microstructure with elongated grains. This elongation had to be taken into account when cutting the samples, because in dependence on the cutting scheme the grains have a preferential orientation. Moreover, the location where the samples were cut out can play a role due to a possible inhomogeneity of the microstructure at the centre or the edge of the blank evoked by the forging process. To preclude a potential influence of the cutting location, the experiments were executed with samples, which were all taken from the same area. Besides the as-received material, the same material in the recrystallised state (at 1600 °C for 1 h) was investigated. The recrystallisation process yields an almost uniform microstructure without a preferential orientation

of the grains but it also causes an agglomeration of defects at the grain boundaries, which in turn lead to a smaller yield strength and a reduced cohesion between the grains. A detailed analysis of the microstructure, which is indispensable to qualify the manufacturing process and to understand the performance of the material under thermal/particle loads, was done during former studies as well as the characterisation of the thermal and mechanical properties [62] .

As mentioned above, the elongation of the grains had to be taken into account when cutting the samples. Therefore, samples with different grain orientations relative to the sample surface were EDM (electrical discharge machining)-cut from the as recieved tungsten round blank with the dimensions $12 \times 10(12) \times 5$ mm³. In detail, samples with a longitudinal (L) grain orientation that means parallel with regard to the surface of the specimen that will be loaded and with a transversal (T) grain orientation, where the elongated grains are oriented perpendicular to the surface, were produced. Moreover, samples with the same dimensions were cut from the recrystallised (R) material. Figure 2.2 shows the cutting scheme and the resulting grain orientation that were used for all experiments in this work.

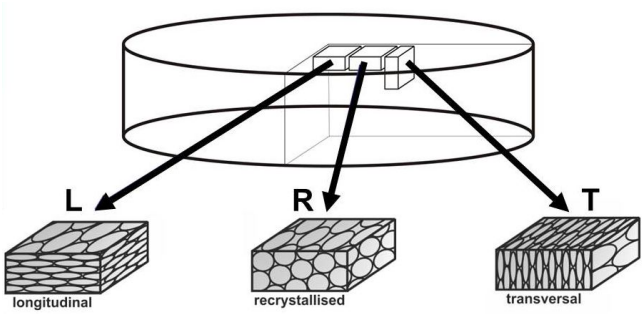


Figure 2.2: The sketch shows the cutting scheme and the resulting grain orientation of the samples [63]. Two different sample types (longitudinal and transversal) were cut from the as-received tungsten to investigate the influence of the microstructure on the performance and thermal shock behaviour. Additionally, samples of the same material but in the recrystallised state (1600 °C for 1 h) were analysed.

After cutting, the samples were polished to a mirror finish by using SiC paper and diamond paste, starting with a granulation of 80 and ending with 1 µm diamond paste. The polishing procedure was necessary to remove all surface damages and thermally induced defects/modifications from the cutting as well as to obtain a complete damage-free reference surface with an arithmetic mean roughness of < 0.05 µm. This well-defined reference surface ensures the verification of exposure induced surface modifications and damages.

2.2 9-12%Cr ferritic martensitic steels

9-12%Cr ferritic martensitic (FM) steels are widely used in power plants due to their good thermophysical and mechanical properties, low thermal expansion coefficient and low susceptibility to thermal fatigue as well as high compatibility with major cooling and breeding materials. The broad industrial experience, particle knowledge, and material properties make FM-steels attractive for applications in fusion devices like DEMO. In recent years, characterisation programms and material developments were performed and reduced activation ferritic martensitic (RAFM) and oxide dispersion-strengthened (ODS) steels were developed and produced [50,64,65].

Furthermore, conventional FM-steels had to be modified to meet the requirements for applications in fusion devices and to utilize them as structural materials or plasma facing materials in DEMO and devices beyond [53, 54]. To achieve a low activation capability molybdenum (Mo), niobium (Nb), and nickel (Ni) were replaced by tungsten (W) and tantalum (Ta) that improved high temperature creep strength. In addition, Ta stabilises the grain size due to carbide formation and a low W content (under 1 wt%) is beneficial for a higher tritium breeding ratio. The long-term creep rupture strength and microstructure stability was improved by alloying cobalt and tungsten respectively, which are primarily solid solution strengtheners. Here, 2-3 wt% cobalt should improve the short-term creep strength as well [65]. Furthermore, the RAFM and ODS steels were strengthend both by solution hardening (addition of chromium (Cr) and W) and precipitation hardening (complex carbides such as $M_{23}C_6$). The Cr content was raised to get better corrosion resistance and to minimise the shift of the DBTT after irradiation but it has to be controlled due to the embrittlement induced by aging or irradiation. Moreover, Cr contributes to the oxidation resistance, too. Normalising and tempering heat treatment processes are generally used to obtain good strength and toughness [50,65]. A characteristical tempered martensite is composed of martensite laths in connection with a high dislocation density and precipitates. The precipitates are settled along the grain boundaries and laths boundaries. The normalising treatment results in a martensite matrix with precipitates, which in turn can impede the movement of dislocations [65].

Table 2.1: Chemical composition of the investigated FM steel P92 [66].

element	C	Si	Mn	P	S	Cr	Mo	Ni	Cu
amount[wt%]	0.120	0.36	0.48	0.019	0.002	8.98	0.50	0.33	0.04
element	Nb	V	Ti	Al	N2	W	B	Zr	
amount[wt%]	0.07	0.20	0.003	0.014	0.053	1.69	0.0027	0.002	

Table 2.1 presents the detailed chemical composition of the ferritic martensitic steel that was investigated within this thesis. This steel was commercially produced P92 (X10CrWMoVNb9-2) manufactured by BGH Edelstahl Freital GmbH, Germany [66]. P92 was chosen as a favorable alternative to the European tempered ferritic martensitic steel called EUROFER that is intended to be used as structural material in DEMO [51].

The properties of different steel types vary in dependence on the chemical composition as well as the manufacturing process. That means, not only the element content but the production stages are individually adapted depending on the needed material properties for the respective field of application. Figure 2.3 depicts exemplarily the production stages of the BGH Edelstahl Freital GmbH.

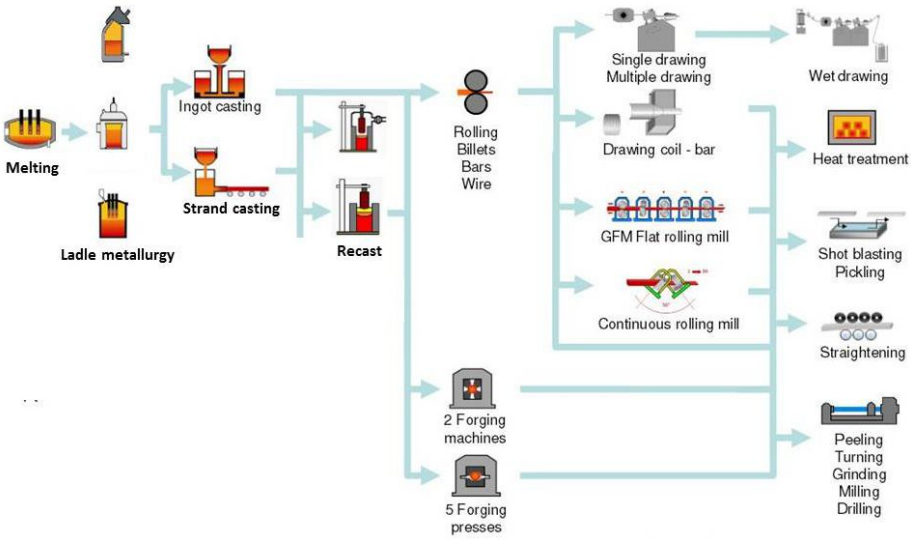


Figure 2.3: The sketch illustrates the main production stages and different possible production stages respectively. Depending on the intended properties of the material and area of application, the manufacturing processes are adapted [66].

As mentioned before, heat treatment processes are basically used to strengthen the material. In case of the used P92, the steel was hardened at 1060 °C and tempered at 765 °C [66]. This heat treatment led to the characteristic microstructure that is presented in figure 2.4. This light microscope image of a metallographic cross section displays clearly the ferritic martensitic structure, where the dark areas are the hard martensite phase and the light ones are the soft and ductile ferrite phase. After the heat treatment processes, the steel was peeled and finally delivered in a

round bar.



Figure 2.4: A light microscope image of a cross section of P92 that illustrates the microstructure. The light areas represent the soft and ductile ferrite, the dark areas are composed of martensite.

For the experiments, samples were cut from the round blank with the dimensions $12 \times 12 \times 5$ mm^3. After cutting, they were grounded and polished to remove all surface damages and thermally induced defects/modifications from the cutting. The grinding or polishing started with SiC paper with a granulation of 80 and ended with 1 µm diamond paste. To end with a mirror finish was essential to guarantee a damage-free reference surface and therefore, to ensure that all investigated surface modifications and/or damages were generated by the exposure during the experiments.

3 Research facilities and analysing techniques

This chapter illustrates the test facilities that were used to investigate tungsten und ferritic-martensitic steel samples, as well as the techniques to analyse the exposed specimens. The first section introduces the experimental devices with their benefits and drawbacks. Unfortunately, no test facility exists that is able to simulate all the loading conditions expected in a fusion device simultaneously. Based on this circumstance, the abilities of two facilities were combined, to create conditions that were as close as possible to the expected loading parameters in a fusion device to get appropriate results. After the combined loading, the exposed samples were investigated by different analysing methods to examine not only surface modifications but rather changes of the bulk material. Based on these analyses, statements can be made about the damage behaviour and mechanisms as well as morphology changes, damage types and their influence on the material performance. The surface analyses were done via profilometry, scanning electron microscopy (SEM), and light microscopy (LM). To examine the bulk material, focused ion beam (FIB) techniques and metallography were used. All these techniques will be explained in the third section of this chapter.

3.1 JUDITH 1

The electron beam facility JUDITH 1 (**Ju**elich **Di**vertor **T**est Facility in the **H**ot Cells) at Forschungszentrum Jülich is located in a hot cell. This circumstance qualifies the test facility to investigate a wide range of materials, especially toxic and radioactive ones. It is not an exaggeration to claim that JUDITH 1 is a unique experimental facility for material testing. Besides the benefit to handle toxic and radioactive materials, it is capable to simulate steady state heat loads and transient thermal events as well as to handle various kinds of sample designs/geometries. In particular, the sample geometry can vary between large actively cooled components for screening or fatigue tests and small samples for thermal shock tests. Figure 3.1 shows a schematic sketch and a photo of the machine while table 3.1 summarises the main machine parameters [67, 68].

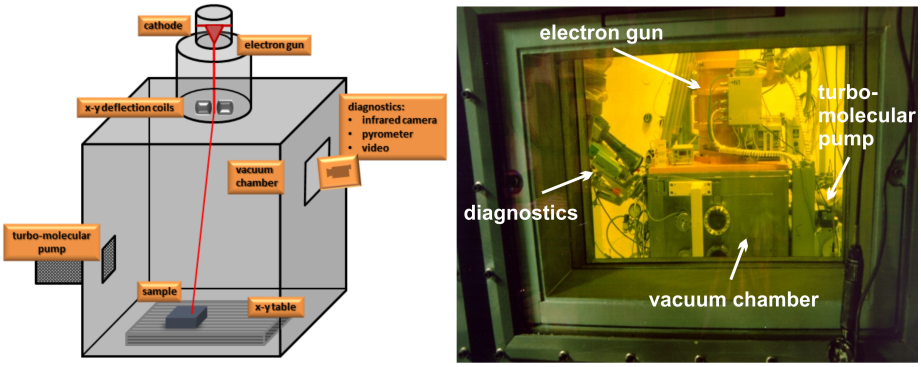


Figure 3.1: JUDITH 1 as a schematic on the left side and on the right side a photo of the device.

The electron beam facility consits of an electron beam gun with a maximum power of 60 kW that is equipped with a high frequency deflection system, a vacuum chamber (dimension 800 × 600 × 900 mm^3) and several diagnostic systems like a fast pyrometer, an infrared pyrometer, two colour pyrometers, thermocouples for the cooling water, calorimetry and infrared as well as visual cameras. Before an electron beam can be generated, the chamber has to be evacuated and afterwards a tungsten cathode emits free electrons which are accelerated (voltage $\leq$ 150 kV) and focused by magnetic coils.

Table 3.1: Main machine parameters of the electron beam facility JUDITH 1.

machine parameters	
acceleration voltage	$\leq$ 150 kV
beam current	$\leq$ 400 mA
beam power	$\leq$ 60 kW
beam diameter	$\approx$ 1 mm
pulse duration	1 ms – 100 ms, 120 ms to continuous
max. loaded area	100 cm^2
scanning frequency	$\leq$ 100 kHz in x/y-direction

The working pressure for the beam generator system is 10^{-5} mbar and for the sample chamber 10^{-4} mbar [67, 68]. Actively cooled components can be connected to the cooling circuit of the machine (maximum flow rate of 60 l/min). The electron beam has a diameter of $\sim$ 1 mm (FWHM) and by using deflection coils this beam can be deflected to scan the samples with frequencies of up to 100 kHz in x- and y-direction. The maximum possible area that can be scanned is 100×100 mm^2. The following figure 3.2 illustrates the beam path of a 1 ms electron pulse [63, 69].

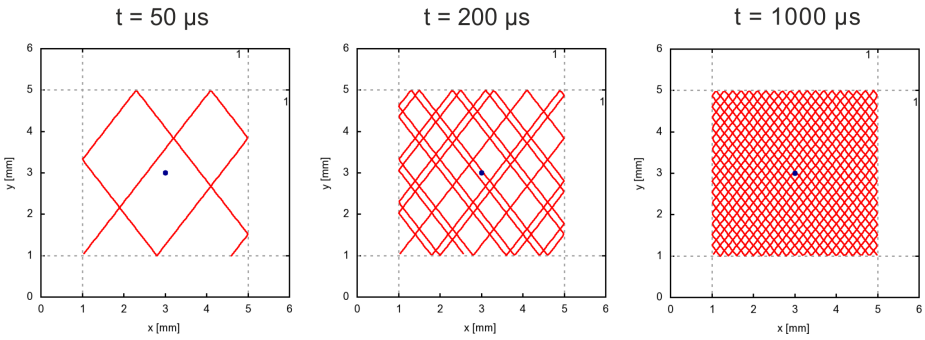


Figure 3.2: The electron beam path (1 ms pulse) of a 4×4 mm^2 loaded area after 50 µm, 200 µm, and 1000 µm [63, 69]. The combination of high and odd frequencies for both directions lead to a homogeneous loading.

The high scanning frequencies and the choice of odd frequencies for both scanning directions facilitate and ensure that the samples are loaded homogeneously. The maximum beam deflection in xy-direction that is achievable is $\pm$ 5 cm at the nominal acceleration voltage. For experiments with the intention to simulate thermal shock events, short pulse durations between 1 ms and 100 ms are used (capacitor mode). These short pulses are generated by a charged capacitor with a pulse rise and fall time of 100 µs. In addition, JUDITH 1 enables the opportunity to run experiments with longer pulses or even with continuous operation (transformer mode) [67].

Furthermore, the acceleration voltage U_a in correlation with the beam current I, that can be varied $\leq$ 400 mA, result in the electron beam. For normal operation U_a is 120 kV, yielding an electron beam energy of 120 keV. These electrons have a penetration depth of $\sim$ 7 µm in tungsten and lead to a volumetric heating within a thin layer. In this layer 95 % of the absorbed electron energy is deposited. It follows from the statement above, that the absorbed power density P_{abs} is not only derived by the acceleration voltage U_a and the beam current I but also by the electron absorption coefficient ϵ of the material. This electron absorption coefficient depends on the respective material and the electron interaction with it. The coherence between the specific physical values is given in the following equation:

$$P_{abs} = \frac{U_a \cdot I \cdot \epsilon}{S} \tag{3.1}$$

with S as the loaded surface area. When the electrons hit the surface of the sample, their energy is converted into heat and excitation energy of the target atoms. Nevertheless, not the whole incident electron energy is deposited in the material due to losses by backscattered electrons, reflected primary electrons, secondary electrons and thermionic electrons. To get an applicable value of the electron absorption coefficient ϵ that includes all the aforementioned losses, measurements, Monte-Carlo-simulations [70], and an experiment [63] were realised and compared with the values of 0.5 [71] and 0.62 [72] that were found in the literature. Consequentially, the electron absorption coefficient ϵ for electrons in tungsten that was used for the experiments was 0.55. For the experiments on ferritic-martensitic steel samples, an absorption coefficient of 0.75 was used.

3.2 PSI-2

The linear plasma generator PSI-2, originally constructed at the Humboldt University in Berlin and since 2009 located at Forschungszentrum Jülich, is adapted for the simualtion of well-defined cold edge (divertor) plasmas and transient events like ELMs, as they are expected in future fusion devices like ITER or DEMO, and, therefore, appropriate to investigate the influence of the plasma on the material (composition, hydrogen inventory, etc.), synergistic effects of particle and transient thermal loads, and in general plasma wall interactions.

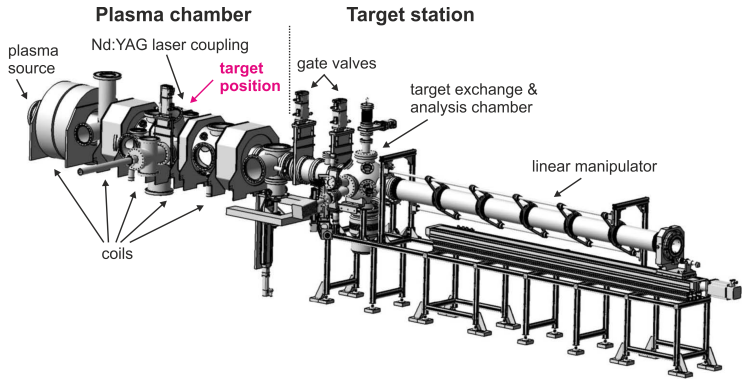


Figure 3.3: Schematic view of PSI-2 with the most important components [73]. The plasma source can be operated with different gases or a mixture of them. The position of the samples in the plasma chamber during the experiments is highlighted in red. The plasma chamber is ~ 3 m long (complete device ~ 6 m).

PSI-2 (see figure 3.3) consists of an vacuum chamber, a target exchange and analysis chamber, a Nd:YAG laser with an energy of 32 J for the ELM simulation, six cylindrical magnetic coils, a linear manipulator, several diagnostics, a visual camera and several connections for different gases like deuterium, helium and argon that are used for the plasma production. To operate the plasma source ideally, a working gas flow of at least 10 - 100 SCCM (SCCM = standard cubic centimeters per minute at standard temperature and pressure) is necessary to create a gas pressure of a few Pa. All experiments were performed under vacuum with an initial pressure between $10^{-7} - 10^{-8}$ mbar [73]. Table 3.2 lists the main machine parameters.

Table 3.2: Main machine parameters of the linear plasma generator PSI-2 [73].

machine parameters	
magnetic field at target exposure region	100 mT
plasma flux density on a sample	max. 10^{23} $m^{-2}s^{-1}$
plasma diameter	$6 \cdot 10^{-2}$ m
power flux density	≤ 2 MWm^{-2} with electrical biasing
energy of incident ions	≤ 200 eV (with electrical biasing)
stationary magnet field	0.1 T in the exposure chamber

The radial profile of the plasma flux, electron temperature, and electron density can be measured by a moveable Langmuir double probe. The Langmuir probe is located at the top of the target exposure chamber, moves with a velocity of 15 mm/s, and scannes with a frequency of 100 Hz. Moreover, the size of the probe tip (1.5 mm) determines the resolution of the measurement [73]. Figure 3.4 shows measurements of a) the plasma flux and b) the electron temperature.

Furthermore, an optical emission spectroscopy and an in-situ quartz microbalance (QMB) system are installed for the characterisation of the main plasma as well as erosion and re-deposition measurements. A Thomson scattering system is under construction. Moreover, the hollow plasma profile has to be taken into account concerning the distribution of the samples on the sample holder to ensure a homogenous plasma exposure. In addition, the sample temperature is controlled by thermocouples and an infrared camera. A bias on the sample holder $\leq$200 V leads

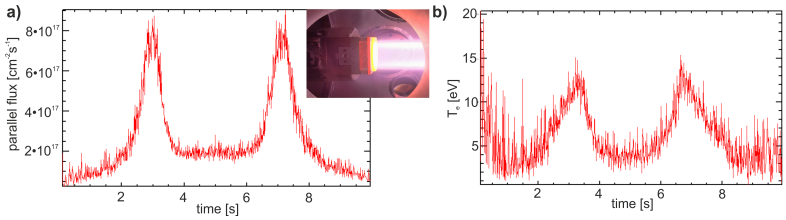


Figure 3.4: An example of a Langmuir probe measurement of a pure deuterium plasma. Measurement a) shows the plasma flux that clearly reflects the hollow profile, while measurement b) indicates the electron temperature. The small picture shows the deuterium plasma onto the sample.

to a potential difference to the plasma to adjust plasma energy.

For experiments simulating transient events, a Nd:YAG laser (neodymium doped yttrium-aluminum-garnet laser) provided by LASAG Industrial-Laser with a wavelength of 1064 nm and an energy of 32 J was used. Figure 3.5 illustrates the laser setup, the pulse wave form of the laser, and the spatial distribution of the power deposition [23].

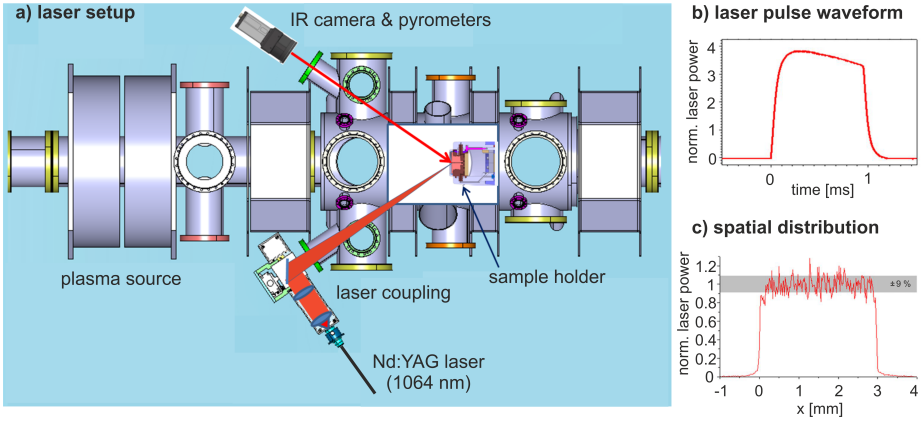


Figure 3.5: The figure shows a) the laser coupling with the device in detail, b) the above mentioned temporal laser beam profile that was measured by a fast photodiode and has nearly-square shape (due to reflections in the fibre-optic), and c) the spatial distribution of the power deposition in the loaded area [23].

The Nd:YAG laser is connected via an optical fiber with the device and strikes the sample surface under an angle of $\sim 38°$. This angle has to be taken into account by calculating the absorbed power densities due to the fact that the area of an ellipse has to be used for the calculations instead of the area of a circle. In detail,

the laser spot has a diameter of around 3 mm, which means that for calculating the area of the ellipse the semimajor (1.82) and the semiminor (1.43) have to be used. Furthermore, the laser light is not visible for the human eye because it is in the infrared range. To align the laser spot to the desired position a pilot He-Ne-laser with a wavelength of $\sim$ 640 nm, which takes the same beam path, was used. Another important fact is that the beam profile is not constant (spatially and temporally) but due to the reflections in the fibre-optics it can be considered as a box profile with constant intensity, which is necessary for the determination of the beam intensity. In addition, there is a loss of the laser beam energy of $\sim$ 10 % due to the optical path through the lenses and the window and consequently the resultant transmittance is T = 90 %. Moreover, $\sim$ 60 % of the transmitted energy is reflected at the sample surface, which was measured by a reflectometer so that the laser absorption rate is 40 % in total. The laser absorption rate (40 %) was taken into account for the determination/calculation of the absorbed power densities. It should be mentioned that the absorption rate of the laser does not change even if the roughness of the sample surface increases [74] as long as no nanostructures (like tungsten fuzz) grow. The reason for that is that nanostructures like tungsten fuzz change the surfaces emissivity drastically in a way that the surfaces become completely black and, therefore, the reflectivity decreases tremendously.

3.3 Analysing techniques

To evaluate the experiments and to get appropriate results, several analysing techniques with different advantages were used that will be described in detail in the following subsections.

3.3.1 Laser profilometry

Laser profilometry is an adequate technique to measure and characterise the surface morphology. Therefore, a laser profilometer by the OPM GmbH with a wavelength of 660 nm was used. The reflected laser light delivers information about the surface properties of the scanned area with a maximum size of 50×50 mm^2. Moreover, not only the dimension of the scanned area but rather the resolution can be adjusted individually, whereby the maximum lateral resolution is limited by 2000 points per mm and the pinpoint accuracy for each point is 20 nm. The laser profilometer facilitates altitude profile measurements up to $\pm$ 500 µm and the determination of the surface roughness. The arithmetic mean roughness R_a is defined as the mean deviation from the average height.

3.3.2 Scanning electron microscopy (SEM)

A scanning electron microscope (SEM) uses a focused, high-energy electron beam to generate signals produced by electron-sample interactions that reveal information about the scanned sample. In detail, these signals include secondary electrons (SE) that deliver an impression of the topography and morphology of the scanned surface, backscattered electrons (BSE) that carry information about the chemical composition and are most valuable for illustrating contrasts, diffracted backscattered electrons (EBSD) that are used to determine crystal structures and orientations. A SEM produces even more types of signals like photons of characteristic X-rays that can be used to identify the composition of a sample and to measure the abundance of elements. For imaging the exposed samples, especially to get a closer look on cracks, crack networks, and other originated structures and to analyse the crack parameters like crack distance and crack width, SE and BSE are commonly used.

3.3.3 Electron backscatter diffraction (EBSD)

The electron backscatter diffraction (EBSD), a crystallographic characterisation technique, is used to investigate the crystal orientation of a material, illustrate global and local textures, defects, grain morphologies, and also deformations. Therefore, a sample, which should be polished or at least flat to get reliable and accurate EBSD results, is placed into the SEM chamber where the electron beam is focussed onto the sample surface. When the electrons enter the sample, they will be backscattered from the atomic lattice, and some will match the Bragg conditions and diffract.

Thus, Kikuchi bands will form, which correspond to each of the lattice diffracting crystal planes and which can be individually indexed by Miller indices. These data are used to describe not only the crystal phase and/or orientation but also to generate different kind of maps to visualize/describe grain orientations, and grain boundaries etc..

3.3.4 Focused ion beam (FIB)

A focused ion beam (FIB) operates in a similar manner as a scanning electron microscope except that a FIB system uses a focused beam of ions. Here, liquid metal ion sources are used, particularly gallium ion sources. The beam current varies, depending on the desired investigation. That means in detail, for imaging low beam currents are used while the high beam currents are convenient for sputtering or milling. Within the frame of this work, the focused ion beam was used for the removal of material to investigate locations of special interest. This location-dependent removal of the specimen down to a submicron scale facilitates the study of induced damages and modifications on the bulk material without cutting the hole sample or impairing the exposed surface.

3.3.5 Metallography

The metallography facilitates the analysis of the microstructure of the material as well as the precise characterisation of the induced damages. To prepare a sample by metallography means it was cut by a diamond wire near the requested cross section line and afterwards embedded in epoxy resin. The embedded pieces were grounded with SiC paper (granulation 80-500) and polished with diamond paste starting with 6 µm particle size and finishing with 0.25 µm. Accordingly, the cross sections were etched with a solution composed of NH_3, H_2O_2 and pure H_2O (ratio 1:2:7). The light microscope (LM) images taken before and after etching provide the opportunity to analyse and evaluate crack widths, crack depths and additional modifications of the material.

4 Performance of tungsten under normal operation scenarios

As described in the introduction, the harsh conditions in a fusion device make high demands on the PFMs. Even under normal operation scenarios, the PFMs will be bombarded by vast heat and particle fluxes [40, 49, 75, 76]. To give an evidence about the performance of the materials and, therefore, the lifetime of the PFCs, tests are essential that cover all anticipated exposure parameters in a fusion device. Admittedly, such all-embracing experiments are inherently difficult to realise. Nevertheless, this section deals with comprehensive tests investigating the combination of various loading parameters. The following subsections will first describe the experiments and afterwards, the results will be discussed. They will be compared in terms of the influence of sequential loadings on the thermal shock behaviour of tungsten, possible changes of the morphology of the material, a potential influence of the different base temperatures on the performance of tungsten and consequential risks regarding the proposed area of application.

4.1 Summary of previous experiments

This section provides a summary of the significant results of former pure thermal experiments [61, 62], to render the conjunction and dependence to the sequential tests that will be illustrated and explained in the following sections. The sheer thermal experiments in [62] were executed in the electron beam facility JUDITH 1 and the linear plasma device PSI-2. The aim of these experiments was a broad characterisation of the used tungsten grade and the investigation of the performance under ITER relevant thermal loading conditions as well as to provide mappings of the investigated surface modifications and damages in dependence on the loading parameters, so called damage mappings. The used tungsten grade was already described in detail in section 2.1. Furthermore, the experiments were executed with identical conditions for comparison with the electron beam and the laser beam. In detail, 100 and 1000 pulses were applied with a repetition frequency of 0.5 Hz, a pulse duration of 1 ms, absorbed power densities in the range of 0.19 GW/m² up to 1.13 GW/m², and at different base temperatures, room temperature (RT), 400 °C and 600 °C (only for laser tests). The following subsections will illustrate the main

results of both loading types.

4.1.1 Results of the electron beam tests

The electron beam tests affiliate to former experiments [61], which were performed on the same material with similar loading conditions. To enlarge and complete the analysis of the damage behaviour and performance of double forged tungsten under transient events simulated with an electron beam that were started in [61], only samples with a transversal grain orientation were tested at RT and 400 °C. Taking all results [61, 62] into account, the damage threshold was found to be between 0.19 GW/m² and 0.38 GW/m². Tests at 0.19 GW/m² did not cause any change of the surface morphology, while power densities above 0.38 GW/m² led to significant changes or damages of the samples in dependence on the base temperature. Moreover, the base temperature influenced the mechanical properties. This effect can be described by a second threshold, the so-called cracking threshold. This threshold was determined to be between 200 °C and 400 °C. In addition, experiments at base temperatures up to 200 °C and power densities above 0.19 GW/m² caused large cracks and crack networks. However, samples with a transversal grain orientation showed a brittle behaviour even at 400 °C by the formation of small cracks, whereas samples with a longitudinal grain orientation and recrystallised samples did not crack at this base temperature. The deviation could be provoked by the microstructure and consequentially weaker mechanical strength, but statistics is not large enough to draw unambiguous conclusions. Nevertheless, due to the broad range of tested parameters and the high consistency of the results, these data provide a useful database for the layout and design of PFCs for future fusion devices. By increasing the base temperature up to 400 °C and higher, the ductility of tungsten increased so that induced stresses were compensated by plastic deformation. In general, the higher the power density the higher the surface roughness when exposed at constant pulse numbers.

4.1.2 Results of the laser beam tests

The experiments determined that the damage and cracking thresholds (only for tests with 100 pulses) were constant for all three sample types. Surface modifications and/or damage did not occur for absorbed power densities of 0.19 GW/m² and below. For recrystallised samples, the damage threshold was located even between 0.38 and 0.76 GW/m² at RT. The cracking threshold, which depends on the mechanical properties of the material, like yield and tensile strength, was located between 100 °C and 400 °C. Accordingly, the DBTT of tungsten played an important and decisive role. Furthermore, only tests at RT and with absorbed power densities above 0.19 GW/m² caused large cracks and crack networks, while experiments at a base temperature of 400 °C and higher only led to surface modifications that became

more distinct with increasing the power density and pulse number. This observation is reasoned by the ductile behaviour of tungsten at elevated temperatures. In summary, the tests at RT led to pronounced crack networks, at which the cracks first propagated preferably perpendicular to the loaded surface into the bulk material up to a certain point and from that point on the propagation was horizontal. Concluding, the surface roughness was most pronounced after 1000 laser pulses at the highest tested power density, where the material had to compensate the highest stress. In addition, the high plastic deformation of certain areas within the loaded area decreased the thermal contact to the bulk material conspicuously and provoked partially molten areas.

In conclusion, the analysis of the results showed that there was no significant difference, as a function of the laser and electron beam loading, in the performance or thermal shock behaviour of the tested tungsten grades. The slight deviation of the damage threshold of recrystallised samples at RT was found to be negligible. Furthermore, the minor differences in the crack pattern and surface modifications were generated by the simulation method of the ELM-like events. The electron beam scanned the samples surface to achieve a roughly homogenous loading, but this scanning damages the material faster. In contrast, each laser pulse exposed the surface homogenously. Also, the penetration depth varied depending on the simulation method. In detail, the penetration depth of electrons in tungsten is about a few µm, while the light decay length is about 20 nm and, therefore, negligible [63]. Moreover, the geometric differences of the loaded area as well as the diverse beam profiles had to be taken into account. The electron beam scanned an area of 4×4 mm^2 with a Gaussian beam profile of approx. 1 mm FWHM, whereas the laser exposed a circular area ($\varnothing \sim 3$ mm) with an approximately rectangular beam profile (see section 3.2). These distinctions, the volumetric heating of the electron beam and the near-surface exposure of the laser, resulted in varying thermal stress distributions and gradients, especially at the edges of the exposed areas, which caused the differences in the observed surface modifications and crack pattern.

4.2 Sequential and simultaneous experiments with deuterium plasma

The following experiments represent the continuation of the afore outlined tests. In detail, sequential and simultaneous thermal and particle loads were executed to achieve more realistic fusion relevant loading conditions. Therefore, pure deuterium plasma was used for particle loads while the thermal loads were exerted by laser beam. Of course, the test conditions were varying to these occurring in ITER, concerning the base temperature, the missing particle loads during the transients, and the two order of magnitude lower particle load for the steady state conditions.

However, as mentioned before, experiments that cover all anticipated exposure parameters are inherently difficult to realise. The experiments were performed at different base temperatures in the linear plasma generator PSI-2. Moreover, to ensure an meaningful comparison, all experimental parameters like sample geometry, pulse duration, repetition frequency etc., were retained except the base temperature.

4.2.1 Sequential and simultaneous tests at 400 °C

The first series of experiments investigating the impact of sequential and simultaneous thermal and particle loads were done at 400 °C base temperature. They were performed on industrially available, double forged pure tungsten, which was described in section 2.1 and also used during the tests in section 4.1. The intention for these experiments was not only to investigate whether the thermal and particle loads cause damage and/or influence the material performance in general, but also to clarify if the sequence of exposure has an influence. If the sequence of exposure shows no influence, future experiments would be much easier.

The experimental conditions were chosen according to the expected parameters in the divertor region in ITER [16,21] and with the involvement of the results of former experiments, which were performed in [61,62,77,78]. Samples with longitudinal (L) and transversal (T) grain orientation to the surface were tested, as well as the same material in the recrystallized state (R). The surfaces were prepared as described in subsection 2.1 and all samples had the dimensions $12 \times 10 \times 5$ mm^3 and were mechanically clamped to an actively cooled sample holder equipped with an ohmic heater that ensured that the specimens were heated to a base temperature of 400 °C, which was measured by a thermocouple. In addition, a torque wrench was used to guarantee a uniform torque of the mask and, therefore, the same thermal contact for each experiment. Figure 4.1 shows a sketch of a sample, the target holder, and an equipped target holder with mask.

The samples were mounted in a circular arrangment due to the hollow plasma profile already mentioned in section 3.2. Furthermore, the laser simulated the transient events with a repetition frequency of 0.5 Hz and a pulse duration of 1 ms. Thereby, the absorbed power densities covered a range of 0.19 GW/m²- 0.64 GW/m² that led to a temperature rise ΔT $\sim$ 350°C per pulse for the lowest and a ΔT $\sim$ 1300 °C per pulse for the highest power density. For each sample type (T, L, R), three samples were tested, one with 0.19 GW/m², one with 0.38 GW/m², and one with 0.64 GW/m². The particle exposure was realised by a pure deuterium plasma with a flux of $\sim\ 6 \cdot 10^{21}$ m^{-2}s^{-1} and a fluence of up to $\sim 1.2 \cdot 10^{24}$ m^{-2} corresponding to 100 laser pulses ($\sim 1.2 \cdot 10^{25}$ m^{-2} corresponding to 1000 laser pulses). The particles were accelerated with a bias voltage of - 60 V towards the sample, resulting in an incident ion energy of 35 eV.

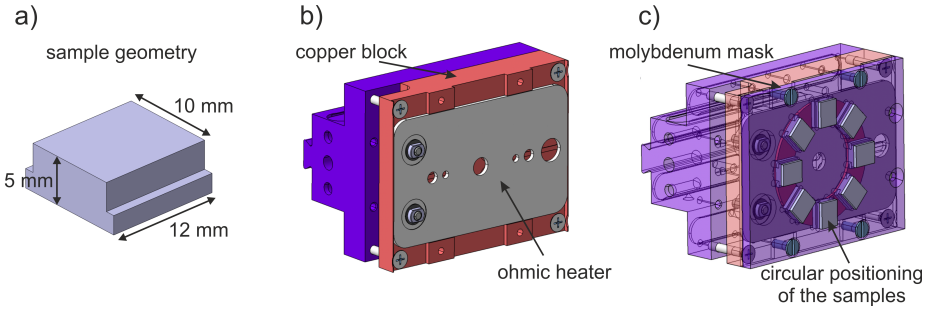


Figure 4.1: Sketch a) shows the sample geometry. The steps on two sides of the sample ensured that the specimens jutted out the mask. In picture b) the actively cooled sample holder with the ohmic heater is shown and in c) the equipped target holder with the molybdenum/tungsten mask. The circular positioning of the samples took the hollow profile of the plasma into account and therefore, guaranteed a uniform exposure [79].

After the tests were conducted, each sample held four exposure spots, where the power density and plasma parameters were retained but the loading sequence and the pulse number were changed. In detail, the first spot was first exposed to 100 transient thermal events and subsequently exposed to plasma. During the thermal shock exposure, the ohmic heater was used to achieve the required base temperature. On the second spot the loads were applied simultaneous and the energy entry of the plasma was sufficient to raise the temperature to 400 °C. Furthermore, the third and fourth exposure point saw initially the plasma followed by 100 thermal pulses on the third and 1000 pulses on the fourth spot, respectively. The loading procedure is visualised in figure 4.2.

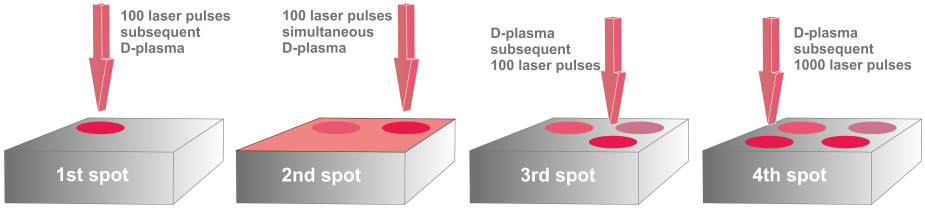


Figure 4.2: A schematic illustration of the loading sequence. Each sample held four exposure spots with a fixed power density, repetition frequency, and pulse duration but an altered order of the thermal and particle loads, as well as the pulse number for the fourth spot. The base temperature was kept constant at 400 °C for each loading sequence.

This method offerd the opportunity to study the influence of the hydrogen as well as

of the samples microstructure and certainly, the order of exposure on the material's thermal shock performance simultaneously. After the experiments, the induced damages and surface modifications were analysed by laser profilometry, light microscopy, scanning electron microscopy (SEM) and cross sections, which were made metallographically and with the focused ion beam (FIB).

Results and discussion

The analysis revealed that there were significant differences of the surface morphology and damage structure depending on the loading sequence, applied power density, pulse number, and sample type. First, the results of sequences, which were executed with 100 transient events, are examined and compared for the three samples types and different absorbed power densities.

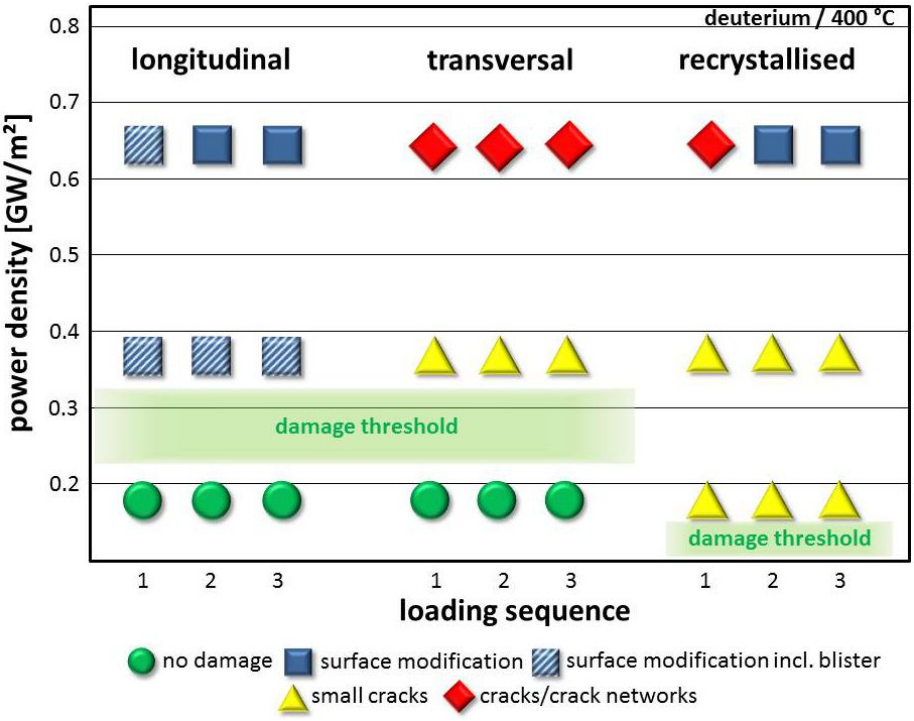


Figure 4.3: Mapping for all tested samples types of the worst observed surface modifications and damages in dependence on the loading sequences with 100 laser pulses and the power density.

Starting with L samples, figure 4.3 illustrates a damage mapping that depicts all investigated damage types devided into five groups. Each group is represented by a

different symbol and colour. Thereby, a green circle indicates that the exposure did not cause observable damages or changes in the surface morphology. Furthermore, loadings that are indicated by a blue square led to surface modifications like swelling and/or roughening, in the case of a blue-striped square this surface modifications involved also blisters. The last two groups involved additionally small cracks (yellow triagle) and cracks/crack networks (red diamond). Here, the inherent difference is that small cracks are arbitrarily and isolated distributed in the loaded area. In addition, they are barely visible to the naked eye, which implies a smaller crack width.

L samples compensated the stresses caused by transient thermal events solely by plastic deformation independent of the loading sequence and power density. First, compressive stresses were induced by each laser pulse that entailed an expansion of the grains, which was prevented by the colder surrounding material. In the cooling phase after each laser pulse, the grains shrank and the compressive stresses were converted into tensile stresses. Confirmed by the results that with increasing power densities the surface roughness rose but cracks were not observed, the ductility of the material was high enough to prevent cracking or rather the tensile strength was larger than the generated tensile stresses. The surface roughness increase was revealed by laser profilometry measurements, the corresponding measured R_a values are given in table A.1 in appendix A.1. Based on the above-quoted results, a damage threshold was defined between 0.19 GW/m² and 0.38 GW/m². This threshold illustrates that a power density of 0.19 GW/m² caused no damage contrary to a power density $>$ 0.19 GW/m². Furthermore, representative SEM images of the induced surface changes and damages are shown in figure 4.4.

In addition, experiments at the highest power density of 0.64 GW/m² caused distinct plastic deformation and delamination. In the case of delamination, the thermal contact to the bulk material was tremendously decreased, which in turn resulted in partial melting. Another consequence of pronounced deformation/delamination could be enhanced erosion or dust formation. Moreover, the order of loading in combination with the applied power density influenced the surface morphology, which became apparent by deuterium accumulations below the surface resulting in bubble nucleation, so-called blisters. Here, the deuterium clustered in intrinsic defects like dislocations and vacancies [44]. Additionally, the number and size of blisters varied greatly dependend on the exposure parameters mentioned before (see figure 4.4). In detail, the highest quantity of blisters was detected after initial loading with the laser beam at 0.38 GW/m^2 and subsequent exposure with plasma, which represents a power density slightly above the damage threshold. Here, the largest blisters had a major axis of 10 µm and the smallest of 2 µm. After simultaneous exposure at the same absorbed power density the largest blisters revealed a major axis of just 3 µm. No blisters were detectable after simultaneous exposure and initial plasma exposure followed by laser loads at 0.64 GW/m². Here, the pronounced surface roughening

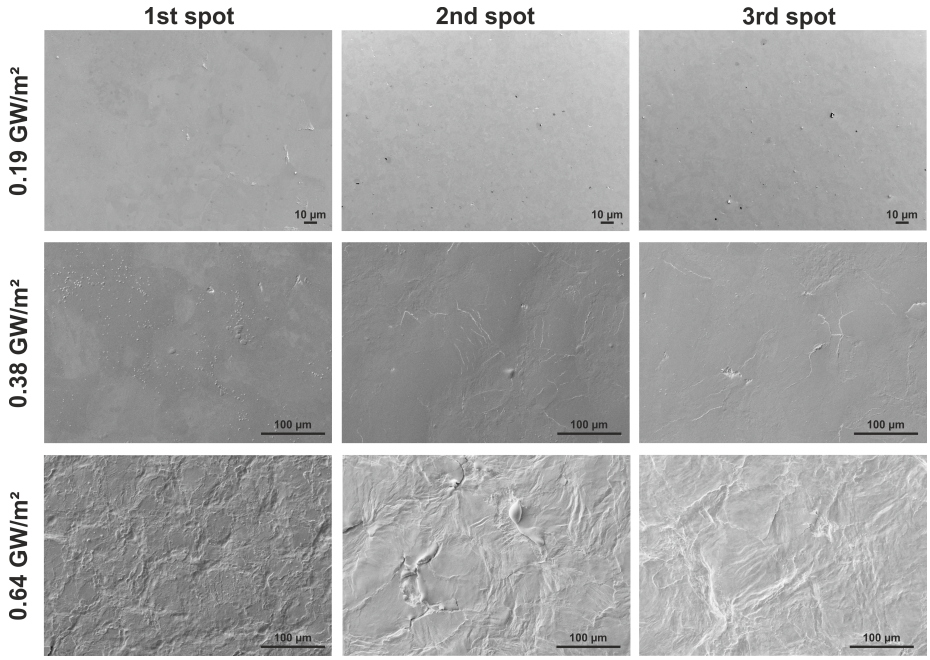


Figure 4.4: SEM images of the different exposure spots of sequences with 100 laser pulses for L samples. Not only the variation in the amount of blisters but the increase of the surface roughness as a function of the applied power density is pointed out.

prevented the observation of potential existing blisters or the blisters disappeared through the repetitive thermal stress cycles. The SEM images in figure 4.4 display the varying amount of blisters in dependence on the applied power density and loading sequence.

Deuterium agglomeration or blistering is influenced by a broad range of parameters. In detail, it strongly depends on the energy (some eV up to keV) and fluence of the impinging hydrogen ions, the manufacturing process and thermal treatment of the material, the microstructure, and the amount of trapping sites in the material [44]. Therefore, the observed difference in the number of blisters can be explained by the microstructure of the samples and the thermal generation of additional defects during transient events [23]. An additional reason could be the base temperature and/or temperature rise at each laser pulse that increased the mobility of trapped deuterium and caused a deeper diffusion into the material or degassing. This was confirmed by the result that simultaneous loads and sequences that terminated with transient events below (0.19 GW/m^2) and far above (0.64 GW/m^2) the damage threshold exhibited a small amount of blisters or no blisters. Moreover, the blisters

were arbitrarily distributed in the loaded area with the tendency to compose clusters within single grains. This observation is related to the crystallographic orientation of the material [80]. As stated in [81], grains with a direction close to ⟨111⟩, which means perpendicular to the surface, are more prone to blister formation.

In agreement with the results of the L samples, T specimens did not show any kind of surface modification or damage after experiments at 0.19 GW/m². Again, the damage threshold was located between 0.19 GW/m² and 0.38 GW/m² (see figure 4.3). Here, power densities above 0.19 GW/m² caused an increase of the surface roughness, led to blister formation, and resulted in the formation of small cracks and/or large cracks. The measured values of the arithmetic mean roughness R_a are listed in table A.1 in appendix A.1.

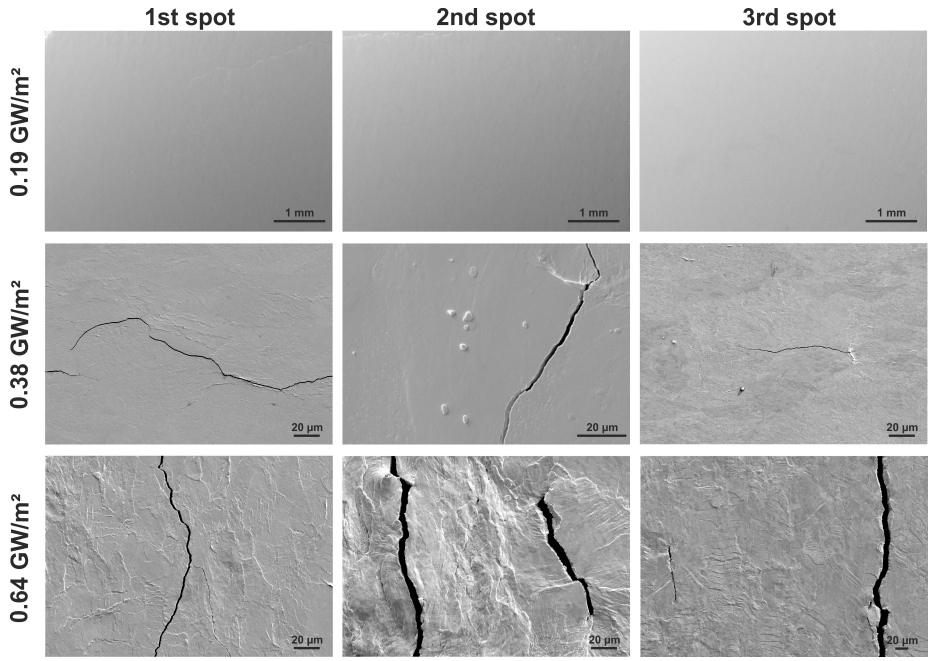


Figure 4.5: SEM images of the exposure spots of T samples after sequential and simultaneous loading at different power densities. From the top to the bottom row the absorbed power density increases, which is reflected in the enhancement of the surface modification and damage.

In contrast to L samples, the generated tensile stresses were higher than the tensile strength of the material, which resulted in crack formation for each sequence at power densities above 0.19 GW/m². Experiments at 0.38 GW/m² caused small cracks with a maximum average crack width up to 4 µm, after tests at 0.64 GW/m²

the highest value was ∼ 11 µm. A detailed list of all measured average values can be found in table A.2 in appendix A.1, while figure 4.5 illustrates representative SEM images of the generated surface modifications and damages. Furthermore, metallographical cross sections were prepared to analyse the propagation of these cracks into the bulk material and the crack depth. It became apparent that the cracks propagated almost solely along grain boundaries, which are the weakest parts of the microstructure, into the bulk material. Figure 4.6 illustrates exemplarily the crack propagation after tests at 0.64 GW/m².

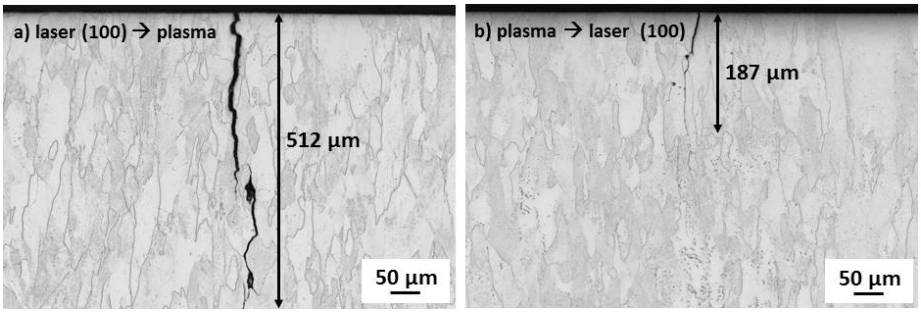


Figure 4.6: Crack propagation of an L sample after different sequences at 0.64 GW/m². Image a) shows the crack depth after initial exposure to 100 laser pulses and subsequently to plasma, in image b) a generated crack after plasma load followed by 100 transient thermal events can be seen.

In general, hydrogen reduces the critical stresses for crack formation and propagation, which is called hydrogen embrittlement [82]. Nevertheless, a correlation between the loading order, power density, and the crack depth was investigated. Tests at 0.38 GW/m² revealed that initial plasma exposure followed by laser beam loads generated the deepest cracks with an average crack depth of ∼ 17 µm. An explanation could be that due to the deuterium trapped by lattice defects like grain boundaries, vacancies etc., the stress level within the tungsten lattice was already higher in comparison with the other loading orders. Therefore, the subsequent exposure to thermal shock loads initiated additional stresses, which further increased the stress level and resulted in the deepest crack propagation. For experiments at 0.64 GW/m², the behaviour was the same but the sequence first laser exposure followed by plasma loading had to be examined separately. In this case, only one crack with a crack depth of ∼ 512 µm was observed, whereas for the other loading orders an average crack depth value based on several cracks was determined. Furthermore, the higher power density caused an increase of the thermal stresses and, therefore, of the strain rates in addition to the brittle behaviour of T samples in general, which is caused by the grain orientation.

The results depicted the influence of the microstructure on the material performance. The texture strengthening effect that was detected for L samples was missing in the case of T samples. Due to the grain orientation, T samples have a lower mechanical strength and a higher DBTT, which means they are more brittle. Apparently, the increase of the base temperature was insufficient to enhance the ductility and, therefore, to compensate induced stresses solely by plastic deformation. Furthermore, loading sequence and power density dependent blister formation was observed in coincidence with the L sample results, which means the highest amount of blisters was generated after initial laser exposure at 0.38 GW/m² followed by plasma exposure.

The analysis of R samples showed an increase of the surface roughness with rising power densities that was in the same order of magnitude like for L samples and almost twice as high like for T samples. The mean R_a values are given in table A.1 in appendix A.1, whereas figure 4.7 displays the surface morphology evolution for all loading orders and power densities.

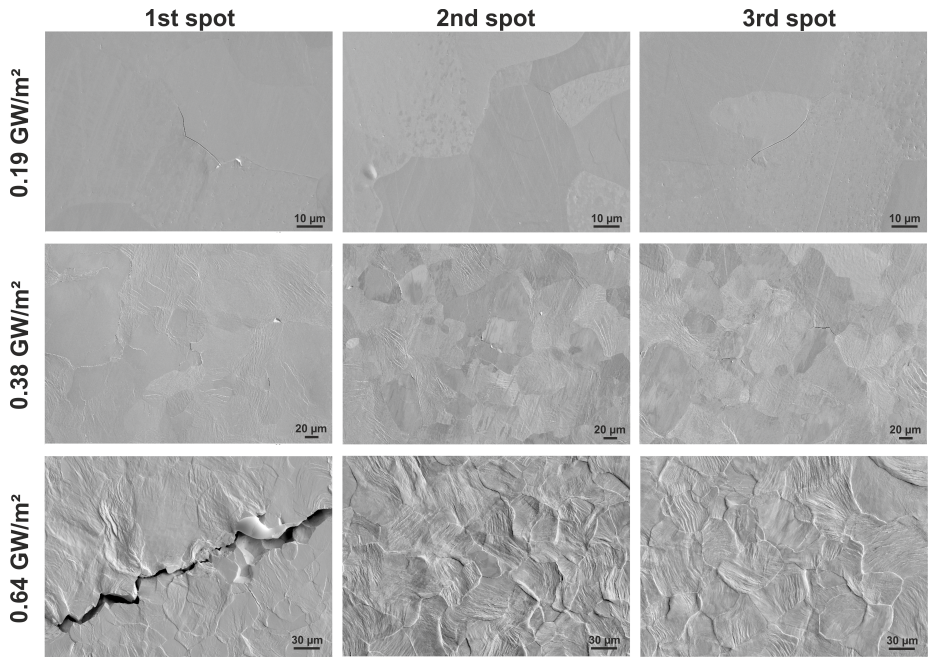


Figure 4.7: SEM images of the single exposure spots of R samples. Small cracks were investigated for almost each loading sequence and power density. The best damage performance was determined for experiments at 0.64 GW/m², which could be associated with a higher ductility of the material.

Besides the increase of the roughness, cracking occurred at almost all tested se-

quences (see figure 4.3, right column). Here, the damage threshold was located below 0.19 GW/m². This result indicated the weakest mechanical properties, which are affected by the microstructure [77] and, thereby, poor performance. As a result of the recrystallisation process, vacancies agglomerated at the grain boundaries, which in turn increased the open volume between adjacent grains [83]. This in turn decreased the cohesion between single grains, the ultimate tensile strength, and deteriorated the thermal shock and fatigue performance. The observed small cracks and large cracks were indiscriminately distributed in the loaded area. Thereby, the development was irrespective of the loading order but the crack width rose as a function of the power density. In particular, after experiments at 0.19 GW/m², the highest average crack width was $\sim$ 0.2 µm, while initial laser loads followed by plasma exposure at 0.64 GW/m² generated cracks with a maximum average width of 11 µm. Furthermore, the missing crack formation after simultaneous exposure and initial plasma exposure followed by laser loads at 0.64 GW/m² was hard to explain. An assumption could be that this was a statistical fluke. Here, further tests are needed to verify the results. All crack width values are given in table A.2 in the appendix A.1. By investigating the crack propagation into the bulk material accretive crack depths were monitored according to increasing power densities. The measured average depth values are given in table A.3 in the appendix A.1 and figure 4.8 exemplarily shows a cross section image of a crack that generated inside the material, which means the crack could not be detected on the loaded surface.

As it can be seen on the metallographic cross section in figure 4.8, substantial grain loss was observed after the cross section preparation, another indicator for the mechanical weakness of recrystallised tungsten. In general, the observed cracks propagated both perpendicular and horizontal to the loaded surface into the bulk material.

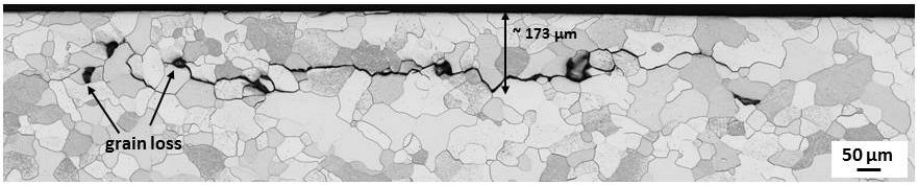


Figure 4.8: The light microscope image illustrates a cross section of an R sample after first plasma exposure followed by laser beam loading at 0.38 GW/m². A horizontal crack inside the material acts as thermal barrier and could lead to overheating and melting.

Especially the horizontal cracks are a serious problem due to the fact that they massively influence the thermal contact to the bulk material and thus, could cause overheating, melting, and in the worst case a loss of whole parts of the material. Regarding an application in a fusion device like ITER, the material loss could have

consequences for the proper functioning on grounds of plasma performance.

So far, only sequences with 100 laser pulses were investigated. The following part focuses on the damage evolution after experiments with higher pulse numbers. For this purpose, the sequences three and four were compared, which had the same loading order in common, first plasma and then laser, but distinguished between the number of laser pulses, 100 and 1000, respectively. The results are displayed in the damage mapping in figure 4.9 and in appendix B.1 figures B.1 - B.3.

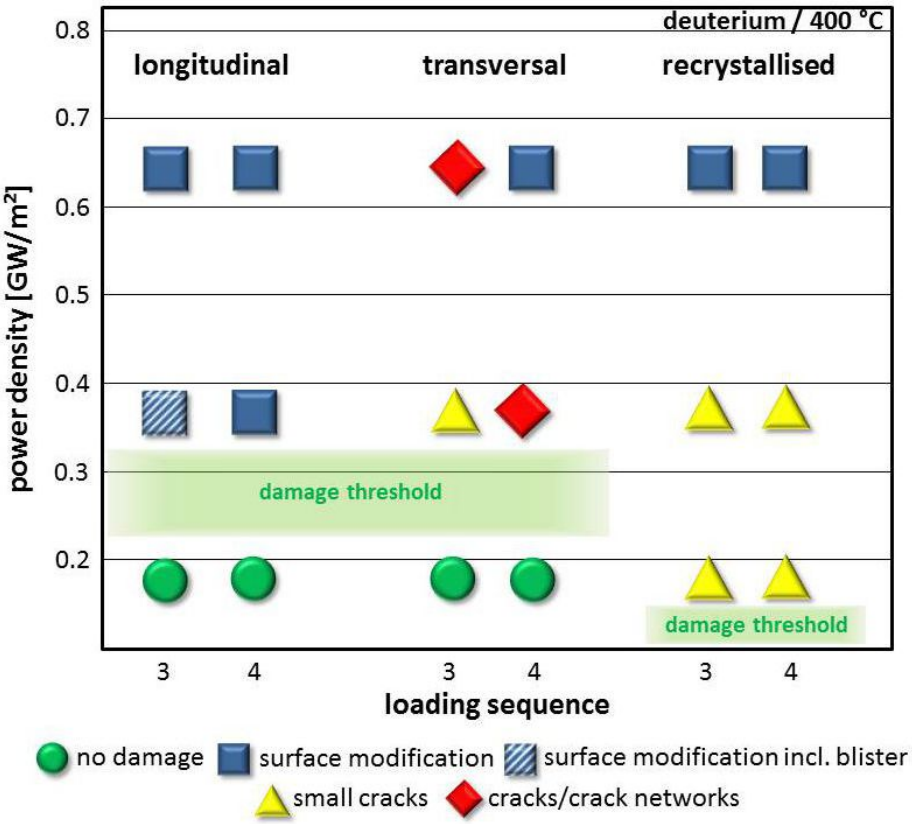


Figure 4.9: The damage mapping illustrates the different surface modifications and damages after sequences with initial plasma exposure followed by laser beam loads and varying pulse numbers. Sequence 3 was realised with 100 laser pulses, sequence 4 with 1000 laser pulses.

Laser profilometer scans revealed that the arithmetic mean roughness R_a was on the one hand higher in comparison with the sequence with 100 pulses (see table A.1 in appendix A.1) and on the other hand increased as a function of the applied

power density. The explanation for this accumulation of damage is the high degree of repetitive stress formation and the resultant pronounced plastic deformation. Furthermore, the thermal shock performance and damage behaviour of R samples remained unaltered, whereas L samples did not show blisters after 1000 laser pulses at 0.38 GW/m². Moreover, T samples generated cracks instead of small cracks after tests at 0.38 GW/m² that was ascribed to the higher amount of fatigue cycles. In contrast, after tests with 1000 laser pulses at 0.64 GW/m² the performance of T samples appeared to be improved. Due to the bare possibility of an improvement, on grounds of a higher number of stress cycles and power density, this result seemed to be a statistical fluke and further experiments are needed to verify the result.

Moreover, the amount of blisters decreased remarkably for all sample types to the point where no blisters were observed, which can be related to the temperature dependency of blistering. In detail, the larger quantity of applied laser pulses extended the time at elevated temperature (during and after each laser pulse), which affected the accumulation of deuterium in the near-surface region. In detail, the mobility of deuterium increased that led to outgassing or deeper penetration into the bulk material. In addition, a decrease in blister formation is prevailing at temperatures above 600 K [84]. Furthermore, the crack width and depth increased in comparison with 100 pulses driven by the compensation of the repetitive expansion and contraction and, therefore, the resulting plastic deformation was more distinct. In addition, the material degradation was reflected in grain nucleation and recrystallisation on L samples after loads at 0.64 GW/m² and up to a depth of 1.5 mm in the entire laser spot area ($\sim$ 3 mm²), which can be seen in figure 4.10 a). Microstructural changes like recrystallisation decreases the mechanical strenght and cohesion between single grains and this makes the material more prone to damage formation and erosion of near-surface grains [77]. Another observation was the significant increase of stress-induced plastic deformation, which led to thermal fatigue effects like partially molten parts that are illustrated in figure 4.10 b).

Another result was the formation of scale-like structures within the loaded surface, pictured in figure 4.10 c). These structures were only found on L and T samples for applied power densities above 0.19 GW/m² and after 1000 transient thermal events. Moreover, they were aligned in the same direction within single grains, therefore a relation linked to the crystal structure was assumed. However, EBSD analysis did not confirm this assumption of a connection between the crystal texture and the aligment. Furthermore, FIB cross sections revealed (figure 4.10 d)) that the structures were not pressed out grains/material. The explanation is that the highly pronounced plastic deformation led to delaminations of material, which in turn resulted in an immense degradation of the thermal contact. This lack of thermal contact to the bulk material caused overheating, melting, and afterwards, solidification and the formation of the investigated scale-like structures.

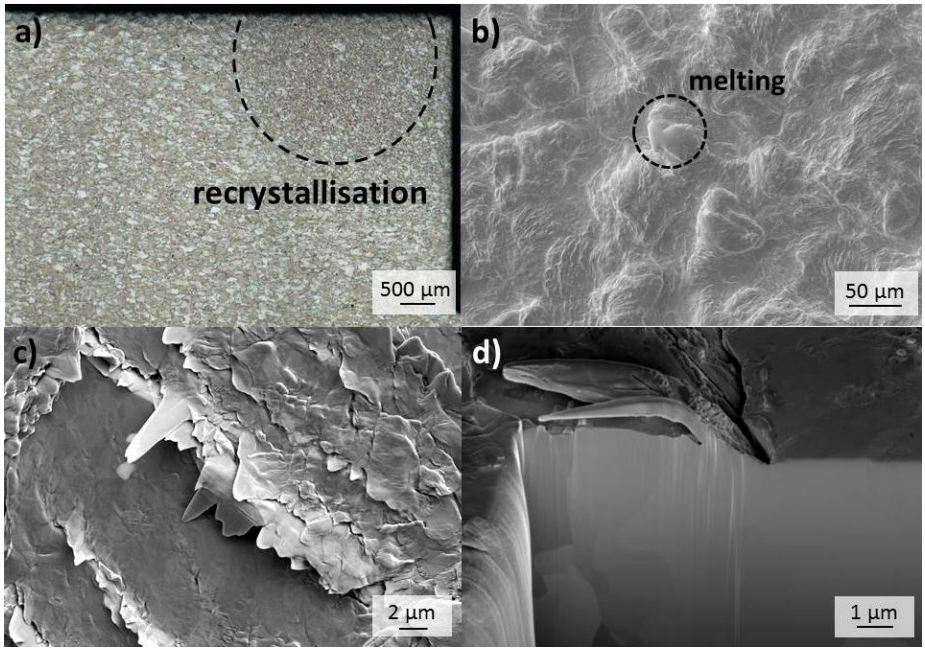


Figure 4.10: Image a) shows the recrystallised microstructure of a L sample after tests at 0.64 GW/m², b) illustrates selective melting after 1000 pulses, and at the SEM picture c) the scale-like structure within the loaded surface are shown that occured on L and T samples. For further investigations FIB cross sections were performed, one can be seen on picture d).

4.2.2 Sequential and simultaneous tests at 730 °C

To investigate if the base temperature measurably influences the performance of tungsten or mitigates the exacerbating impact of deuterium, the subsequently described sequential and simultaneous experiments were executed at 730 °C while all other loading parameters were maintained. The experimental parameters were already delineated in detail in subsection 4.2.1. Due to changes of the optical connection between the laser and the linear plasma generator the highest absorbed power density could be increased to 0.76 GW/m². Furthermore, the samples were mounted on a high temperature sample holder with ceramic spacers (figure A.1 in the appendix A.2). An ohmic heater was used again to achieve the required base temperature, which was monitored by a thermocouple. The following discussion of the obtained results will be started by sequences with 100 laser pulses before the damage evolution due to the pulse number increase will be explicated.

Results and discussion

After conducting the experiments, the samples were investigated by means of laser profilometry, SEM and metallography. L samples did not exhibit cracks or crack networks but the damage threshold shifted below 0.19 GW/m². The damage mapping, illustrated in figure 4.11, follows the preassigned damage categories and monitors the material performance. Thereby, a new category was added by a checked square that displays surface modifications that included pores and cavities.

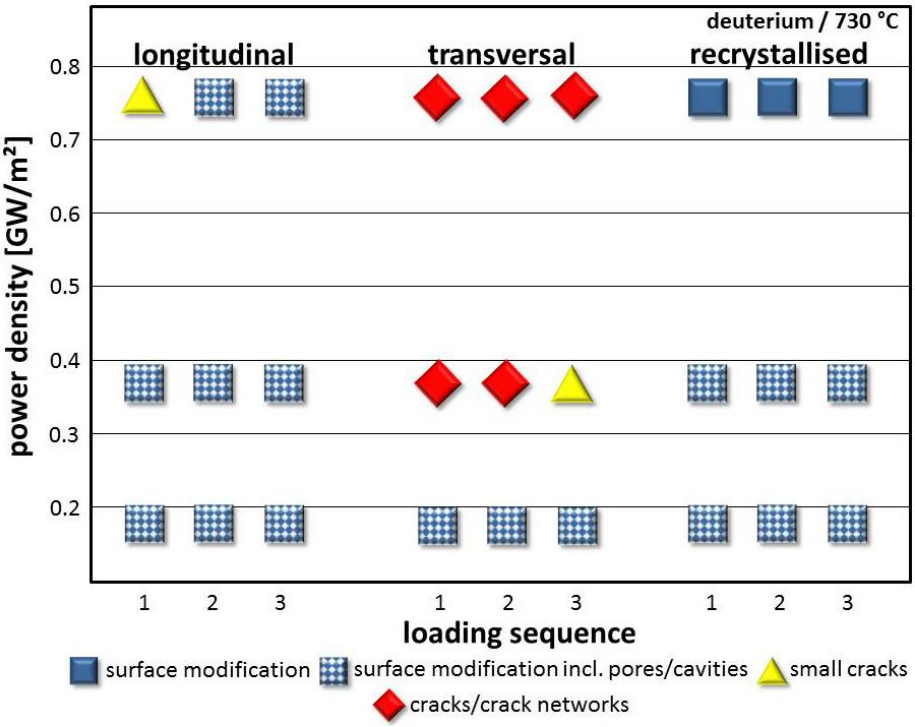


Figure 4.11: Surface modifications and material damage after sequential and simultaneous testing at 730 °C for all sample types. The damage thresholds shifted below 0.19 GW/m².

The arithmetic mean roughness R_a values (table A.4 in the appendix A.2) showed that the surface roughness increased in dependence on the applied power density but was not influenced by the exposure sequence. Furthermore, no blister formation was detected, which can be attributed to the base temperature and a reduced number of existing trapping sites [44]. The high base temperature in combination with the temperature rise during each thermal event decreased the amount of trapping sites and, therefore, the retained deuterium in the near-surface region, which can be confirmed

by the fact that maximum deuterium retention takes place between 450 and 850 K as stated in [85–88]. Instead of blisters, pores and cavities occurred for each loading sequence and power density with an interrelation between the applied power density and the observed amount. Precisely, the lowest power density of 0.19 GW/m² provoked the highest quantity of pores/cavities that declined with increasing power densities. Moreover, the pores and cavities were arbitrarily distributed in the loaded area but numerously represented on single grains. This fact can be explained by the preferential crystal orientation for blistering, described in subsection 4.2.1, accompanied by the high amounts of outgassing deuterium at temperatures above 850 K. The high quantity of degassed deuterium resulted in material loss and finally the formation of pores and cavities [18, 89]. Figure 4.12 shows exemplary SEM images of L samples after loading sequences with 100 laser pulses at different power densities.

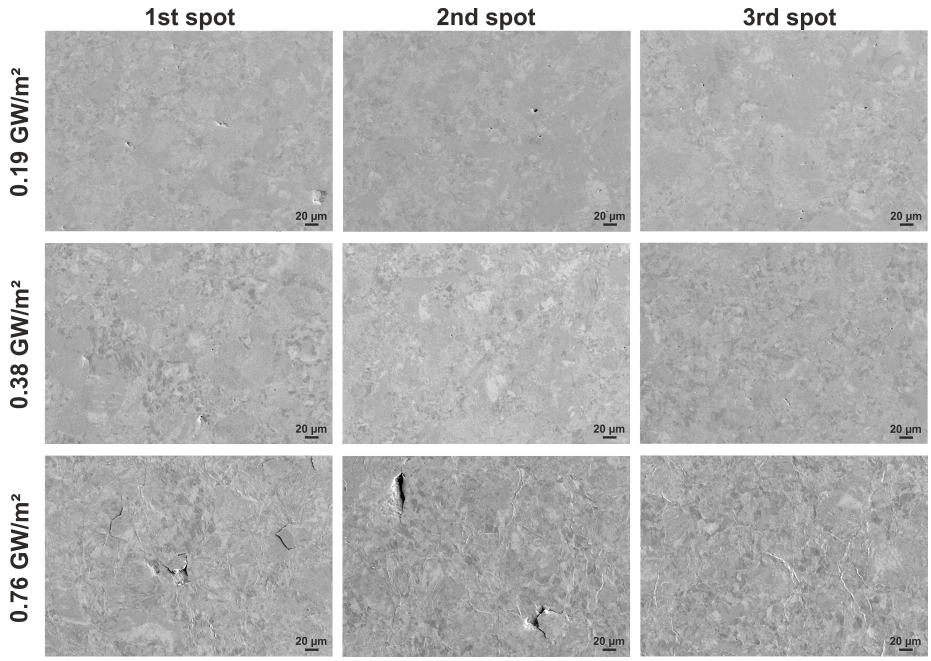


Figure 4.12: SEM images of the single exposure spots on L samples after sequences with 100 laser pulses. At 730 °C base temperature blistering was not detected but then pores/cavities were formed. Their amount decreased with increasing power densities.

Furthermore, laser loading followed by plasma exposure generated small cracks in the loaded area. These small cracks were extremly shallow and therefore, not visible in metallographic cross sections. An exemplary cross section image is shown in figure A.2 in appendix A.2. However, cross sections revealed grain nucleation (first image

in the top row in figure A.2 in appendix A.2) that was observed for all loading sequences, power densities, and all sample types (not only for longitudinal ones). The grain nucleation will result in recrystallisation and deteriorations of the mechanical properties and thus could initiate undesirable modifications of the material response.

The performance of T samples dropped due to the increase of the base temperature, which was reflected in the shift of the damage threshold. Here, crack and crack network formation started already at 0.38 GW/m² under any loading scenario, as it can be ssen in figure 4.13.

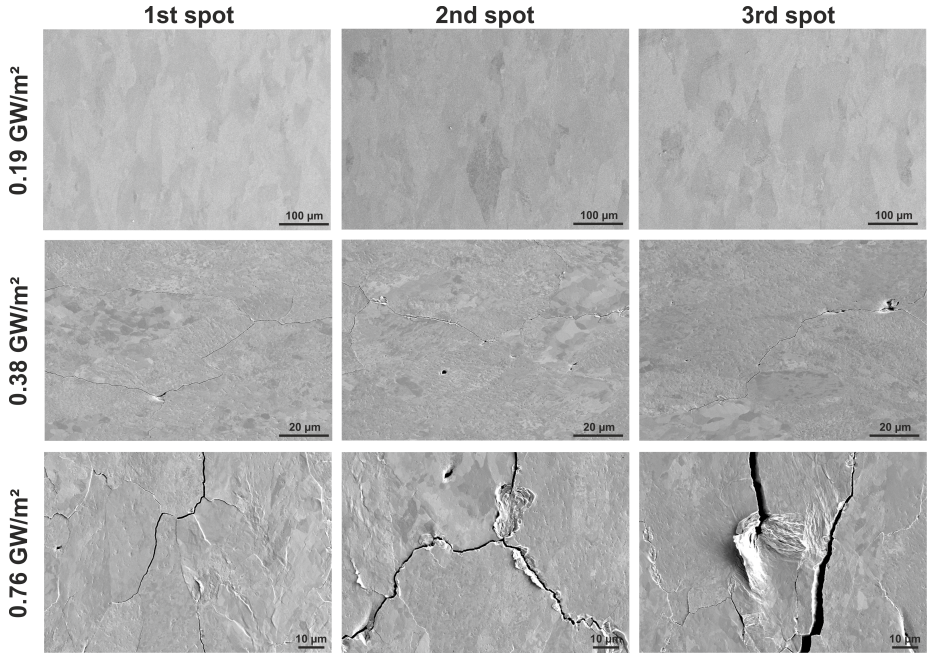


Figure 4.13: SEM images of T samples after sequential and simultaneous experiments at different absorbed power densities. Here, the crack evolution in dependence on the power density becomes evident.

This result evidenced the independence of the thermal shock behaviour from the loading order as well as the significant effect of the microstructure. Considering that a higher base temperature should increase the ductility in a way that stresses are relieved by plastic deformation, the brittle response of T samples indicated that this expectation was not met. The outcome is critical, since the transversal grain orientation is the preferential orientation for applications in ITER. Therefore, the consequences such as enhanced erosion, melting, and material losses would prejudicially affect the life time of in-vessel components and finally the operation of the

device. Moreover, roughness measurements only showed a slight increase of the R_a values in dependence on the applied power density. However, the cracks, which can be considered as artificial castellation, were appropriate to relieve stresses. This stress relaxation resulted on the one hand in less plastic deformation with low surface roughness values (table A.4 in appendix A.2) and on the other hand in increasing crack width values as a function of the power density. The associated average crack width values are listed in table A.5 in appendix A.2.

Metallographic cross sections disclosed that the cracks, generated at 0.38 GW/m², had an exceedingly shallow penetration depth. Owing to this, the cracks could not be discovered on the cross sections. The crack depth values after experiments at 0.76 GW/m² revealed the deepest penetration after initial plasma exposure followed by 100 transient thermal events. The cracks penetrated along grain boundaries perpendicular to the surface up to $\sim$ 220 µm deep into the bulk material. To complete, these experiments did not lead to detectable blister formation but the embrittling effect of deuterium was again determined, displayed in a denser crack network and deeper crack propagation.

The impact of the base temperature rise on R samples became apparent by the absence of cracks. The gain in ductility balanced the weaker mechanical properties due to the recrystallised microstructure. However, a power density dependent increase of the surface roughness was observed, which was accompanied by a decreasing amount of pores and cavities. Accordingly, most were found after tests at 0.19 GW/m², whereas power densities above 0.19 GW/m² lowered the amount significantly. An explanation for the decreasing pore/cavitiy formation could be that potential pores/cavities were covered by the rising plastic deformation of the loaded surface. In addition, the loading order evoked no effect on the thermal shock and/or damage behaviour. All measured data are listed in table A.4 in the appendix A.2 and figure 4.14 depicts SEM images of the surface evolution after experiments at different power densities.

In general, pores and cavities were least developed on R samples. The same was observed for experiments at 400 °C concerning blister formation. A reason for the reduced blister formation was the recrystallised microstructure itself because recrystallisation eliminates not only dislocations but also vacancies and/or vacancy clusters [90]. This in turn degrades the trapping sites for hydrogen and, therefore, less blisters were observed after tests at 400 °C and less pores and cavities were monitored after tests at 730 °C. Additionally, metallographic cross section (figure A.2 appendix A.2) showed again pronounced grain nucleation that also influenced the microstructure essentially. Cross sections of samples exposed to 0.76 GW/m² exhibited horizontal cracks in a depth of $\sim$ 28 µm underneath the loaded area. These kind of cracks are particularly risky due to the emergance of thermal barriers that

could promote melting and material loss.

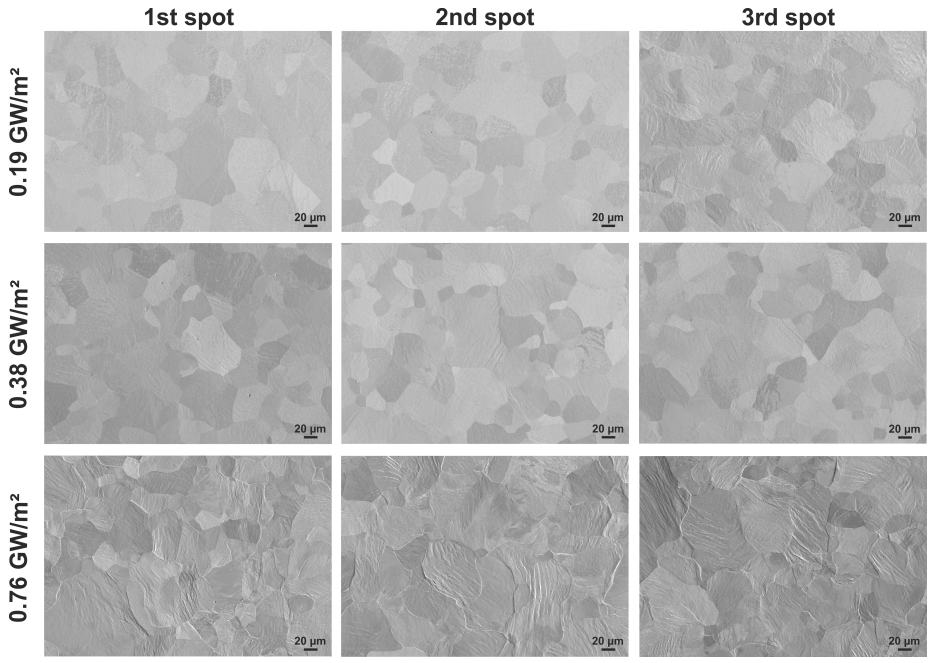


Figure 4.14: SEM images of the different exposure spots of R samples after tests at varying power densities. The connection between applied power density and surface roughness is clearly indicated, whereas a relation to the loading order was not observed.

The analysis of the damage evolution due to the increase from 100 to 1000 laser pulses exhibited no significant changes. Samples with longitudinal grain orientation and recrystallised microstructure showed almost the same thermal shock and damage behaviour and as stated in the previous paragraph, enhanced grain nucleation. Nonetheless, the grain nucleation did not influence the material performance. However, SEM images revealed that the surface roughness increased considerably due to the higher number of compressive and tensile stress cycles that had to be compensated. This observation was confirmed by R_a values, table A.4 in appendix A.2, which exhibited for both sample types a roughness increase by a factor of 4 - 5. Nevertheless, all stresses were solely counterbalanced by plastic deformation in opposition to T samples. Figure 4.15 illustrates the comparison of the surface modifications and/or damages after 100 and 1000 transient thermal events and figure B.4 - B.6 in appendix B.2 shows the corresponding SEM images.

T samples generated cracks instead of small cracks after tests at 0.38 GW/m². This

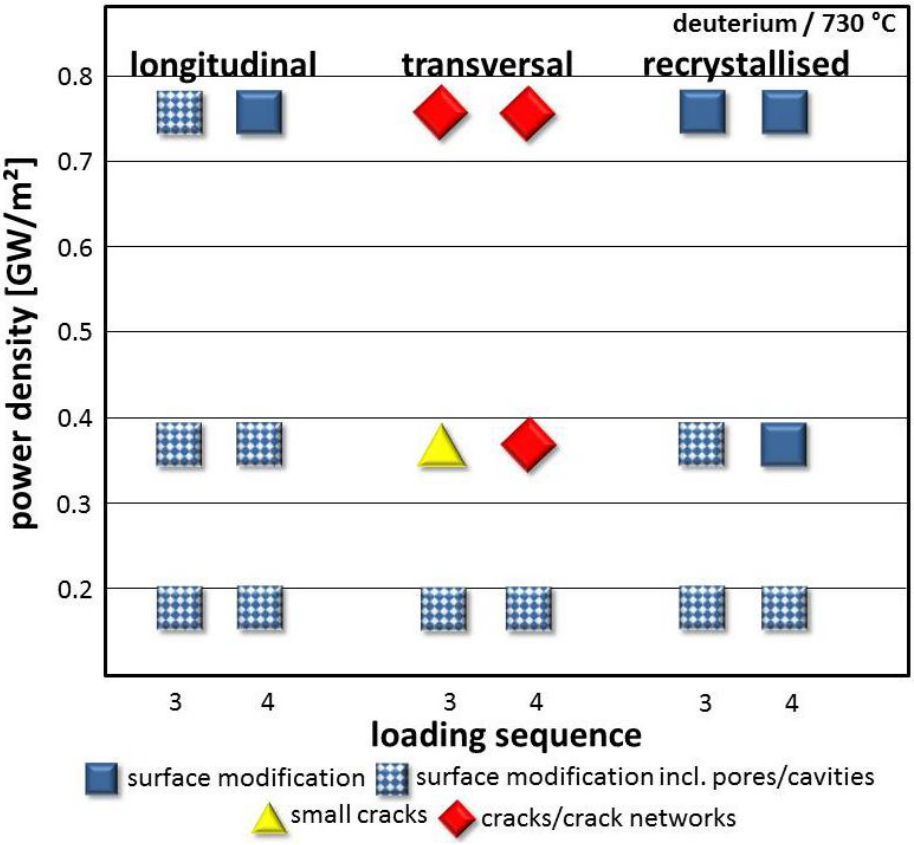


Figure 4.15: The mapping displays the damage evolution. Sequences with the same loading order, namely plasma with subsequent laser exposure, but varying pulse numbers (100 and 1000) were compared.

implied higher values of crack width and crack depth. To be more precise, after 100 laser pulses the highest crack width was 0.17 µm, while 1000 pulses initiated cracks with a maximum width of 0.42 µm. Thereby, the cracks propagated perpendicular to the loaded area into the bulk material and stopped at a maximum depth of $\sim$ 20 µm (after 1000 pulses). In addition, several cavities were identified within the bulk material after 1000 thermal events at 0.76 GW/m². These cavities had dimensions of up to $\sim 15 \times 6$ µm² and resided in depths of 10 µm up to $\sim$ 58 µm beneath the surface. They could have been an effect of the cross section preparation or originated from accumulations of hydrogen that penetrated deeper into the material due to an enhanced mobility. Anyhow, cavities inside the material support not only hydrogen accumulation and retention that raises the pressure inside the lattice of tungsten but interrupt the heat conduction because they act as thermal barriers. Both, the

stresses and the thermal barriers would entail grave consequences and, undoubtedly, they would change the mechanical properties as well as the thermal shock behaviour of the material.

Comparison of deuterium tests

Sequential and simultaneous experiments at base temperatures of 400 °C and 730 °C with pure deuterium plasma demonstrated the significant influence of the loading order, absorbed power density, pulse number, and microstructure of the sample on the thermal shock performance. Experiments at 400 °C revealed that the order of exposure had a substantial impact on the surface morphology, which was reflected on blister formation. Here, sequences executed at 0.38 GW/m² that ended with plasma exposure evoked a considerable amount of blisters within the loaded area. In contrast, simultaneous loading and sequences that ended with transient thermal events at power densities above and below 0.38 GW/m² initiated less marked or no blisters. In contrast, experiments at 730 °C did not show any correlation between the loading order and surface modification. Neither the surface roughness was affected nor blisters occurred, which can be ascribed to the high base temperature. Also, the detected pores/cavities were not provoked by the exposure sequence but by the applied power density and the plasma exposure in general.

Furthermore, at 400 °C it was found that deuterium had an adverse impact on the damage behaviour and exacerbated the performance substantially. This exacerbation was reflected in crack emergence on T and R samples, which was not investigated for experiments in [61,62] that were executed without deuterium plasma. The results showed conspicuously the embrittlement due to hydrogen retention. Tests at 730 °C revealed that an increase of the base temperature was not sufficient to compensate the adverse impact of deuterium because again cracks and crack networks were observed. In conjunction with these observations, the influence of the microstructure was highlighted. T and R samples offered lower mechanical strength due to their microstructure. T samples are more brittle due to the grain orientation and R samples suffer from weak grain boundaries and a lower yield/tensile strength. In contrast, L samples were more resistant against crack formation, which was traced back to texture strengthening effects involving in higher mechanical strength.

Moreover, experiments at 730 °C caused significant grain nucleation up to several 10 µm deep independent of the loading sequence, power density, and pulse number. This grain nucleation will lead to a recrystallised microstructure and, therefore, degrade the mechanical properties of the material. Texture strengthening effects attributed to the as received microstructure, as it became apparent in case of L samples, would slowly disappear and already mechanically weak microstructures would degrade even more. In conclusion, even if a higher base temperature in-

creases the ductility of the material, as it was observed on R samples, it will impact the microstructure detrimentally. With regard to an application in a fusion device, this could have severe influences on a smooth operation and desired lifetime of the components.

In both experimental series, the surface roughness evolution was controlled on the one hand by the applied power density and on the other hand by the number of laser pulses. By rising the power density, the surface roughness increased. Reasons for the higher surface roughness were certainly the increasing tensile and compressive stresses within the loaded area and the reduced yield strength. The changes of the surface morphology were less distinctive if the particular sample type had a high fracture strain and yield strength because these parameters are specifying the level of plastic deformation before cracks occur. In addition, the grain structure and grain size influence the mechanical properties like ductility and strength and, therefore, the material response and roughness development as well. In detail, small, elongated grains, like in case of the L and T samples, cause a finer distribution of lattice orientations and lead to a higher strength in deformation direction (texture strengthening) and in general (fine-grain strengthening) [59]. Moreover, R samples exhibit undeformed or less deformed, larger grains, which leads to a lower yield strength [59]. This circumstance was monitored by the lower damage threshold at 400 °C in comparison with L and T samples. The same roughness evolution was noticed for experiments executed with 1000 laser pulses instead of 100. Again, the thermal fatigue damage due to repetitive loading was the main reason for increasing surface roughness. Nevertheless, it can neither be claimed nor be evidenced that an increase of the base temperature improved the material performance or compensated the adverse impact of deuterium.

4.3 Sequential and simultaneous experiments with deuterium helium (6 %) plasma

In further experiments, the impact of sequential and simultaneous thermal and particle loads at different base temperatures was investigated, while the composition of the used plasma was changed. These tests were executed with a mixed deuterium helium plasma to achieve more realistic conditions and to study the impact of deuterium and helium, which behave differently in metals, on the thermal shock behaviour as well as material performance in general.

4.3.1 Sequential and simultaneous tests at 400 °C

For the second series of experiments, 6 % of helium was added to the deuterium gas. Thereby, the first tests were executed at 400 °C base temperature with the

same order of loading (figure 4.2) and applied power densities (0.19 - 0.76 GW/m²) as described in subsection 4.2.1. Moreover, all other experimental conditions stayed unchanged to keep the different experiments comparable. Afterwards, the exposed samples were investigated by means of laser profilometry, light microscopy, SEM, and metallographic cross sections.

Results and discussion

The results showed some considerable differences of the thermal shock behaviour and damage performance primarily in dependence on the applied power density and the microstructure of the samples. The impact of the loading sequence was moderate. According to the previous section, the discussion will be started with sequences that were executed with 100 transient thermal events, before the comparison with higher pulse numbers will be elaborated.

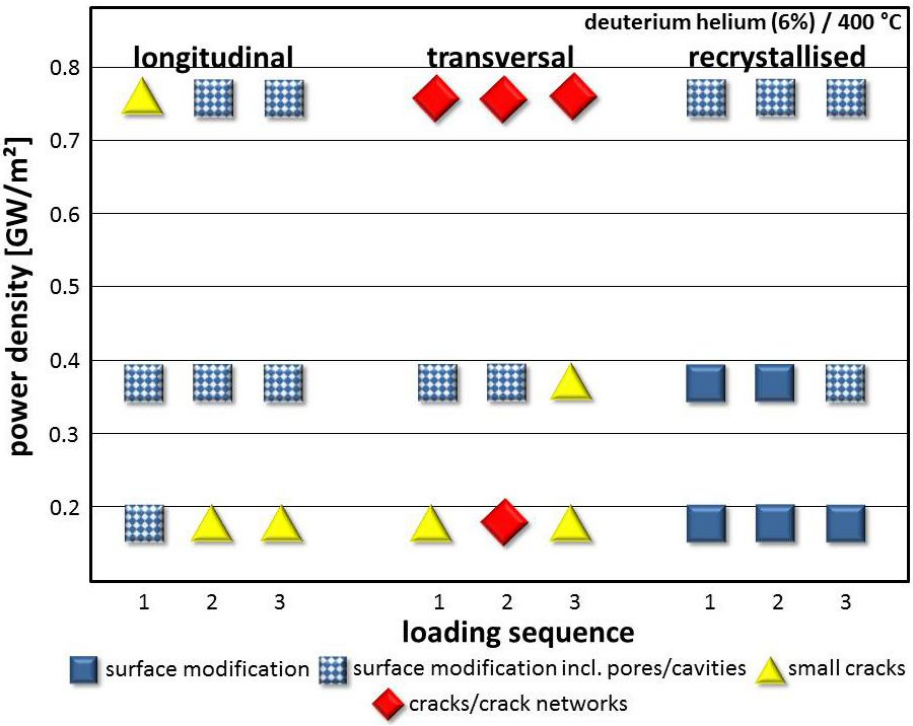


Figure 4.16: Damage mapping of the investigated surface modifications and damages in dependence on the loading sequence (100 laser pulses) and the absorbed power density. For all sample types, the damage threshold was located below 0.19 GW/m².

Starting with L samples, figure 4.16 shows a damage mapping that depicts all ob-

served surface modifications and damage types. First of all, it can be stated that the damage threshold was located below 0.19 GW/m². Furthermore, a correlation between the loading sequence and damage behaviour, valid for all three tested power densities, was not found.

However, for the lowest and highest tested power densities, a correlation between loading sequence and surface modification was detected. After simultaneous exposure and initial plasma load followed by laser beam loading at 0.19 GW/m², small cracks occurred that were only visible on SEM images due to the small crack width. The maximum average crack width was 0.16 µm and the cracks propagated up to $\sim$ 16 µm deep into the material, as cross sections pointed out. For tests at 0.76 GW/m² laser beam loads and subsequent plasma exposure generated small cracks with a wider maximum crack width of 0.51 µm but the same order of crack depth of $\sim$ 16 µm. All measured crack parameters can be found in table A.7 in appendix A.3, whereas figure 4.17 illustrates SEM images of the different loading spots at different power densities.

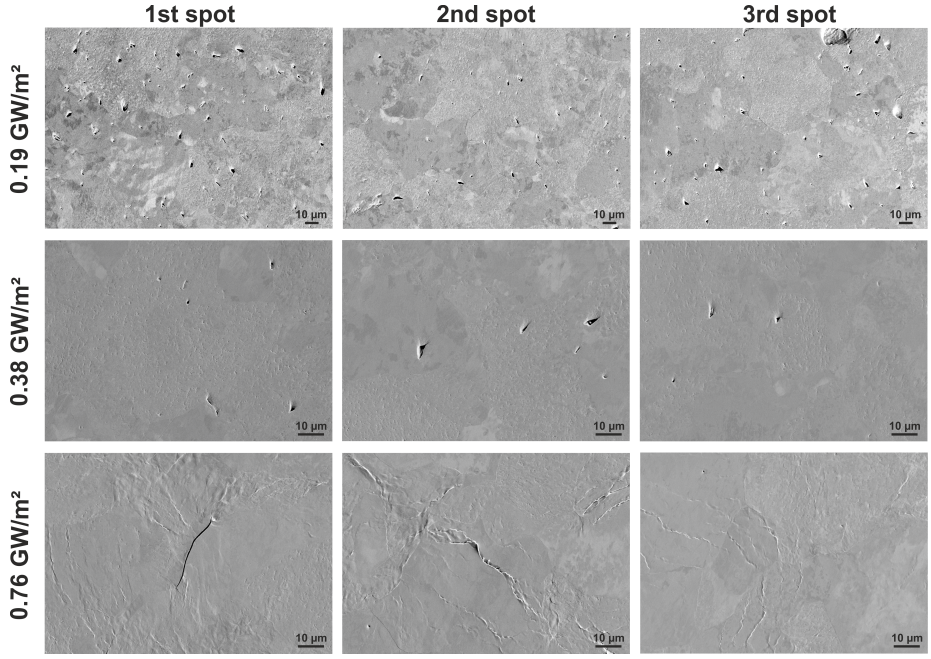


Figure 4.17: The picture illustrates SEM images of the different exposure spots of L samples. Thereby, the absorbed power density rises from the lowest 0.19 GW/m² in the first row up to the highest 0.76 GW/m² in the bottom row.

Furthermore, cavities and pores were ascertained within the loaded area for all test

conditions but no blisters. An explanation why no blisters were detected, could be the occupation of trapping sites by helium [91]. One reason for the occurrence of pores and cavities could be the loss of near-surface material due to accumulations of helium and/or deuterium, which induced local stresses by the formation of e.g. bubbles and, therefore, exceeded the yield strength of the material and led to material losses. Moreover, the decreasing amount of pores/cavities at rising power densities could be an effect of higher concentrations of trapped deuterium and/or helium in near-surface regions at low power densities. With rising power densities the mobility of the gas atoms increased due to the higher ΔT during thermal shock loads. Therefore, deuterium and/or helium penetrated deeper into the material or outgassed before pronounced accumulations could occur.

Additionally, the highest increase of plastic deformations, reflected in the measured R_a values (table A.6 appendix A.3), was detected after tests at the highest power density. Here, the high induced stresses exceeded the tensile strength of tungsten, which led to the formation of cracks after initial laser loading followed by plasma exposure, as already mentioned. Additionally, cracks horizontal to the loaded surface within the bulk material emerged on metallographic cross sections (see figure 4.18 a)). These horizontal cracks were observed up to a depth of 44 µm and they are inherently alarming because they act as thermal barries, which prevent the heat conduction and, therefore, promote overheating and melting. Moreover, the detection of such cracks during the operation of ITER will be almost impossible. Another observation was grain nucleation that will end up in recrystallisation, which should be prevented due to the deteriorating impact on the mechanical properties. The cross section images in figure 4.18 display examples of the aforementioned horizontal cracks and the microstructure after loading.

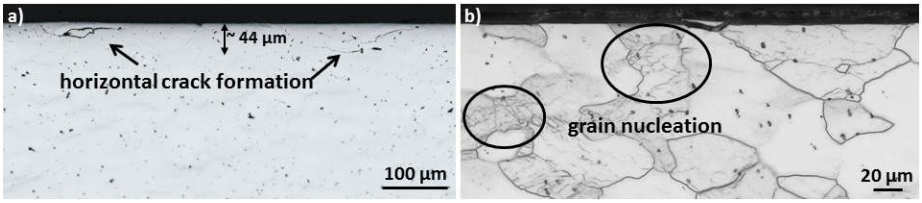


Figure 4.18: Image a) illustrates cracks inside the bulk material after tests at 0.76 GW/m² that spread horizontally to the loaded surface. Another result after experiments at 0.76 GW/m² was the grain nucleation that is highlighted in image b).

The influence of the microstructure became apparent on the damage behaviour of T samples. In line with L sample results, the damage threshold dropped below 0.19 GW/m². Furthermore, the induced stresses were only compensated by plastic

deformation for sequence one and two at 0.38 GW/m². All other loading conditions caused small cracks, large cracks, or crack networks. Thereby, tests at a power density of 0.76 GW/m² generated the worst damages independent of the exposure sequence. In general, T samples acted more brittle compared to L samples due to the missing texture strengthening effect reasoned by the grain orientation. The presence of deuterium and helium that accumulated in near-surface regions additionally embrittled the material and affected the performance negatively. Figure 4.19 illustrates exemplarily SEM images of the exposed surfaces at low and high power densities.

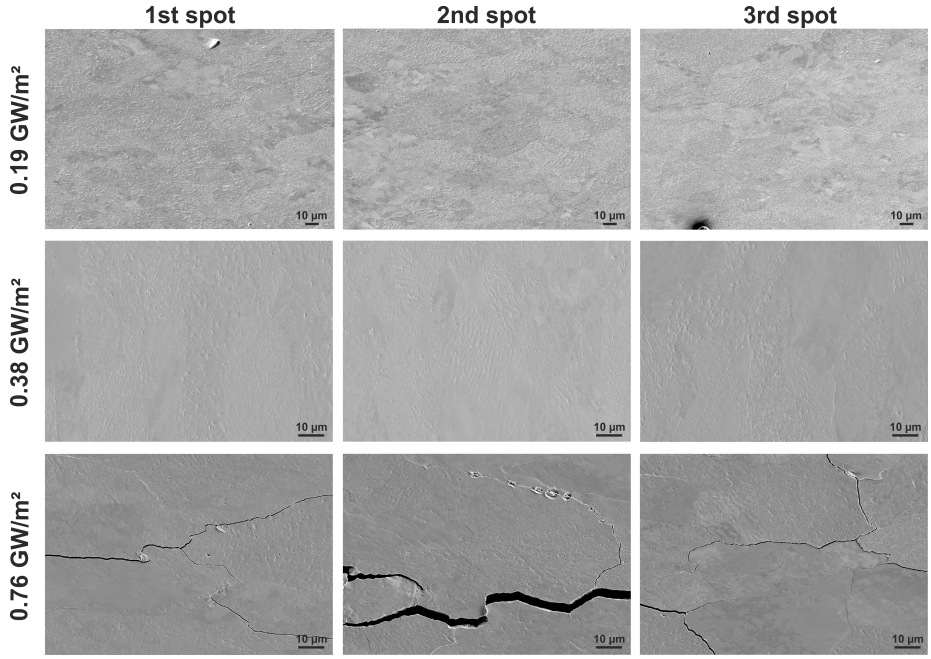


Figure 4.19: The figure shows SEM images of the different exposure spots of T samples. The top row depicts results after tests at 0.19 GW/m² and in the bottom row the results of experiments at the highest absorbed power density of 0.76 GW/m².

In accordance with the L samples results, pores and cavities occurred for almost each loading sequence and applied power density but no blister formation was detected. The pores/cavities were the result of a high amount of trapped deuterium and/or helium that evoked high stress levels within the material, which resulted in the loss of material. The absence of blisters was traced back to this loss of material and/or the presence of helium in the used plasma that reduced deuterium accumulations in the near-surface region by occupying trapping sites and, therefore, suppressing the

blister formation as it was stated in [91]. This highly temperature dependent effect starts at temperatures of $\sim\ 300 - 350$ K and is explained by He bubble formation in the near-surface region [91]. The interaction of helium with tungsten starts with the formation of vacancies/vacancy clusters along the path of the ions and leads to bubble formation. Moreover, the extent of helium induced damages (like He blistering and spongy surfaces) depends amongst others on the surface temperature and temperature gradients within the PFMs during the steady state and thermal shock loads [44].

Furthermore, metallographic cross sections revealed that the cracks propagated almost solely along the grain boundaries perpendicular to the loaded surface into the bulk material. Figure 4.20 shows metallographic cross section images after experiments at 0.76 GW/m². The deepest cracks were generated for all tested power densities after simultaneous exposure due to stresses induced by deuterium and/or helium accumulations simultaneously with stresses generated by the thermal transient events that exceeded the tensile strength of the material. Moreover, the thermal shock loads caused stresses but also defects within the tungsten lattice. Therefore, the amount of trapping sites for deuterium and/or helium increased and connected with it the amount of contained/trapped deuterium and/or helium in general [23]. Another explanation for the higher amount of contained/trapped deuterium and/or helium was found on higher diffusion rates of deuterium and helium, which were supported by the steep temperature gradients during each thermal shock event. Moreover, initial laser exposure followed by plasma loads and vice versa caused less deep cracks, but in the same order of magnitude for both sequences. This result was also valid for the crack width. Summarised, the results revealed not only that by increasing the power density, the crack depth and width increased but the simultaneous loading had a substantial impact on the propagation depth of the cracks. The arithmetic mean roughness values can be found in table A.6 in appendix A.3 and the crack parameter values in table A.8 in the same appendix.

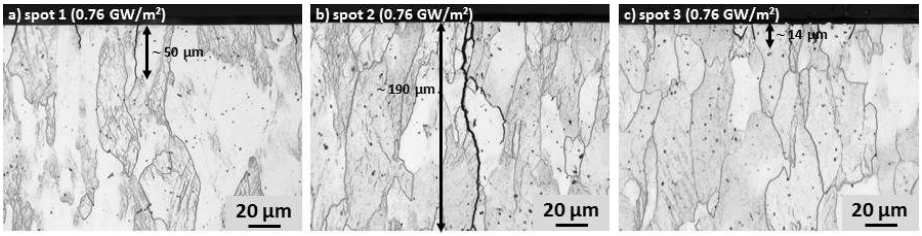


Figure 4.20: Cross section images of a T sample after different loading sequences at 0.76 GW/m². Image a) shows the microstructure after initial laser loads followed by plasma exposure, b) after simultaneous exposure, and c) after plasma load and subsequent laser loads.

The results exhibited that R samples performed best of the three tested samples types due to the absence of cracks. Here, the analysis of metallographic cross sections confirmed that no cracks were generated, neither shallow cracks in the near-surface region nor cracks inside the bulk material. Furthermore, all experiments solely caused surface modifications like roughening that increased with rising absorbed power densities and was independent of the loading sequence. Figure 4.21 depicts SEM images of the different exposure spots at all tested power densities.

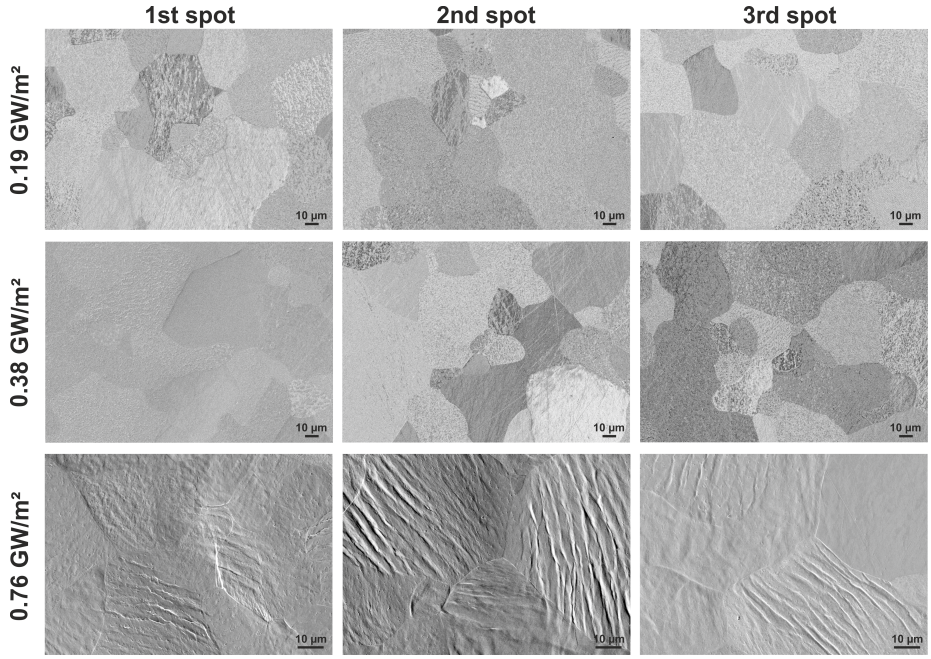


Figure 4.21: The figure illustrates SEM images of the different exposure spots of R samples. The top row shows the results after testing at the lowest power density and the highest power density is represented in the bottom row.

SEM images showed the highest plastic deformation for experiments at 0.76 GW/m² and, thereby, the highest extent of deformation was observed for certain orientations of the crystal lattice in a grain. Here, the crystal orientation seemed to have an impact on the stress compensation. Moreover, the loaded surfaces showed cavities and pores, whose amount increased with power densities above 0.19 GW/m². An explanation could be that power densities above 0.19 GW/m² led to higher ΔT values during the thermal shock loads and increased the mobility of deuterium/helium. Therefore, the amount of trapped deuterium and/or helium rose, which in turn could have caused an exceeding of the yield strength of the material and/or induced larger quantities of outgassing deuterium and/or helium, which then provoked the

loss of material. The surface roughness was measured by laser profilometry and the values can be found in table A.6 in appendix A.3.

The investigation of the damage evolution due to the increase of the number of laser pulses from 100 to 1000 exhibited no considerable changes with the exception of the formation and/or the amount of pores/cavities. For all three sample types, the thermal shock and damage behaviour stood nearly unaltered. Figure 4.22 depicts the comparison of the investigated damage types after 100 and 1000 laser pulses for all tested power densities.

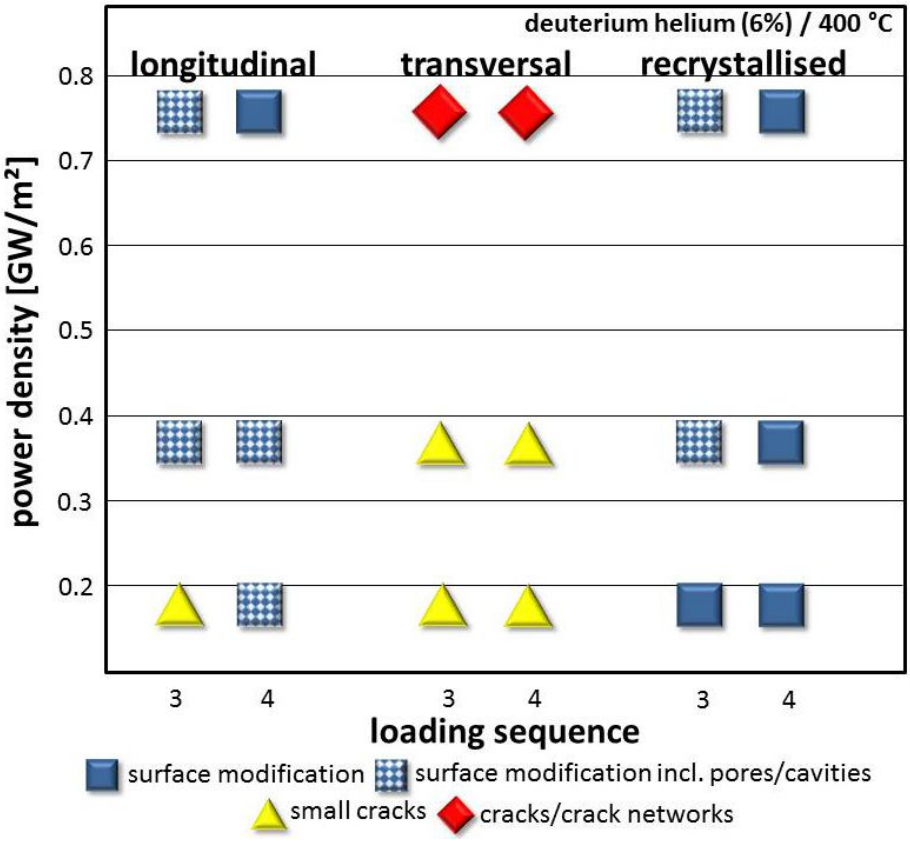


Figure 4.22: This damage mapping compares the damage evolution for all sample types after inital plasma exposure followed by 100 (3) or 1000 (4) laser pulses. The thermal shock and damage behaviour stood almost unaltered.

L samples showed no crack formation after 1000 transient thermal events, which could be an statistical effect or induced by parts of the machine (e.g. contamination of a window, which would have changed the absorptivity). After 1000 laser

pulses at 0.76 GW/m² no pores/cavities were observed, which also applied for R samples at 0.38 GW/m² and 0.76 GW/m². Explanations could be that the distinct surface roughness after 1000 thermal shock cycles covered the pores/cavities and/or the repetitive plastic deformation erased them. In contrast, T samples showed the weakest performance due to crack formation for all tested power densities. In addition, the analysis of SEM images revealed that the surface roughness increased due to the higher amount of compressive and tensile stress cycles that had to be compensated but also due to rising power densities. These results were confirmed by laser profilometry measurements that exhibited rising surface roughnesses for all sample types. Thereby, R samples showed the highest increase. Here, the roughness was up to five times higher as a function of the applied power density and pulse number, which was an indication for fatigue effects. The average R_a values can be found in table A.6 in appendix A.3. Furthermore, the figures B.7 - B.9 in appendix B.3 provide SEM images of the compared exposure sequences for all sample types and.

Moreover, the crack width and depth for T samples were compared. Both crack parameters increased by increasing the pulse number. For 0.19 GW/m² and 0.38 GW/m² the increase of the crack width was only marginal, but after 1000 laser pulses at 0.76 GW/m², the crack width was eight times higher than after 100 pulses. Comparing the crack depth revealed that by raising the number of applied laser pulses the cracks penetrated deeper into the material. Here, the largest difference in crack depth was observed after tests at 0.19 GW/m² because 1000 ELM-like events exhibited four times deeper cracks than 100 transient events. An explanation was a higher amount of trapped deuterium and/or helium in the near-surface region for experiments at 0.19 GW/m² and, therefore, higher stresses in the tungsten lattice. In contrast, at 0.76 GW/m² the ΔT per laser pulse was higher, which boosted the mobility of deuterium/helium significantly so that a larger amount of deuterium/helium outgassed in a short periode of time, which decreased not only the amount of trapped deuterium/helium but the stresses within the lattice. Another reason for the difference in the crack depth could be that at 0.76 GW/m² the crack depth already reached the limit determined by the temperature gradient and occured stresses, while this was not the case for lower power densities.

Last of all, metallographic cross sections revealed microstructural changes after 1000 laser pulses at 0.76 GW/m² in the near-surface region of L samples. Here, the material exhibited substructures within original grains and the start of recrystallisation down to a depth of $\sim$ 65 µm. Representative metallographic cross section images can be found in appendix A.3 figure A.3. Concerning the operation in a fusion device recrystallisation should be avoided due to the mechanical changes this microstructural transformation involves. But based on the presented results, where the recrystallised samples performed better than T samples and, therefore, recrystallisation could be

less disastrous as accepted.

4.3.2 Sequential and simultaneous tests at 730 °C

The next part of the sequential and simultaneous experiments with a mixed deuterium helium plasma was executed at 730 °C base temperature, while the rest of the loading conditions was maintained. The aim was to analyse the performance of tungsten at a base temperature that deteriorate the mechanical properties and where nano structures (so called tungsten fuzz) [92] start to be generated due to the helium content in the used plasma. These investigations were highly important because tungsten fuzz could tremendeously influence the thermal shock and damage behaviour and could additionally cause enhanced melting and erosion. For the experiments, the high temperature sample holder (figure A.1 appendix A.2) and an ohmic heater was used to achieve the required base temperature. Consistently, the discussion of the results starts with loading sequences that were executed with 100 laser pulses followed by the analysis of the damage evolution due to increasing pulse numbers.

Results and discussion

First, the results of L samples will be discussed. Figure 4.23 displays the worst observed surface modifications and damages for all tested sample types that emerged after sequential and simultaneous exposure at different absorbed power densities. The analysis ascertained that L samples generated small cracks for power densities above 0.19 GW/m². Thereby, experiments at 0.38 GW/m² caused small cracks for almost each loading sequence with the exception of simultaneous exposure. By rising the power density to 0.76 GW/m², only initial laser exposure followed by plasma loads and simultaneous exposure generated small cracks. In addition, the crack width increased with rising power densities, whereas the crack depth, which was investigated on metallographic cross sections, was in a similar range (table A.10 appendix A.4). Therefore, a correlation between loading sequence, applied power density, and thermal shock behaviour was observed and the damage threshold was located below 0.19 GW/m². Furthermore, the small cracks were accompanied by surface modifications like roughening, delaminations, molten parts, cavities/pores, and in addition, nano structures. These nano structures, or the start of the formation of nano structures were observed for almost all loading sequences and power densities except initial plasma exposure followed by laser loads at 0.76 GW/m². Thereby, the occurrence of these structures was traced back to the presence of helium in the used plasma due to the fact that helium, dependent on the base temperature and ion energy, leads to significant surface morphology modifications by near-surface implantations. In particular, for base temperatures $\geq\sim$ 730 °C and particle energies above 20 eV, tungsten nano structures with tendril-like features, tungsten fuzz, will

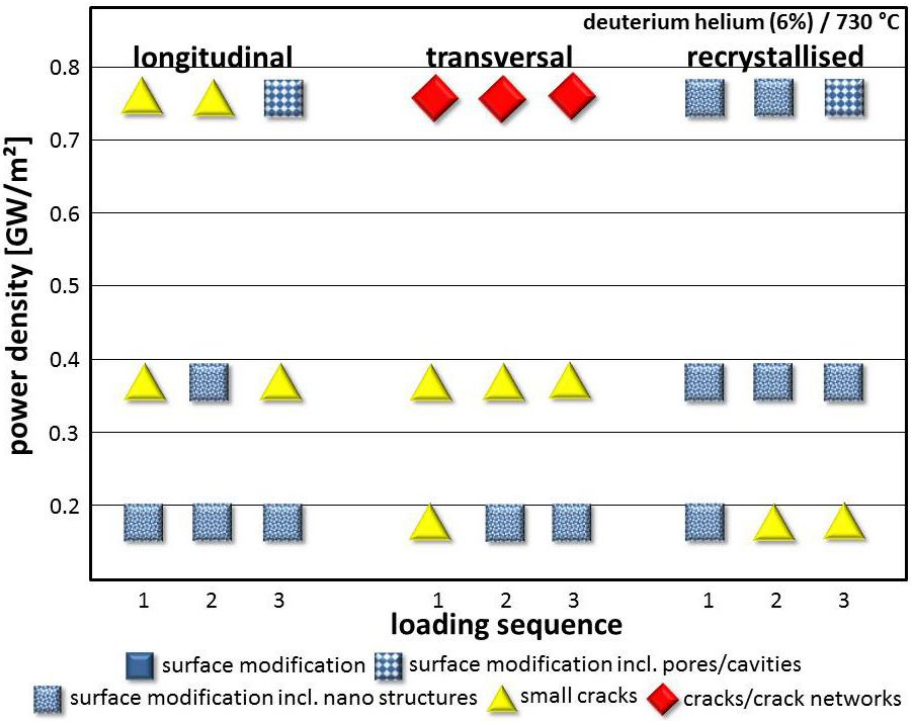


Figure 4.23: Mapping of the most severe observed surface modifications and damage types after loading sequences with 100 laser pulses in dependence on the loading sequence and absorbed power density. The damage threshold was detected below 0.19 GW/m² for all three sample types.

be formed [23, 92, 93].

The formation of tungsten fuzz starts with helium bubbles in the near-surface regions and when these bubbles grow, material is pushed out (viscoelastic flow) and fine filaments are formed [93]. It can be stated, based on SEM images with a high magnification, that the initiation of tungsten fuzz formation was observed and some of these SEM images are given in appendix B.4 figure B.10. In addition, a pronounced fuzz formation was not detected because this would require either a longer exposition time, a higher helium content, or a higher base temperature. Furthermore, a reason why fuzz was not observed after initial plasma exposure followed by laser loads at 0.76 GW/m² could be the high power density of the laser pulses and, therefore, high ΔT values during each laser pulse. If fine filaments had formed, the subsequent exposure to thermal shock loads destroyed the filaments by melting or erosion [92]. Figure 4.24 depicts SEM images of the loaded L sample surfaces.

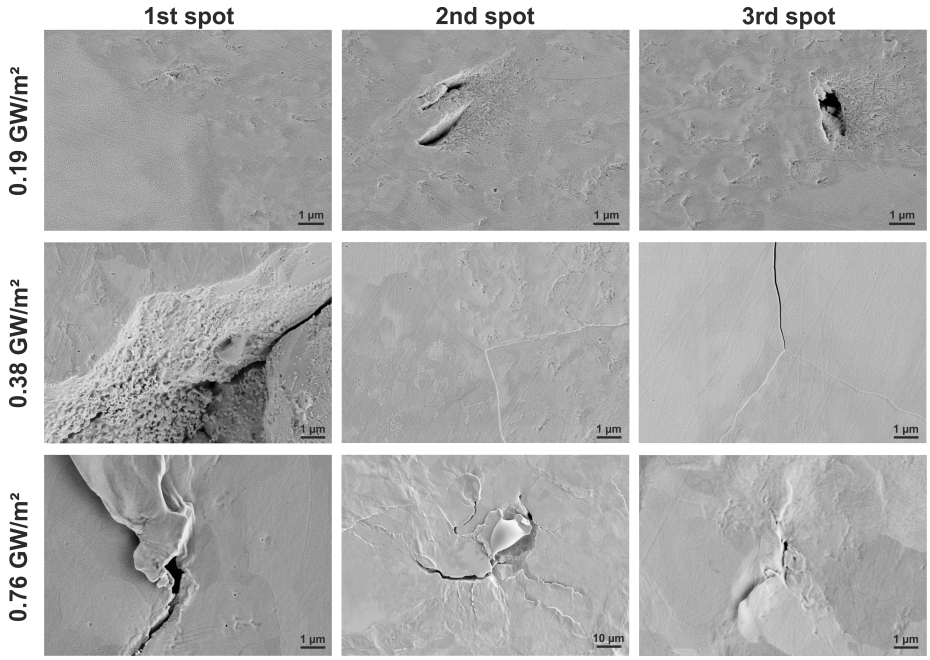


Figure 4.24: Representative SEM images of loaded L sample surfaces after different loading sequences and power densities. Here, power densities above 0.19 GW/m² caused small cracks and additionally the surface morphology change due to nano structures.

Moreover, helium/deuterium did not only modify the surface morphology but influenced the material performance significantly compared to pure deuterium tests. The texture strengthening effect and the resulting higher mechanical strength and ductility, which were observed in previous tests for longitudinal samples, dropped considerably. This drop was partly evoked by hydrogen embrittlement but for the most part generated by the helium irradiation. Due to the temperature dependence of hydrogen accumulation/retention, the amount of hydrogen in near-surface regions after experiments at 730 °C decreased continuously and the damage mechanisms are controled by helium [44]. This is the reason why blisters were not found. Furthermore, the highest surface roughness was detected after tests at 0.38 GW/m², whereas tests at 0.19 GW/m² and 0.76 GW/m² generated less roughening. The roughness values can be found in table A.9 in appendix A.4. Accompanied with the rising surface roughness, delaminations were observed, which led to overheating and the formation of melt droplets due to the poor thermal contact to the underlying material. In a fusion device, this could lead to erosion of material that would impurify the plasma.

The analysis of T samples exhibited that the damage threshold was located below 0.19 GW/m² and only simultaneous exposure and plasma loads followed by laser exposure at 0.19 GW/m² did not generate cracks (see figure 4.23). For all other loading conditions the tensile strength of the material was exceeded and caused cracking. Figure 4.25 illustrates SEM images of the different exposure spots in dependence on the applied power density.

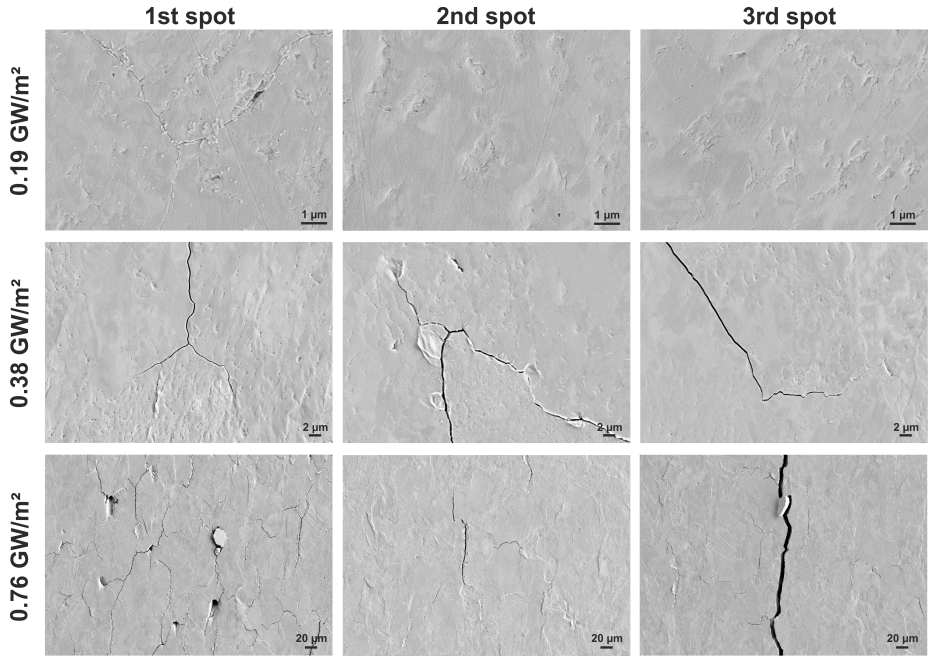


Figure 4.25: SEM images of the different exposure spots of T samples after experiments at different power densities. Tests at 0.76 GW/m² heavily impaired the material, which arose in the formation of crack networks, delaminations and molten parts.

In particular, below 0.76 GW/m² small cracks were observed, whereas tests at 0.76 GW/m² generated large cracks and crack networks within the loaded area. The crack width as well as the crack depth increased with rising power densities (see table A.11 in appendix A.4). Thereby, metallographic cross sections revealed that the cracks propagated always along the grain boundaries perpendicular to the loaded surface into the material. Additionally, the deepest cracks were observed after simultaneous exposure due to the simultaneous generation of stresses by repetitive thermal shock events and deuterium/helium accumulations within the tungsten lattice. Another damage parameter that increased with rising power densities was the surface roughness. The average values are given in table A.9 in appendix A.4.

Here, power densities above 0.19 GW/m² did not solely generate plastic deformation but caused isolated delaminations of material that in turn led to overheating and melting.

Furthermore, the temperature rise did not balance the brittle behaviour of T samples. Moreover, the material performance was additionally exacerabted due to the influence of deuterium and helium in near-surface regions. Predominantly, accumulations of helium in near-surface regions induced stresses within the lattice and affected the mechanical properties, the thermal conductivity, and the heat dissipation [92, 94]. All these effects, in addition to stresses arising from transient events and the presence of helium induced nano structures, had a significant impact on the thermal shock resistance. In addition, the combination of thermal and particle exposure and more precisely, the simultaneous or subsequent exposure of tungsten fuzz with transient events, changed the surface conditions tremendeously by the creation of a spongy surface morphology with a loose contact to the underlying material. The spongy morphology arose due to outgassing and/or melting of the filaments. Figure 4.26 depicts a metallographic cross section image of the path of a crack and SEM images of the spongy surface morphology.

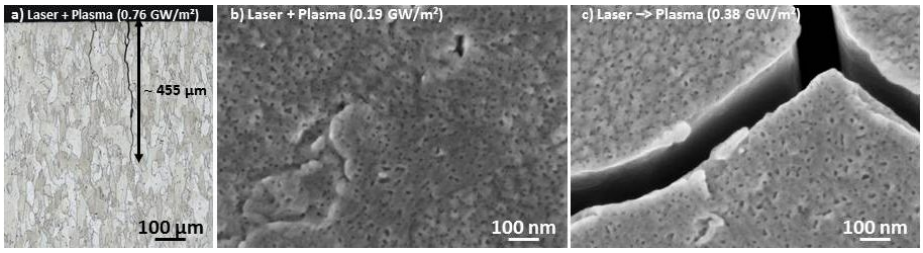


Figure 4.26: Image a) shows the crack propagation within a T sample after initial laser exposure followed by plasma loads at 0.76 GW/m². The spongy surface morphology is illustrated after b) simultaneous exposure at 0.19 GW/m² and on image c) after laser with subsequent plasma exposure at 0.38 GW/m².

The results of R samples revealed that recrystallised samples exhibited the best thermal shock behaviour. Again, the damage threshold was located below 0.19 GW/m² but the material compensated the induced stresses by plastic deformation except for simultaneous loads and plasma exposure followed by laser exposure at 0.19 GW/m². Profilometry measurements exhibited that the surface roughness increased with rising power densities (see table A.9 in appendix A.4) and additionally, simultaneous loads evoked the highest plastic deformation and, therefore, surface roughness. To underline this result, the analysis of the crack width and depth also indicated that after simultaneous exposure both parameters showed the highest values (see table A.12 in appendix A.4). Therefore, both findings were founded by concurrent stress

generation due to the implantation of helium/deuterium and the tension arising by thermal shock loads in comparison to successive stress generation. Figure 4.27 gives an overview of the different exposure spots at varying power densities.

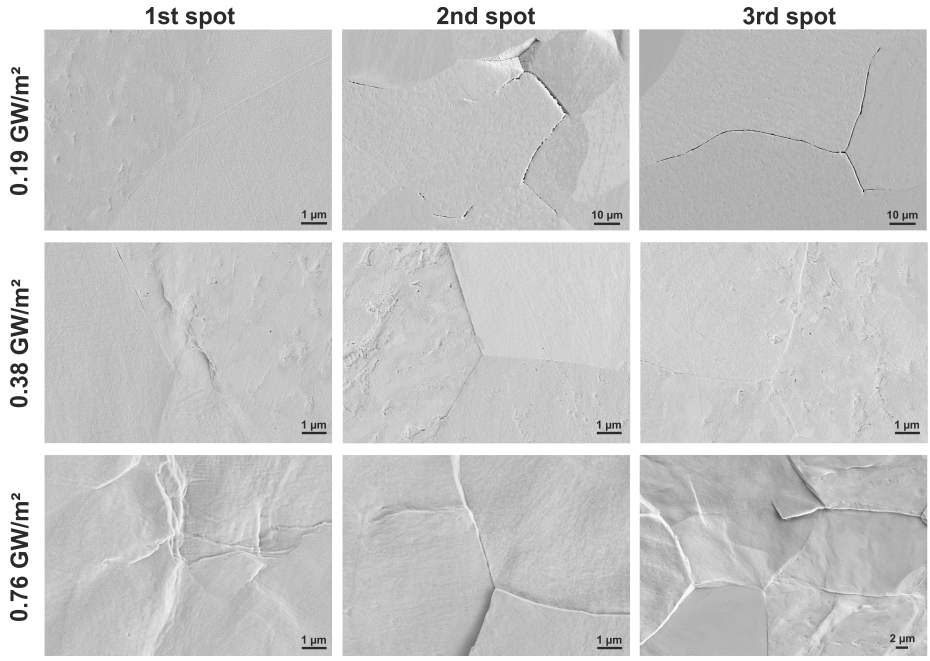


Figure 4.27: The figure depicts SEM images of R samples after simultaneous and subsequent loading at different power densities. Only simultaneous exposure and plasma loads followed by laser exposure at 0.19 GW/m² caused small cracks within the loaded area.

Furthermore, in agreement with the results of L and T samples, nano structures were found on the exposed R sample surfaces. As quoted before, due to the loading sequences and low quantity of helium in the plasma, no single filaments were detected but again a spongy structure. In detail, the loose contact to the underlying material as well as the reduced thermal conductivity/heat dissipation will promote overheating/melting during further thermal shock loads. Another observation that was made on cracked samples was the formation of tungsten fuzz inside the cracks (image a) figure 4.28) and crack bridging by tungsten fuzz (image b) figure 4.28). If this material would be further exposed to thermal shock loads, it will thermally expand and, thereby, the crack width will decrease or the small cracks could even close completely. This in turn would increase the risk of erosion and dust formation due to compressive forces or frictional loads on the nano structures inside the crack or between the crack edges, which suffer from a low mechanical stability. To complete,

besides the crack depth values the cross section analysis revealed that the cracks propagated along the grain boundaries perpendicular to the loaded surface into the bulk material. Moreover, a weak cohesion between single grains was displayed at the surface by the loss of whole grains during the preparation. With respect to an application in a fusion device, the lost material would impurify the plasma, which has to be avoided due to associated loss of plasma energy. Image c) in figure 4.28 displays the explained finding.

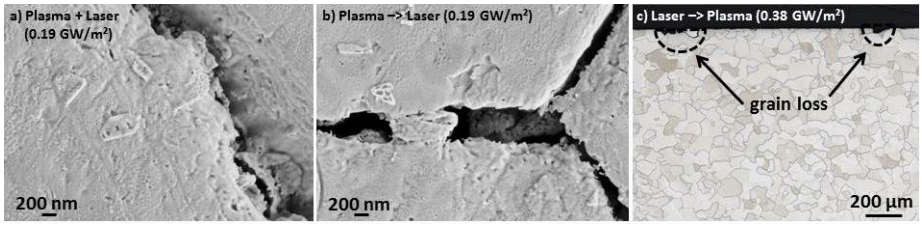


Figure 4.28: Image a) displays the fuzz formation inside a small crack after simultaneous exposure at 0.19 GW/m² of an R sample. After plasma exposure followed by laser loads crack bridging was observed that is illustrated on image b). Image c) shows the microstruture and grain loss after laser loads followed by plasma exposure at 0.38 GW/m².

In the following paragraph, the damage evolution due to the increase of the number of pulses will be discussed. First, it was observed that there were differences in the damage evolution after 1000 laser pulses. At T samples that were tested at 0.19 GW/m² small cracks emerged after 1000 laser pulses, whereas the same loading order with 100 laser pulses caused surface modifications only. Furthermore, R samples did not show pores/cavities after 1000 thermal stress cycles at power densities above 0.19 GW/m². The same was detected for L samples after tests at 0.76 GW/m². The high level of plastic deformation could be one reason why no pores/cavities were detected, another reason could be the repetitive expansion and contraction that annihilated the pores/cavities. Figure 4.29 depicts the most distinct results on the basis of a damage mapping and figures B.11 - B.13 in appendix B.4 compare the induced damages after 100 and 1000 transient events on the basis of SEM images.

Profilometry measurements indicated that the degradation state of the surface was affected by rising power densities and the increase of the applied pulse number. The repetitive heating and expansion followed by cooling-down and contraction of the material led to distinct irreversible plastic deformation. The mean roughness values are given in table A.9 in appendix A.4. Moreover, metallographic cross sections were prepared to investigate the microstructural evolution. All three sample types exhibited microstructural changes after 1000 transient thermal events in terms of re-

crystallisation. With a view to applications in future fusion devices, recrystallisation is considered as a serious issue due to the fact that it modifies the mechanical properties and the damage behaviour. Certainly, the presented results are contradictory to this statement because R samples performed best. Therefore, further experiments would be helpful to gain broader insights and to clarify how serious recrystallisation would be under operational conditions. Representative metallographic cross section images are provided in figure 4.30.

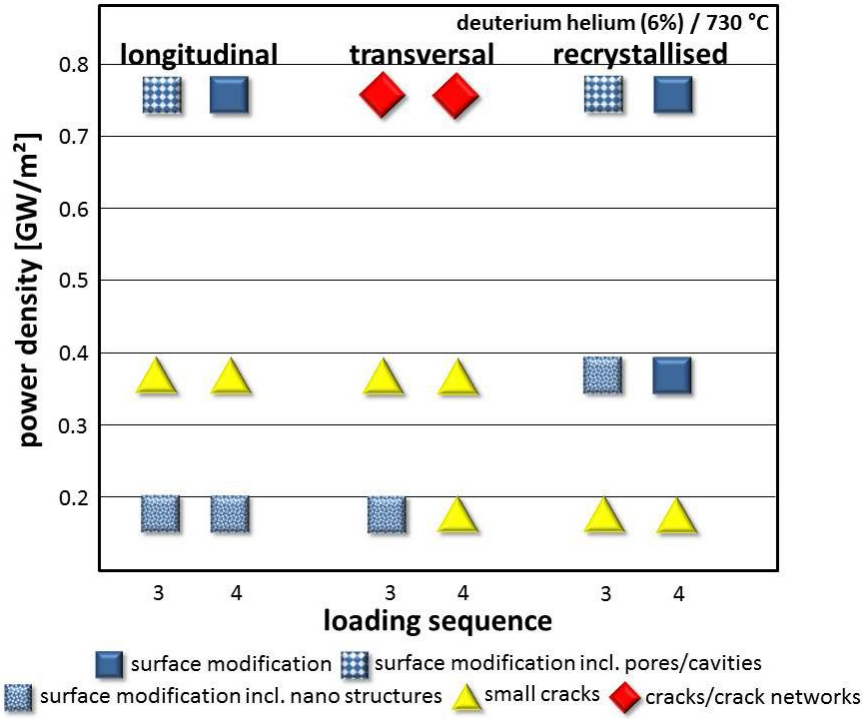


Figure 4.29: This damage mapping illustrates the damage evolution after 1000 laser pulses in comparison with the same loading sequence but 100 laser pulses in dependence on the applied power density.

Finally, none of the sample types showed nano structures after 1000 laser pulses at the highest tested power density. Here, the immense plastic deformation/surface roughness made it difficult to detect tungsten fuzz but detailed analysis confirmed that there were no nano structures or spongy morphology to find. Explanations for this result were on the one hand melting of the helium induced nano structures due to the high number of cyclic loads and on the other hand outgassing of helium in combination with a viscoelastic flow of the W fibres back to the surface.

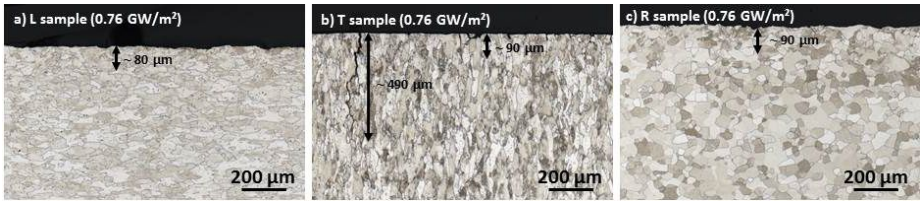


Figure 4.30: All cross sections are taken after initial plasma exposure followed by 1000 laser loads at 0.76 GW/m². Image a) shows the recrystallised zone of an L sample, image b) of a T sample and c) of an R sample. The thermally affected region is virtually identical for all sample types (typically 90 µm deep).

Comparison of deuterium helium plasma tests

The sequential and simultaneous experiments at different base temperatures (400 °C and 730 °C) with mixed deuterium helium plasma revealed that the loading sequence had virtually no effect on the damage and thermal shock behaviour. However, the absorbed power density, applied pulse number, and microstructure of the samples influenced the material performance considerably. Experiments at 400 °C exhibited that samples with longitudinal and transversal grain orientations generated small cracks, large cracks, and crack networks. Thereby, the performance of L samples dropped due to the exposure with deuterium/helium plasma in comparison to pure deuterium plasma. This drop was reflected in the emergence of small cracks after tests at 0.19 GW/m² and 0.76 GW/m². Transversal samples, which in general are more brittle due to the microstructure, exhibited small crack and cracks/crack networks. Here, the fracture strength was even more reduced by the presence of deuterium/helium. In contrast, R samples showed the best performance. The induced compressive and tensile stresses as well as stresses that arose from deuterium and/or helium concentrations in the near-surface region were solely compensated by plastic deformation. Moreover, by rising the base temperature to 730 °C, L samples showed small cracks for absorbed power densities above 0.19 GW/m², T samples slightly improved their performance at 0.19 GW/m² but at power densities above 0.19 GW/m² the damage behaviour became worse. In addition, the investigation of R samples revealed small cracks after experiments at 0.19 GW/m². These results can be traced back to the increase of the base temperature that in general reduces the yield strength and to helium/deuterium exposure that caused embrittlement.

Furthermore, the exposure with mixed deuterium helium plasma influenced the surface morphology. Here, no blisters were observed but cavities and pores were investigated, whose amount increased with rising power densities due to outgassing of trapped deuterium and/or helium. At 730 °C, helium dominated the surface modifications displayed by the formation of nano structures, namely tungsten fuzz. Tungsten fuzz significantly affected the surface morphology and performance of the

material. The loose contact of the nano structures to the underlying material led to melting and the formation of spongy surface morphologies, while helium concentrations in the near-surface region induced higher defect concentrations, lattice deformations, and stresses. Thereby, the thermal shock behaviour altered. Additionally, nano structures also emerged inside cracks and caused bridging of cracks. With regard to an application in a fusion device, these effects could lead to enhanced erosion, dust formation, and significant degradation of the components and their lifetime.

Both test series exhibited that the surface roughness evolution was significantly controlled by the absorbed power density and the number of applied laser pulses. With an increase of the absorbed power density, the compressive and tensile stresses increased, which had to be compensated. Sample types with high fracture strain and yield strength were able to compensate more just by plastic deformation. Additionally, the microstructure and resulting mechanical properties played an important role. Although, R samples had a lower yield and tensile strength compared to L and T samples, their performance appeared to be the best. To illustrate this statement, after 1000 laser pulses only surface roughening was observed in contrast to surface roughening inclusive pores and cavities after 100 pulses. Here, already at a low pulse number of 1000 (with regard to ITER and/or DEMO), the accumulation of damage/thermal fatigue damage due to the repetitive loading either covered the pores/cavities or erased them. In contrast, L samples, which benefit from the texture strengthening due to the microstructure, showed a weaker performance. The performance seemed to be improved only after 1000 transient thermal events at 0.76 GW/m², if the R_a values were disregarded. The distinction can be explained by the different influence of helium on the thermal shock behaviour of the varying sample types. Moreover, the degradation of the high yield/tensile strength of L samples, which was observed for tests with pure deuterium plasma, was conspicuous, whereas a deterioration of the already low yield/tensile strength of R samples did not have an appreciable effect. Furthermore, experiments with 1000 transient thermal events produced the highest roughness values due to the higher amount of compressive and tensile stress cycles, which was an indication of fatigue effects. Concluding, the addition of helium decreased the performance of longitudinal and transversal samples considerably.

4.4 Summary and conclusion

Experiments with simultaneous and sequential thermal and particle loads with varying plasma compositions, base temperatures, pulse numbers, and absorbed power densities were executed to investigate the thermal shock resistance and material performance as well as the impact of the test parameters and synergistic effects. Moreover, the influence of the microstructure and resultant differences of mechani-

cal properties on the damage behaviour were examined with regard to applications in future fusion devices. Furthermore, the stepwise approach to more realistic conditions, as they are expected in fusion devices like ITER, permitted a detailed study of the effects of each single test parameter but also of the effects of combined loading parameters. On the basis of these results, conclusions were drawn concerning the performance and lifetime of PFCs as well as proposals for the improvement of PFMs could be made.

Experiments with pure deuterium plasma at 400 °C revealed that no damage occured on L and T samples after tests at 0.19 GW/m². Therefore, the damage threshold was located between 0.19 and 0.38 GW/m². At absorbed power densities above 0.19 GW/m², both sample types showed surface modifications like roughening and blister formation. Nevertheless, the performance of T samples was worse, here small/large cracks and crack networks appeared. In general, the ductility of T and R samples at a base temperature of 400 °C was not sufficient to compensate induced stresses just by plastic deformation in contrast to L samples. T as well as R samples offered reduced mechanical properties, e.g. T samples acted rather brittle, due to their microstructure (grain orientation, grain size, weak grain boundaries etc.) in comparison to L samples, which benefit from texture strengthening effects. These properties in conjunction with a higher defect concentration and lattice deformation due to deuterium accumulations in the near-surface regions decreased the thermal shock performance and affected the damage behaviour compared to pure thermal shock experiments [61]. Here, the synergistic effect of microstructure related mechanical properties and hydrogen embrittlement became evident.

Furthermore, the loading sequence affected the surface morphology considerably. The loading sequence that ended with plasma exposure generated the highest amount of blisters within the loaded area as a function of the applied power density. More precise, after tests at 0.38 GW/m², most blisters were detected, whereas all other loading sequences and power densities caused less or no blisters. Blistering depends on the impinging ion energy, the ion fluence, the amount of trapping sites, and the temperature [44]. Therefore, loading sequences with initial thermal shock events promoted the formation, movement, and agglomeration of vacancies, in which deuterium was trapped and accumulated. In ITER and fusion devices beyond, supersaturation of deuterium could result in microcracking, cracks underneath the surface and erosion processes, which all will degrade the material performance.

The step to 1000 transient thermal events caused already measurable changes of the damage evolution. The higher amount of compressive and tensile stress cycles in combination with rising power densities provoked in dependence on the sample type distinct surface roughness, delaminations that resulted in molten areas, which solidified in scale-like structures, and thermal fatigue damage like small cracks and

crack networks. Here, T samples showed the weakest performance by the formation of crack networks, which is a profound result, since the transversal grain orientation is favored relating to applications in ITER. Moreover, in ITER the amount of transient thermal events will be considerably higher ($> 10^6$) than in the presented experiments and, thus, the conditions even more severe, which could lead to tremendous degradation and/or damage of the PFCs and a limitation of the lifetime.

Experiments at 400 °C but with a mixed deuterium helium plasma exhibited that the addition of 6% helium decimated the thermal shock performance and damage behaviour of L and T samples, whereas R samples showed an improved performance compared to the tests with pure deuterium plasma due to the fact that the induced stresses were solely compensated by plastic deformations. The improved performance of recrystallised samples is contradictory to the fact that recrystallised microstructures are weaker in general. Attempts to explain this result could be statistical fluctuations of the loading conditions, contaminated parts of the plasma generator etc., or less worsened mechanical properties due to the influence of helium. Further experiments are needed to achieve more certainty. The damage threshold decrease of L and T samples below 0.19 GW/m² indicated the diminution of the mechanical properties (like ductility, yield and tensile strength) and thermophysical properties by the presence of helium. This decrease was reflected in the formation of small cracks and cracks/crack networks already at 0.19 GW/m². As it was observed in earlier experiments [44,95], by using a helium seeded deuterium plasma, the damage formation was dominated by helium that reduced deuterium accumulations and deuterium retention due to the occupation of trapping sites at grain boundaries, vacancies, and dislocations, where bubbles started to form. The predominance of helium was observed in the absence of blisters and the occurrence of pores and cavities. The pores and cavities were the result of material loss due to accumulations of helium and/or deuterium in near-surface regions that caused an exceedance of the tensile strength of the material.

In coincidence with the results of pure deuterium tests, the increase of the pulse number did not impair the damage behaviour. Again, in dependence on the absorbed power density, the surface roughness and crack parameters increased. However, by comparing the mean surface roughness of both experiment series in general, the samples were less roughened after tests with mixed deuterium helium plasma. Explanations could be the lack of deuterium induced surface modifications (blister) due to the occupation of near-surface trapping sites by helium or the slight impact of helium on the surface morphology. Further experiments are required to understand the underlying mechanisms, which are responsible for the difference of the observed surface morphology evolutions.

In experiments with pure deuterium plasma at a base temperature of 730 °C, the

damage threshold for all sample types was located below 0.19 GW/m², which was mainly reasoned by the temperature rise that decreased the mechanical properties. In addition, the negative impact of hydrogen, namely hydrogen embrittlement, also acted opposing to the gain in ductility. While L and R samples compensated the induced stresses almost entirely by plastic deformation with the exception of a L sample that exhibited small cracks after initial laser exposure at 0.76 GW/m² followed by plasma loads, T samples generated cracks and crack networks nearly after each loading sequence above 0.19 GW/m². The results demonstrated the mechanical weakness of the transversal grain orientation, a high ductility of L and R samples, and that the loading sequence did not affect the damage behaviour.

Moreover, the elevated base temperature prevented blister formation due to the fact that blistering highly depends on the operating temperature (blister formation decreases at T > 950 K [44]). In exchange, pores and cavities were detected as a result of outgassing deuterium. The amount of pores/cavities was dependent on the applied power density, since the number of pores/cavities decreased with rising power densities. Furthermore, the increase of the absorbed power density and number of laser pulses caused a rise of the surface roughness but did not affect the damage category. Therefore, the highest surface roughness values were measured after sequences with 1000 laser pulses at 0.76 GW/m². Here, L samples exhibited the lowest surface roughness, which was traced back to the high fracture strain and yield strength, whereas R samples with a low yield strength showed significant surface roughening.

Finally, grain nucleation up to several 10 µm depth was observed independent of the loading order, power density, and pulse number. This thermally activated nucleation can lead to recrystallisation and grain growth. The driving forces are the prior deformation of the material, the temperature during the experiments, and the initial grain size. Furthermore, in fusion devices, recrystallisation must be avoided because recrystallisation increases the grain size, which in turn results in a higher DBTT and entails a lower mechanical strength and thermal shock fatigue resistance due to the reduction of dislocations and vacancies. Texture strengthening effects attributed to as received microstructures would disappear and already mechanically weak microstructures would degrade even more. The result would be enhanced cracking, erosion of complete grains, melting etc.

The tests at 730 °C with a mixed deuterium helium plasma revealed in coincidence with pure deuterium plasma tests at the same base temperature that the damage threshold was located below 0.19 GW/m². Again, T samples performed worst but also the damage behaviour of L and R samples deteriorated. This was attributed to both, the elevated base temperature that lowered the mechanical strength of the material and the presence of helium/deuterium that accumulated in near-surface

regions and, therefore, also influenced the properties of the material. In addition, the loading sequence had no effect on the damage behaviour. Here, the damage behaviour was mainly driven by the absorbed power density, pulse number, and microstructure of the samples. Precisely, T samples generated crack networks, whereas L and R samples only exhibited small cracks. The crack parameters as well as the surface roughness rose as a function of the applied power density. Here, T samples exhibited the lowest surface roughness, which was a result of the cracks that acted as stress-relief slots and, thereby, reduced the plastic deformation.

Furthermore, the formation of blisters was suppressed due to the high base temperature and the helium content. In addition to pores/cavities, the initiation of nano structures was observed on the exposed surfaces. These nano structures caused spongy surface morphologies, emerged inside cracks or bridged cracks, and altered the thermal shock resistance. If nano structures would form on PFCs, this would not only degrade the properties and lifetime but enormously increase the erosion and dust formation, if these structures would experience further thermal shock events. Moreover, the quantity of tungsten atoms within the plasma could exceed the tolerable amount and, therefore, degrade the plasma energy measurably. In the worst case, this would lead to a termination of the plasma. The raise of the number of applied transient thermal events in combination with increasing power densities did not affect the damage category but provoked distinct surface roughness and higher crack parameter values.

In summary, the simultaneous and sequential experiments at different base temperatures and varying plasma compositions exhibited that the damage behaviour of tungsten is highly complex and affected by many parameters. Moreover, interactions and connections between loading conditions, like base temperature and plasma composition, thermomechanical properties, and microstructure were identified and categorized. Thereby, the tests transpired that the favored transversal grain orientation for applications in ITER and devices beyond could lead to extensive problems. The results show that the reduced mechanical strength of T samples was further decreased by the presence of deuterium and helium as well as by the elevated base temperatures. Severe damage formation, namely roughening, formation of blisters, initiation of fuzz formation, cracks, and crack networks, were observed for almost each loading scenario. The most important result is that the highest tested power density (0.76 GW/m^2) always caused pronounced crack networks. Based on this and taking all expected loading conditions within a fusion device into account, premature failure of PFMs/PFCs could be one disastrous consequence amongst others. The decision if tungsten with a longitudinal grain orientation could be an appropriate alternative is elusive because the performance dropped by the presence of helium too. L samples showed a considerably better damage behaviour than T samples, but the risk of parallel crack formation is higher owing to the grain ori-

entation, which has to be prevented due to the risk of melting and erosion. In addition, recrystallisation was detected for both sample types, which will decrease the mechanical strength and increase the erosion of complete grains and, therefore, contaminate the plasma significantly. Solutions could be coatings, mechanical stabilisation by particle strengthening, or the reinforcement with e.g. tungsten fibers that could strengthen the material and suppress/guide crack propagation. However, the mitigation of ELMs and off-normal events as well as the prevention/limitation of off-normal events would also extend the lifetime of PFCs.

4.5 High pulse number experiments

Since ITER will start with a full-tungsten (W) divertor (originally, the start-up phase was foreseen with a low-Z divertor armoured with tiles made from fiber reinforced graphite), the thermal shock resistance of W became even more important due to the fact that high flux steady state plasma and transient ELM striking could limit the lifetime of PFMs. During the service time of the divertor in ITER, millions of unmitigated type-I ELMs with energy densities up to 10 MJm^{-2} are expected to strike the divertor as well as a steady state heat flux of around 10 MWm^{-2} (for slow transients even up to 20 MWm^{-2}) [16, 96]. The consequences of ELMs will be erosion, cracking, and melting, which in addition will increase the amount of impurities in the core plasma, as well as the destruction of PFCs. The steady state fluxes will change the surface morphology by blistering and helium-induced nano structures, which affect the material response. Therefore, the synergistic effect of high pulse number transient heat loads in conjunction with steady state deuterium helium (6 %) plasma was investigated.

In coincidence with the simultaneous and sequential experiments L, T, and R samples were examined. The tests were executed at a base temperature of 730 °C, which was achieved due to the plasma exposure and an ohmic heater at the sample holder. Moreover, to simulate the ELM-like transient thermal events, a Nd:YAG laser with a wavelength of 1064 nm was used. The impact of 10,000 and 100,000 transient thermal events with an absorbed power density of 0.38 GW/m^2, a pulse duration of 0.5 ms, and a repetition frequency of 10 Hz was investigated. The steady state exposure was realised by a mixed deuterium helium (6 %) plasma with a flux of $\sim 6 \times 10^{21}$ $m^{-2}s^{-1}$ and a fluence corresponding to 10,000 laser pulses and to the time to achieve the desired base temperature of up to $\sim 9 \times 10^{24}$ m^{-2} ($\sim 6 \times 10^{25}$ m^{-2} corresponding to 100,000 laser pulses plus the time to achieve the required base temperature). Furthermore, the particles were accelerated towards the samples via a bias voltage of - 60 V (resulting in a particle energy of $\sim$ 35 eV) and the variation of the base temperature during the entire exposure time was in the range of $15 - 20$ °C, therefore negligible. Afterwards, the induced damages and surface

modifications were analysed by means of laser profilometry, SEM, FIB, EBSD, and metallography. All measured R_a values as well as all other presented values (bubbles size etc.) can be found in appendix C.

4.5.1 Results and discussion

First, the results of an L sample that was exposed to 10,000 transient thermal events will be discussed. Figure 4.31 depicts SEM images of the exposure spot with varying magnification.

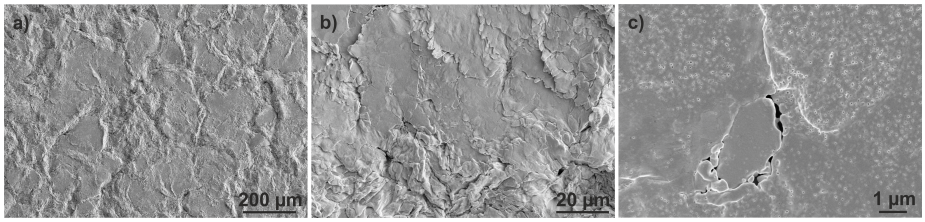


Figure 4.31: Loaded area of an L sample after 10,000 transient thermal events. The magnification increases from image a) to image c) and, thereby, the different surface modifications appear.

The loaded area showed pronounced plastic deformation due to the repetitive stresses induced by thermal shocks. Laser profilometry measurements exhibited an R_a value of ~ 2.34 µm. On SEM images with higher magnification (see image b) of figure 4.31) scale-like structures were observed, which were also detected after sequential experiments with 1000 laser pulses (see section 4.2.1). These scale-like structures were aligned within single grains, which indicated a conjunction with the crystallographic orientation of the grains. Furthermore, no blister formation was found due to the fact that helium dominated the damage mechanisms and suppressed the accumulations of deuterium in near-surface regions. Microcracks with a crack depth of ~ 15 µm generated within the loaded area and a spongy surface morphology was detected. The spongy surface was either the result of molten nano structures or of the loss of material due to partially bursted helium bubbles. In the case of nano structures, the repetitive heating during each laser pulse melted arising fuzz structures, which solidified after the transient event and created the spongy morphology. The other explanation could be that if the pressure inside the helium bubbles exceeded the tensile strength of the material, the bubbles burst and lost their caps. However, spongy surfaces obstruct the heat transmission and promote erosion, dust formation, and melting due to the loose structure.

Moreover, FIB cross sections revealed helium induced bubble formation below the surface. Images a) and b) in figure 4.32 illustrate FIB cross section images of the helium bubbles within the loaded area. The bubbles were located up to a depth of

140 nm underneath the exposed surface and had varying sizes. The largest bubbles had a major axis of 106 nm, whereas the major axis of the smallest bubbles was around 44 nm. A preferential location for the formation, e.g. within single grains or along grain boundaries, was not found. Moreover, these bubbles created distortions inside the lattice, which in turn caused stresses, prevented the heat transmission, and altered the mechanical properties of the material. In addition, metallographical cross sections were prepared to investigate the microstructure. Microstructural changes were detected up to a depth of $\sim$ 75 µm (images c) and d) in figure 4.32). Thereby, the near-surface regions experienced recrystallisation, whereas grain nucleation and subgrain formation dominated deeper regions. This difference was explained by the temperature gradient. Moreover, small cracks were observed that penetrated along the grain boundaries into the material up to a depth of $\sim$ 14 µm. At some locations, the cracks separated parts of the surface from the bulk material. Such separations can lead to overheating, melting, and material loss.

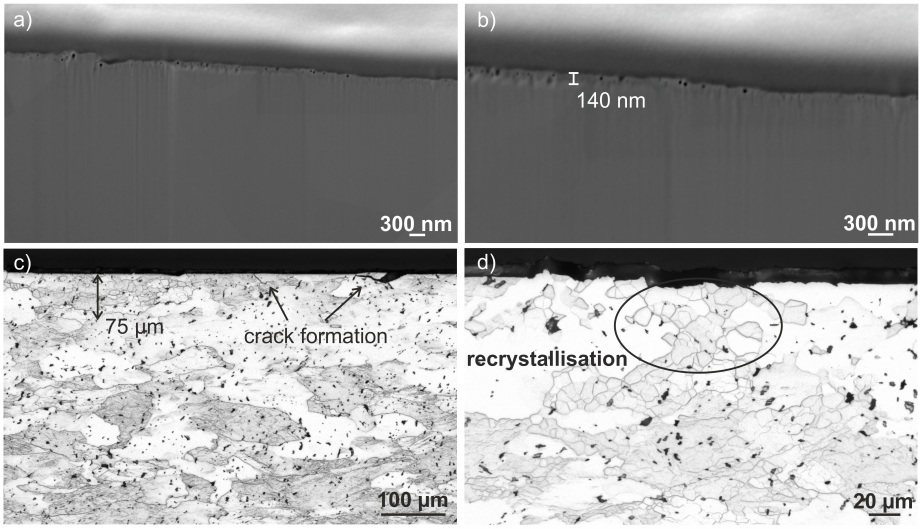


Figure 4.32: Images a) and b) show focussed ion beam cross section images of helium induced bubbles underneath the loaded surface of an L sample. The bubbles occurred in a layer with a depth of up to 140 nm. Images c) and d) show on the basis of metallographical cross sections crack formation and recrystallisation.

Furthermore, the pulse number was raised to 100,000, which also increased the deuterium/helium fluence. Figure 4.33 shows SEM images with different magnifications of an exposed L sample. In comparison with the L sample that experienced 10,000 laser pulses, the surface roughness increased considerably. Laser profilometry measurements confirmed this. After 10,000 stress cycles, an average R_a value of 2.34 µm

was measured, whereas after 100,000 stress cycles, the average R_a value was 36 µm. Moreover, the extreme plastic deformation generated distinct hills, which were separated by valleys. Additionally, a spongy surface morphology was detected but less pronounced than after loading with 10,000 laser pulses.

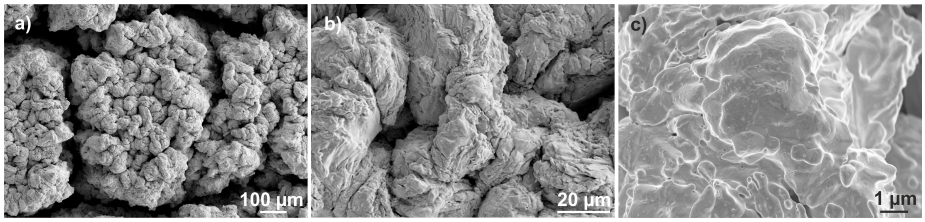


Figure 4.33: SEM images with varying magnifications of the surface of an L samples after exposure with 100,000 transient thermal events. The increase of the applied pulse number generated intense surface roughening and plastic deformation.

Based on metallographical cross sections, which can be seen in figure 4.34 images a) and b), the hill-valley structure was carefully analysed. Measurements revealed that the hills were up to $\sim$ 145 µm above the original surface and the valleys propagated down to a depth of $\sim$ 280 µm. In addition, a lot of cracks were detected within the hills, which were a result of thermal fatigue, the microstructural change, and accompanied by it, the decrease of the mechanical strength. In conformity with the test with 10,000 laser pulses, grain nucleation and recrystallisation took place. After 100,000 laser pulses, the microstructural changes were detected up to a depth of $\sim$ 480 µm, in contrast to $\sim$ 75 µm after 10,000 laser pulses. The recrystallisation in combination with the high base temperature, the temperature rise during the thermal shocks, and the influence of deuterium/helium resulted in a decrease of the thermal shock performance and caused pronounced plastic deformation and cracks.

Furthermore, the amount and size of helium bubbles within the loaded area and outside this area after 100,000 transient events was analysed via FIB cross sections. The FIB cross section images, which are shown in figure 4.34, revealed that within the exposed area and outside of the area bubbles were generated in a layer with similar depth. Inside the loaded area, the layer had a depth of 240 nm (4.34 c)), outside the exposure spot the depth of the layer was 210 nm (4.34 d)). Moreover, the size of helium induced bubbles were compared for both areas. The largest bubbles below the exposure spot (image c) figure 4.34) had a major axis of $\sim$ 110 nm and the smallest of $\sim$ 40 nm, within the only plasma exposed regions (image d) figure 4.34) the measured values of the major axis were $\sim$ 80 nm for the largest and $\sim$ 40 nm for the smallest bubbles. These results indicated that despite the surface temperature increase ($\Delta T \sim 750$ °C) during each thermal shock event, which increased the mobility of helium, the size of helium induced bubbles was more or less equal in

both regions.

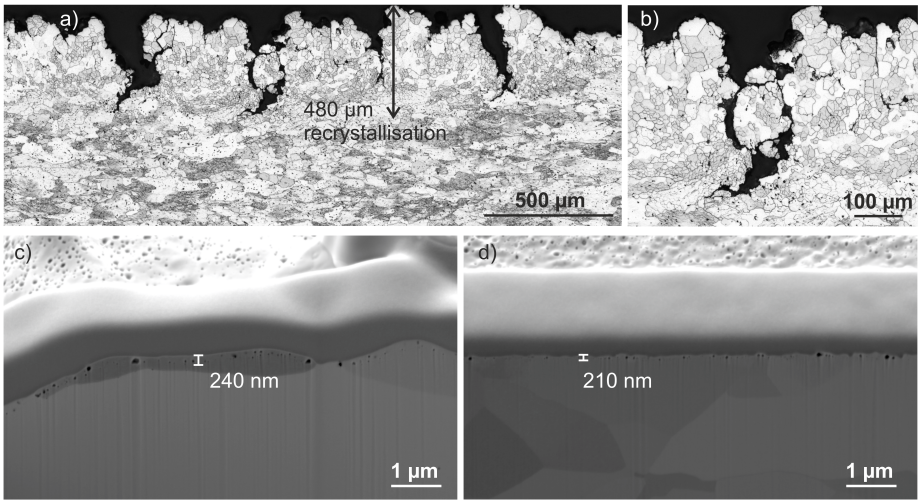


Figure 4.34: The metallographical cross section images a) and b) show the hill-valley structure as well as microstructural changes of an L samples after 100,000 transient events. Image c) illustrates the helium bubble formation within the simultaneously loaded area, whereas image d) shows the bubble formation in an area that was exposed to deuterium helium plasma only.

Furthermore, by comparing the bubble concentration below the exposed area after 100,000 ELM-like events and after 10,000 a difference based on the higher fluence was detected. The higher fluence in the case of 100,000 laser pulses increased the amount of helium bubbles. Moreover, the layer, in which helium bubbles were generated, was deeper after 100,000 and the spongy morphology was less pronounced after 100,000 than after 10,000 laser pulses. An explanation could be that the pressure inside the bubbles was lower due to the higher amount of bubbles, which then would have also influenced the loss of material (bubble caps). In addition, the high grade of plastic deformation could have impeded the detection of spongy structures. Therefore, it can be stated that the number of applied transient thermal events and the prolonged exposure time (higher fluence) affected the depth, in which helium bubbles were generated as well as the amount of trapped/outgassed helium. In addition, by comparing both tests it can be concluded that the raise of the number of pulses increased the surface modifications and damages and, therefore, melt and dust formation can not be excluded at these loading conditions and beyond.

The simultaneous exposure of a T sample with 10,000 transient thermal events and deuterium helium plasma exhibited a rough and cracked surface without blisters, which can be seen in figure 4.35. In comparison with the L sample that experienced

the same loading conditions (see figure 4.31), the surface appeared less rough. This impression was certified by laser profilometry measurements that exhibited a R_a value of 1.37 µm. Moreover, the generated cracks had an avergage crack width of 1.7 µm and acted as natural castellation and stress relief, which provoked that the surface experienced less plastic deformation. Furthermore, the occurrence of cracks indicated the substantial influence of the microstructure on the thermal shock and damage behaviour. The mechanical weakness of the transversal grain orientation was additionally degraded by the high base temperature and the presence of deuterium/helium that lowered the yield strength.

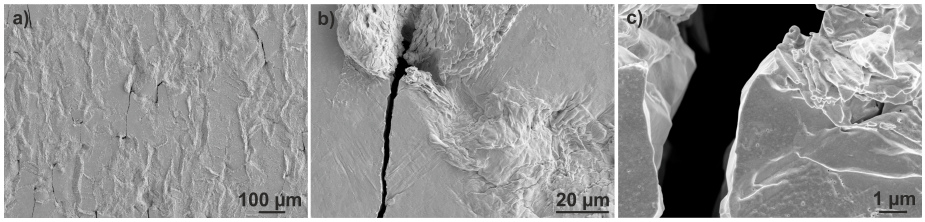


Figure 4.35: The SEM images of a T sample show that 10,000 laser pulses in combination with deuterium helium plasma caused surface roughening and crack formation within the loaded area.

To investigate the crack propagation and crack parameters, metallographical cross sections were prepared (image a) figure 4.36). The metallographical cross sections exhibited that most of the small cracks, which were observed on SEM images, were shallow and could not be detected on the cross section images. Nevertheless, at some locations cracks with a depth of $\sim$ 5 µm were observed as well as crack formation within the material. Image a) in figure 4.36 illustrates a crack that was found in a depth of $\sim$ 54 µm. Such cracks are a serious problem due to the fact that they act as thermal barrier and promote overheating, melting, and loss of material.

Additionally, grain nucleation and recrystallisation up to a depth of $\sim$ 95 µm occurred, which also affected the mechanical properties by decreasing the yield strength and cohesion between single grains. Moreover, the initiation of helium induced nano structures as well as bubbles beneath the loaded surface were less pronounced in comparison with an L sample after the same exposure conditions. In detail, the surface did not reveal the distinct spongy morphology. FIB cross sections emphasized that the number and size of helium bubbles below the surface were smaller in comparison with the L sample. Here, a small amount of bubbles with a major axis of 30 nm were generated in a layer with a depth up to 50 nm. The result is illustrated in figure 4.36 b). A reason for less helium accumulations and, therefore, less/smaller bubbles could be the generated cracks that relieved not only induced stresses but also trapped helium. In addition, the microstructure also could have been a cause for the pronounced difference due to a higher number of grain boundaries at the

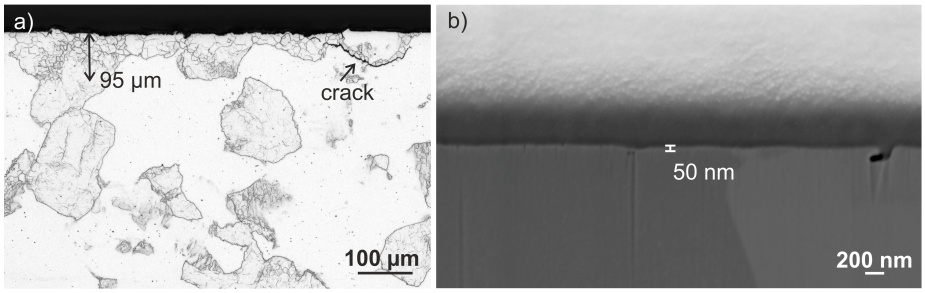


Figure 4.36: The metallographical cross section image a) illustrates the microstructural changes and the crack formation within a T sample after 10,000 laser pulses. The FIB cross section image b) depicts the low amount of helium induced bubbles.

surface and, therefore, a faster diffusion along these grains boundaries into deeper regions of the material. In conclusion, further experiments would be helpful, to identify the driving mechanisms.

After 100,000 laser pulses, the T sample surface showed distinct plastic deformation and crack formation at the edges of the exposed area due to the high stresses and the cooler surrounding material (see figure 4.37). The arithmetic mean roughness increased markedly (R_a = 22 µm in comparison to 1.37 µm after 10,000) but was less than the roughness of the L sample (R_a = 36 µm), which experienced the same loading conditions. The cracks at the edges of the exposed area, which acted as natural castellation and stress relief, seemed to be an explanation for this difference.

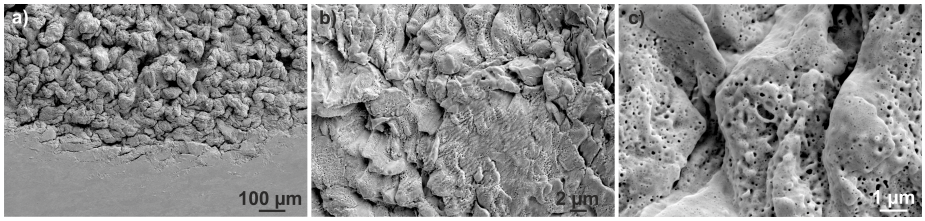


Figure 4.37: The SEM images illustrate the exposed surface of a T sample after 100,000 transient thermal events. Pronounced plastic deformation occurred due to the high number of repetitive stress cycles and a helium induced spongy morphology was detected.

In common with the L sample, the repetitive expansions and compressions produced a hill-valley surface morphology. Thereby, the hills were up to $\sim$ 87 µm above the original surface and the valleys stretched up to $\sim$ 193 µm deep into the material. Besides the plastic deformation of the loaded area, a pronounced spongy surface

morphology was observed. The distinct difference between the T sample that was exposed to 100,000 laser pulses and the T sample that experienced 10,000 laser pulses indicated that the amount of trapped helium increased. An explanation was found in the extent of the exposure time. Moreover, cavities originated within the hills, which were attributed to thermal fatigue damage due to the repetitive loading and/or the change of the microstructure, which affected the mechanical properties. Metallographical cross sections exhibited grain nucleation and recrystallisation of the near-surface region up to a depth of $\sim$ 340 µm (image a) and b) figure 4.38). The microstructural change caused agglomerations of vacancies, dislocations etc. at grain boundaries and, therefore, lowered the grain boundary strength, which provoked material loss during the cross section preparation as well as deteriorated the fatigue performance.

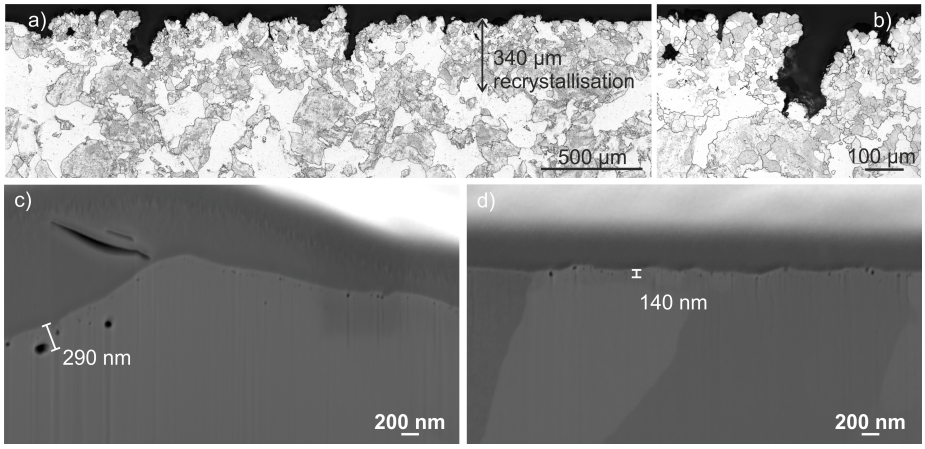


Figure 4.38: The metallographical cross section images a) and b) show the hill-valley surface morphology as well as the recrystallisation of the microstructure of a T sample after 100,000 ELM-like events. Image c) illustrates the helium bubble formation within the loaded area, whereas image d) depicts the bubbles below the only plasma exposed area.

Furthermore, the increase of the number of applied transient thermal events raised the dimensions of the layer, in which helium bubbles were generated. Based on FIB cross sections, the depth of the layer as well as the size of the helium bubbles within the loaded area and outside the loaded area were analysed and significant differences were observed, not only for both investigated regions but also in comparison to the test with 10,000 laser pulses. Figures 4.38 c) and d) illustrate the results. Within the exposure spot, the bubbles formed in a depth up to 290 nm underneath the loaded surface, while for the solely plasma exposed area the maximum depth, at which bubbles were detected, was 140 nm. Moreover, the size of the bubbles was

larger after 100,000 stress cycles than after 10,000. The largest bubbles below the simultaneous exposed area had a major axis of 170 nm and the smallest of 35 nm. The investigations of the pure plasma loaded regions revealed bubbles with major axes of 51 nm and 20 nm for the largest and smallest. This difference could be reasoned by the higher helium mobility within the simultaneous exposed area due to the temperature rise during each transient thermal event, which enhanced the amount of trapped helium. In comparison with the longitudinal sample (100,000 transient events), the number and size of the bubbles in both areas were in the same order of magnitude but slightly smaller for the T sample exposed to 100,000. This observation exhibited that after 100,000 stress cycles, the varying microstructures had less effect on helium induced damages. Nevertheless, the recrystallisation, spongy surface morphology, helium bubbles, as well as the heavily deformed surface alter the mechanical poperties, the thermal shock behaviour, and the fatigue performance tremendously and increase the risk of overheating, melting, erosion, and dust formation significantly, which have to be avoided or at least mitigated in future fusion devices.

A recrystallised sample that was exposed to 10,000 transient thermal events showed pronounced surface roughening accompanied by structures that looked like the initial phase of scale-like structures (image a) figure 4.39). Laser profilometry measurements revealed an R_a value of 4.16 µm, which was the highest in comparison of all tested samples at these loading conditions. An explanation could be the lower mechanical strength that led to higher plastic deformation. Moreover, neither blister formation nor cracks were observed. To investigate the microstructure, metallographical cross sections were prepared.



Figure 4.39: Representative SEM images of an R sample after simultaneous loading with deuterium helium plasma and 10,000 laser pulses. Besides pronounced surface roughening, distinct fuzz formation was detected.

Figure 4.40 a) depicts a metallographical cross section image that shows the change of the microstructure. After 10,000 transient thermal events, grain nucleation as well as recrystallisation was observed up to a depth of $\sim$ 100 µm. Further investigations were executed via electron backscatter diffraction (EBSD) analysis. The analysis of small angle grain boundaries (figure 4.41 d)) exhibited a more detailed result about

the depth of the microstructural changes and the kind of the changes. Thereby, up to a depth of ∼ 200 µm substructured grains and entirely recrystallised grains were found and additionally, the new recrystallised grains were considerably smaller (average major axis of ∼ 15 µm) as the original ones (average major axis ∼ 64 µm). The results are illustrated in figure 4.41.

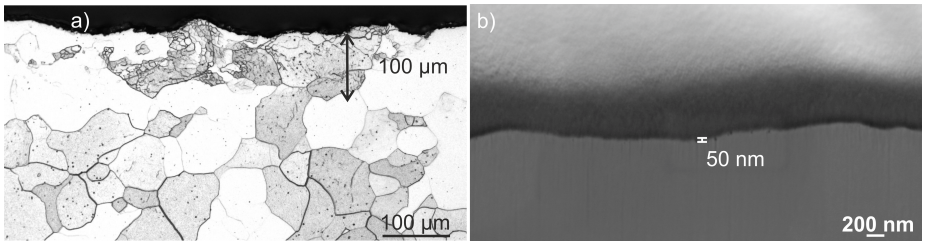


Figure 4.40: Image a) shows a metallographical cross section that depicts the microstructural change of the R sample after 10,000 ELM-like events. Image b) illustrates the helium bubble formation underneath the loaded surface.

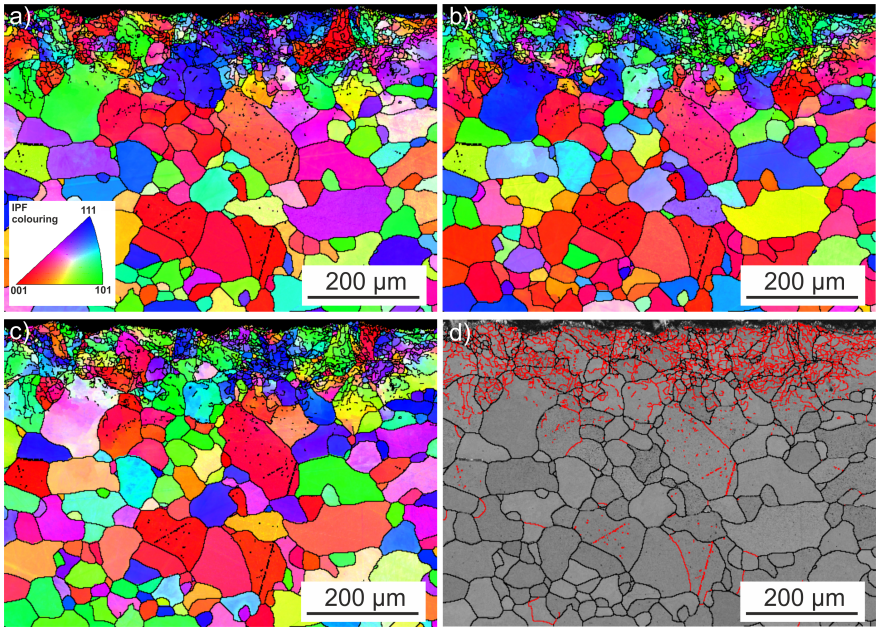


Figure 4.41: Images a) - c) illustrate the crystal orientation of subgrains and new recrystallised of an R sample. Thereby, images a) and c) depict the orientation of the crystal parallel to the loading direction and b) in loading direction. Image d) shows the amount of small angle grain boundaries (in red) and original grain boundaries (in black).

The inverse pole figure (IPF) colouring maps, which are shown in figure 4.41 a) - c), indicated the crystal orientation of subgrains and new recrystallised grains after exposure to 10,000 ELM-like events. Thereby, most of the new developed subgrains/recrystallised grains had the same crystal orientation ⟨101⟩ in loading direction. Furthermore, the investigation of the ratio of recrystallised grains, substructured grains, and deformed ones revealed that substructured grains dominated the affected region. The results can be seen in figure 4.42.

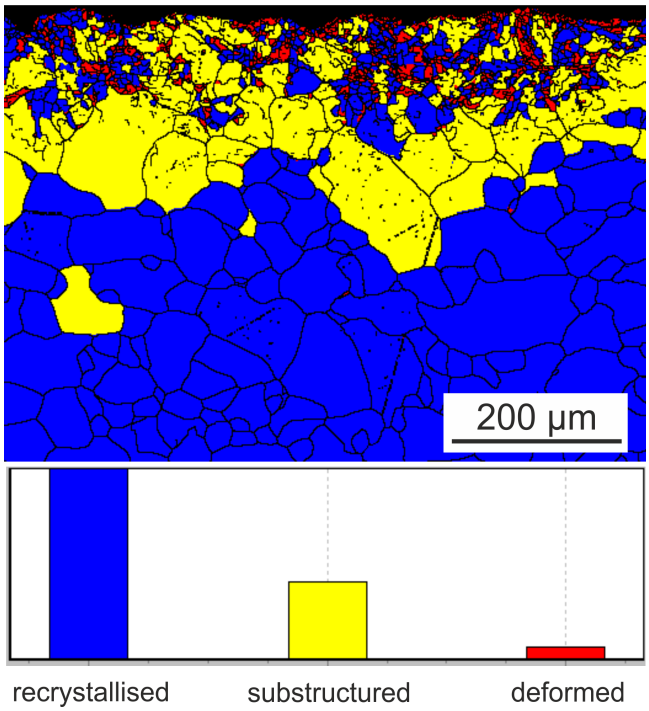


Figure 4.42: The image shows the ratio of recrystallised grains, substructured grains, and deformed ones of a R sample after 10,000 transient thermal events. The bottom of the image, depicts the original microstructure, whereas the top illustrates the near-surface region that was affected by ELM-like events and plasma exposure. The graph below exhibites the proportion of the different microstructural states.

Both, substructured grains and recrystallisation, affect the mechanical properties and the thermal shock resistance of the material. Additionally, the region, in which the microstructural change occurred, was the largest by comparing all tests with the same exposure conditions, which indicated again the influence of the microstructure. Furthermore, SEM images with a higher magnification exhibited distinct nano structures, which can be seen in figure 4.39 c). Here, the significant influence of

the microstructure became apparent again. In coincidence with L and T samples, a spongy morphology was detected but with a completely different characteristic. In contrast to the other sample types, the surface was not just flat with a high amount of holes. Here, fuzz tendrils had developed, which then were molten by the thermal shock events and possibly solidified in this spongy microstructure. For a profound investigation, FIB cross sections were prepared. The analysis revealed that only a small amount of bubbles was generated within a layer with a maximum depth of ~ 50 nm (figure 4.40 b)). The largest bubbles had a major axis of ~ 21 nm and the smallest of ~ 10 nm. Consequently, the amount as well as the size of the helium induced bubbles were the lowest of all tested samples. An explanation could be the lower defect concentration of recrystallised tungsten compared to L and T samples. Furthermore, due to the lower defect concentration and trapping sites higher amounts of helium could have accumulated in the existing ones. If this was the case, the bubbles grew faster, which in turn entailed a viscoelastic flow of tungsten and the formation of tungsten tendrils (fuzz). This would also explain, why less helium induced bubbles were observed in contrast to L and T samples. However, these experiments need to be expanded to obtain more detailed insights.

The experiment with 100,000 transient thermal events caused an increase of the surface roughness. Figure 4.43 depicts SEM images with varying magnification, which show the induced surface modifications.

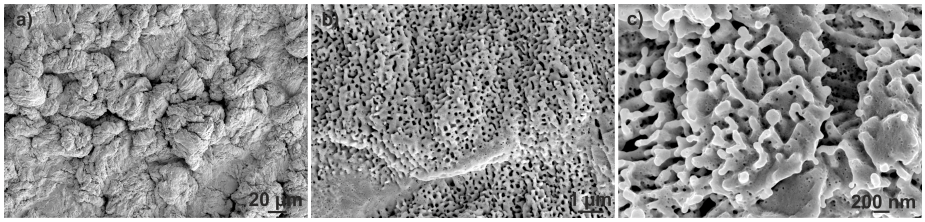


Figure 4.43: SEM images with different magnification of the exposed surface of an R sample after 100,000 ELM-like events. The repetitive stress cycles caused distinct plastic deformation and molten W tendrils.

First of all, the arithmetic mean roughness was measured. After 100,000 ELM-like events, the surface roughness increased to $R_a \sim 6$ µm, which was the lowest rise in comparison with the other sample types after the same exposure conditions. An explanation could be the higher ductility and the open volume between adjacent grains, which acted as space for expansion and stress relief and, therefore, the surface experienced less plastic deformation. Nevertheless, the high amount of compressive and tensile stress cycles generated a hill-valley surface morphology as it was observed after all experiments with 100,000 transient thermal events. Here, the largest hills were ~ 53 µm (L ~ 145 µm, T ~ 87 µm after 100,000 transient events) above the

original surface and the valleys expanded up to a depth of ∼ 24 µm (L ∼ 280 µm, T ∼ 193 µm after 100,000 transient events). This result endorsed the roughness measurements and evidenced a minor impact of the number of applied pulses on the surface modifications as well as the significant effect of the microstructure. To investigate microstructural changes metallographic cross sections were prepared.

The metallographic cross sections revealed that the microstructure changed due to the extended time at elevated temperatures evoked by the repetitive loading. Images a) and b) in figure 4.44 show the results. Besides cavities and small cracks, which formed within the hills and were the result of compressive and tensile stresses in combination with the low yield strength and grain boundary strength of recrystallised tungsten, recrystallisation and substructures like grain nucleation and subgrain formation were detected up to ∼ 240 µm below the exposed surface.

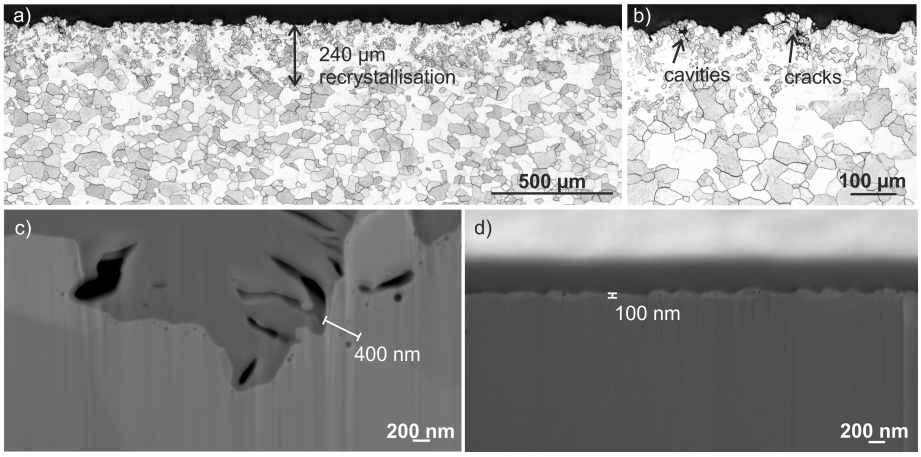


Figure 4.44: Images a) and b) show metallographical cross sections, which illustrate the change of the microstructure of an R sample after 100,000 laser pulses. The images in the bottom row show FIB cross section of helium bubble formation within c) the loaded area and outside d).

Continuative EBSD analyses exhibited that up to a depth of ∼ 160 µm plenty of small angle grain boundaries with angles between 3.5° and 10° were observed (figure 4.45 d)). With respect to the small angle grain boundaries, the examination revealed that the majority of these grains were completely recrystallised and had the same crystal orientation in exposure direction (figure 4.45 a) - c) and figure 4.46). In addition, from a depth of ∼ 160 µm up to a depth of ∼ 360 µm most of the original grains revealed substructures. These results exhibited the impact of the temperature gradient on the microstructure. Concerning applications in future fusion devices, these results demonstrated that a high amount of stress cycles in conjunction with

high base temperatures and the temperature increase during each thermal shock will lead to significant microstructural changes that further deteriorate the thermal shock and fatigue performance.

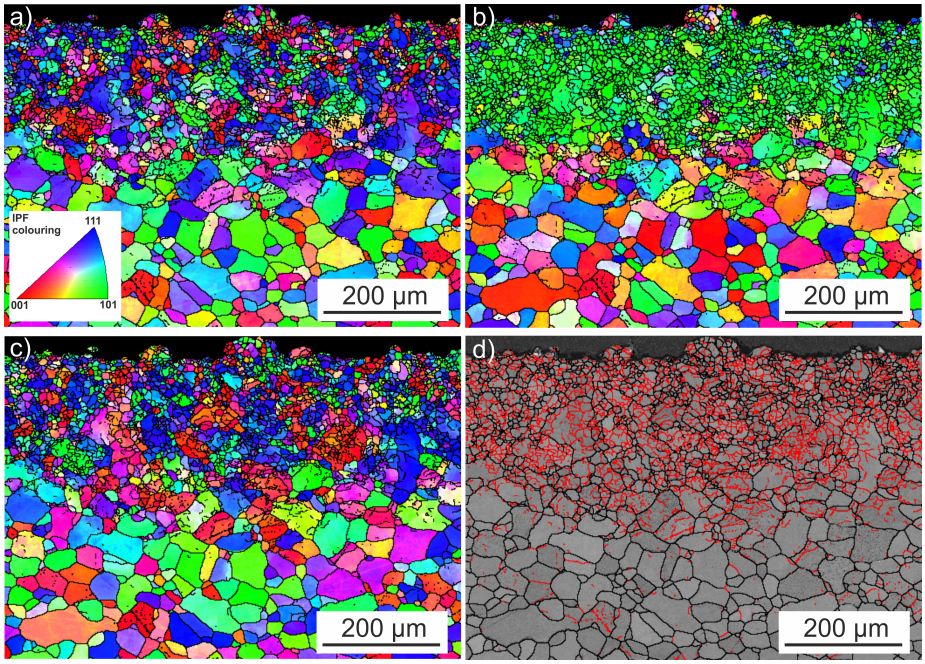


Figure 4.45: Images a) - c) illustrate the crystal orientation of subgrains and new recrystallised grains of a cross sections of an R sample that was exposed to 100,000 laser pulses. Thereby, a) and c) depict the orientation of the crystal parallel to the loading direction and b) in loading direction. Image d) shows the amount of small angle grain boundaries (in red) and of original grain boundaries (in black).

Furthermore, pronounced nano structures formed at the surface, which can be seen on image c) in figure 4.43. In coincidence with the results of the R sample after 10,000 laser pulses and compared with the other sample types, the surface appeared highly spongy. Additionally, tungsten tendrils and small melt droplets were observed in contrast to prementioned results. These findings underlined the tremendous influence of the microstructure on the damage behaviour. Moreover, the loose structure as well as the tendrils and melt droplets can lead to enhanced dust formation and erosion, if transient events strike these structures. Also, the helium induced bubble formation within the loaded area and outside was investigated via FIB cross section. Figure 4.44 c) depicts a FIB cross section image from an area below the exposure spot and 4.44 d) an image from a region that was solely exposed to deuterium he-

lium plasma. Outside the exposure spot bubbles formed in a layer with a depth of $\sim$ 100 nm and the largest bubbles had a major axis of $\sim$ 30 nm.

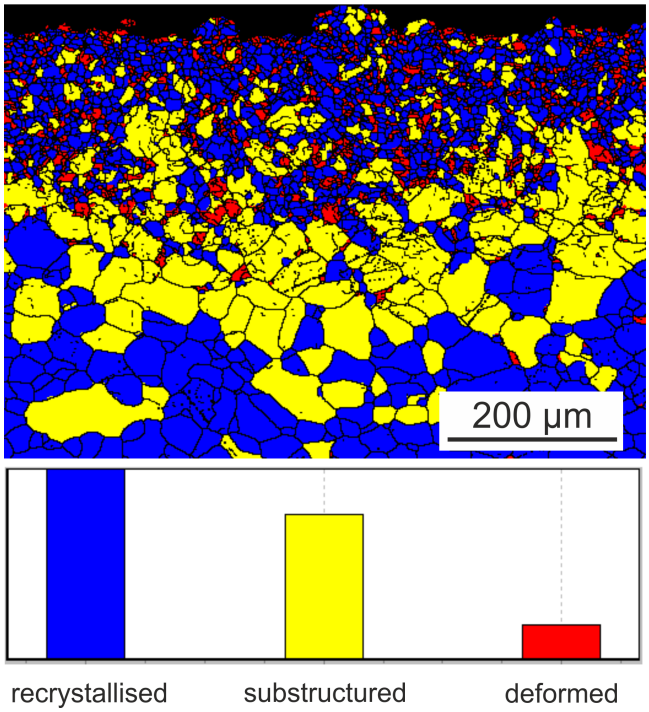


Figure 4.46: The image shows the ratio of recrystallised grains, substructured grains, and deformed ones of an R sample after 100,000 transient thermal events. The bottom of the image, depicts the original microstructure, whereas the top illustrates the near-surface region that was affected by ELM-like events and plasma exposure. The graph below exhibites the proportion of the different microstructural states.

In contrast, within the exposure spot bubbles were detected up to a depth of $\sim$ 400 nm and, here, the largest ones had a major axis of $\sim$ 97 nm. Compared with the other sample types after identical exposure conditions, the dimensions of the layer, in which the bubbles formed below the simultaneous loaded surface, were considerably larger and in addition, the amount of induced bubbles appeared higher but the size of the helium bubbles was smaller. Opposing to these results, the layer of bubble formation outside the exposure spot and the detected bubbles were the smallest by comparison. This difference between the two investigated regions originated from the higher mobility of helium atoms during simultaneous exposure as well as from the generation of additional trapping sites due to the thermal shock

events. The distinction to the other tested sample types could be explained by the varying microstructure and, therefore, differently developed defect concentrations and lattice deformations that acted as trapping sites for helium. In addition, the open volume between adjacent grains could have lead to deeper penetration and accumulation of helium, what could be substantiated by the larger extent of the layer, in which helium bubbles occurred.

4.5.2 Conclusion

The high pulse number experiments at an absorbed power density of 0.38 GW/m² and with simultaneous deuterium helium plasma exposure at 730 °C revealed that by increasing the pulse number the surface modifications and damages increased measurably. Precisely, 10,000 ELM-like events caused pronounced surface roughening and accessory, in the case of the L sample, microcracks occurred and the T sample showed cracks. By comparing the surface roughness evolution of all sample types after 10,000 transient events, the R sample exhibited the highest R_a values, while the T sample showed the least developed surface roughening. The low R_a value of the T sample was traced back to the formation of fatigue cracks that acted as stress relief and, therefore, suppressed distinct plastic deformation. Contrariwise, the crack formation substantiated the mechanical weakness and brittle behaviour of the transversal microstructure that was already detected after sequential experiments with 100 and 1000 laser pulses under equal loading conditions (subsection 4.3.2). Moreover, the high surface roughness of the recrystallised sample was attributed on the one hand to the ductile property and on the other hand to the low yield strength and grain boundary strength that prevented crack formation but caused higher plastic deformations due to the repetitive stress cycles.

Furthermore, the comparison of the arithmetic mean roughness values after 10,000 transient thermal events and after sequential tests with 1000 transient thermal events exhibited that the R_a values and, therefore, the surface roughness increased significantly for all sample types, even if the damage category remained constant. To illustrate, the arithmetic mean roughness of the R sample was four times higher after 10,000 ELM-like events than after 1000 and for L and T samples the surface roughness doubled. Besides the rising surface roughness, microstructural changes, like grain nucleation, subgrain formation, and recrystallisation, were observed for all tested samples types and, thereby, the characteristic of the microstructural changes increased with rising pulse numbers. In detail, the extent of the affected zone raised with the number of applied ELM-like events and, in addition, the ratio of grain nucleation/substructured grains to completely recrystallised grains increased too. Again, R samples showed the largest affected zone concerning microstructural changes, which could be reasoned by the microstructure and lower thermophysical properties of recrystallised tungsten. In addition to the microstructural changes, helium

induced bubble formation underneath the surface was detected. Here, the L sample revealed not only the largest layer, in which helium bubbles arose, but the largest bubbles in general. An explanation could be that the microstructure promoted the accumulation of helium in near-surface regions due to a high amount of trapping sites and/or that the absence of cracks also favored the helium retention because otherwise the cracks could have acted as relief for helium atoms like in the case of the T sample.

The results of experiments with 100,000 ELM-like events exihibited an exacerbation of the observed surface modifications and damages in comparison with tests with 10,000 ELM-like events or less. The L and T sample revealed enormous surface roughening with a pronounced hill-valley structure that was characterised by cracks and vacancies within the hills. In addition, distinct microstructural changes during the exposure, like substructured grains and recrystallised ones, supported the tremendous increase of surface modifications and damages. The measured R_a values were more than ten times higher than after 10,000 transient thermal loads. Such modified surfaces and near-surface microstructures depict lower mechanical properties and, therefore, will be more prone to overheating, melting, erosion of complete grains, dust formation, and in the worst case scenario the loss of complete surface parts. In contrast, the R sample showed only a slight increase of the surface roughness and did not exihibit a hill-valley structure. An explanation could be that due to the already recrystallised and, therefore, mechanically weaker microstructure, only the first 10,000 ELM-like events evoked distinct surface modifications/damages but then the material achieved some kind of saturation. Certainly, the fuzz formation was most pronounced and appeared entirely different from the nano structures, which were detected on the L and T sample. These results countered to the expectations regarding the recrystallised tungsten as it was also the case for sequential experiments described in subsection 4.3. Due to the considerably lower mechanical properties and thermal shock and fatigue performance, the worst surface modifications and damages were anticipated. However, further experiments are needed to validate the obtained results.

To conclude, the results exemplified that the risk of enhanced erosion, dust formation, as well as damage formation due to severe surface roughening and plastic deformations will tremendously escalate with the number of transient events. Furthermore, rising numbers of transient thermal events promote also microstructural changes, like grain nucleation, subgrain formation, recrystallisation etc., which have to be avoided because they deteriorate the mechanical properties, like yield strength, tensile strength and grain boundary strength, and, therefore, impair the thermal shock and fatigue performance. In addition, accumulation of helium and/or deuterium as well as bubble formation in near-surface regions disturb the heat transmission, evoke distortions of the tungsten lattice and, therefore, induce stresses

beyond those arising from transient thermal events. On that account, the surface temperature should be kept as low as possible to prevent microstructural changes and higher diffusion rates of deuterium/helium and transient events have to be mitigated at least. Taking the aforementioned number of expected unmitigated type-I ELMs during the service time in ITER into account ($n \gg 10^6$), the consequences for the PFMs/PFCs could be a significant degradation of the scheduled life time and/or premature failure. Based on the generated results, it is a debatable point whether the preferential transversal grain orientation will survive the severe loading conditions in ITER, satisfy the regulations for a smooth operation and, therefore, is the best solution for applications in future fusion devices.

5 Performance of steel under off-normal events

In ITER, the normal conditions that have to be sustained by the PFMs are already challenging, but additional off-normal events like VDEs, disruptions, or MGIs implicate an exacerbation of the loading conditions. Moreover, in devices beyond ITER, for example DEMO, the environmental conditions for the in-vessel components are even more severe, not least due to the long operation time between component exchange [40, 45, 51, 97]. In ITER, beryllium and tungsten are the main materials for PFCs, while stainless steel is used for remote areas such as port plugs. In DEMO, tungsten and tungsten alloys appear to be the main candidates for PFMs, but ferritic martensitic steels (e.g. EUROFER), which are foreseen as structural material in ITER and DEMO, could become contingent candidates for PFMs in less exposed wall positions as well [51]. Therefore, the ferritic martensitic steel P92 (see section 2.2) was investigated under fusion relevant loading conditions. The present comprehensive experiments examine several exposure parameters to predict the performance of P92 with regard to applications in ITER/DEMO [98].

5.1 Melting experiments in JUDITH 1

The first part of the experiments was conducted at the electron beam facility JUDITH 1 (see section 3.1) with the purpose to simulate wall loadings of steel surfaces under conditions, which create molten surfaces. Therefore, samples of the industrially available ferritic martensitic steel P92 (X10CrWMoVNb9-2) from BGH Edelstahl Freital GmbH were cut with the dimensions $12 \times 12 \times 5$ mm^3 and afterwards polished to a mirror finish to obtain a well-defined surface. P92 was chosen due to its cost-efficience and similarity to EUROFER.

The electron beam was used to simulate off-normal transient thermal events, such as photon flashes caused by mitigated disruptions or ELMs (MGI), that will strike the entire plasma facing surface. In this connection, the worst case scenario was investigated, in which these events caused melting of thin surface layers. In ITER, the expected heat flux factor of the photon pulses caused by the mentioned protection scenarios is in the range of $F_{HF} = 10 - 20$ MWm^{-2}s$^{0.5}$ [57] and steel will start

melting at $F_{HF} \sim 13$ MWm^{-2}s$^{0.5}$ [16]. Consequently, to guarantee melting of the sample surface, one batch of samples (**tests A**) were exposed at RT to pulses with a length of 3 ms and a power density of 245 MW/m^2, corresponding to a heat flux factor $F_{HF} \sim 13$ MWm^{-2}s$^{0.5}$, taking an electron reflection coefficient of 0.25 (based on Monte-Carlo simulations) into account. Moreover, different pulse numbers (10, 100, and 1000) were applied and the loaded area had a size of 8×8 mm^2. On the second batch of samples (**tests B**), 10 and 100 electron beam pulses with a pulse duration of 1 ms and a power density of 708 MW/m^2 ($F_{HF} \sim 22$ MWm^{-2}s$^{0.5}$) similar to mitigated ELMs) were applied and resulted in a surface temperature considerably above the melting point. Here, the loaded area had to be downscaled to 6×6 mm^2 to achieve the intended absorbed power density. These tests were performed at RT as well. Afterwards, the samples were examined by laser profilometry and scanning electron microscopy to obtain a detailed analysis of the surface morphology and damage conditions. In the following table all loading conditions are summarised.

Table 5.1: Overview of the loading conditions of melting tests in JUDITH 1.

test parameter	**tests A**	**tests B**
loaded area [mm^2]	8×8	6×6
pulse duration [ms]	3	1
pulse number	10 / 100 / 1000	10 / 100
abs. power density [MW/m^2]	245	708
F_{HF}[MWm^{-2}s$^{0.5}$]	13	22
base temperature [°C]	RT	RT

5.1.1 Results and discussion

Figure 5.1 illustrates exemplarily a sample surface after 1000 events at 245 MW/m^2 (5.1 a)) and after 10 events at 708 MW/m^2 (5.1 b)). Image 5.1 a) displays the pronounced hill-valley structure that had formed after 1000 electron beam pulses. Moreover, cracks emerged in the valleys after 1000 electron beam pulses. The fact, if the surface first cracked and then started to melt locally could not be proved by destructive cross section analysis since subsequent experiments at PSI-2 with these samples were planned. Furthermore, the hills were larger in the middle of the exposed area, which is an effect of the scanning path and the associated slightly inhomogeneous loading and of the lack of a lateral heat transfer in the centre of the loaded area. In detail, experiments with pulse durations > 1 ms exhibited that the heat in the centre of the loaded area can only dissipate in bulk direction (z direction) due to the absence of a lateral thermal gradient, whereas the heat at the edges can propagate in x and y direction [99]. Consequentially, the egdes remained cooler, while the centre of the loaded area experienced higher maximum tempera-

tures, which led to repetitive, shallow melting and the occurrence of super-imposed melt layers. Furthermore, the motion of these melt layers due to cohesive forces caused higher hills and even merged hills, while the cracks in the valleys prevented melt motion across the cracks. This effect intensified by increasing the applied pulse number. In general, the samples of tests A, which were exposed at 245 MW/m², experienced greater surface modifications.

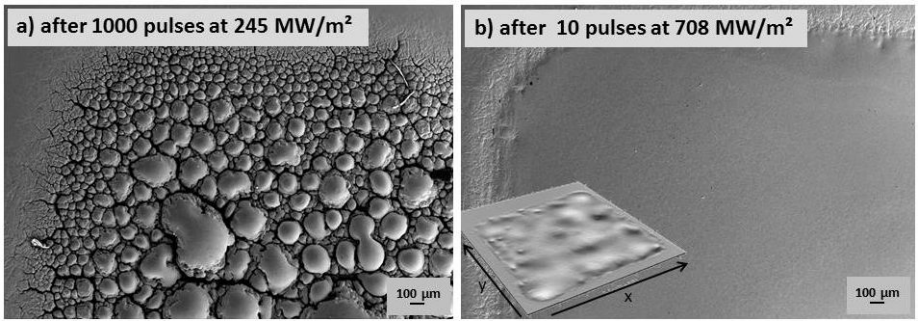


Figure 5.1: SEM images of the surface morphology after exposure to a) 1000 (pulse duration 3 ms) electron beam pulses at 245 MW/m² and b) 10 (pulse duration 1 ms) pulses at 708 MW/m². 1000 pulses at the lower power density caused a pronounced hill-valley structure, whereas 10 pulses at 708 MW/m² led to a slightly wavy surface that is plotted on the profilometer scan at the bottom left corner.

The analysis of samples exposed at 708 MW/m² exhibited that after 10 electron beam pulses (see figure 5.1 b)), the exposed area was only slightly wavy. Even an increase up to 100 electron beam pulses did not have an impact on the surface morphology similar to tests at 254 MW/m² with the same pulse number. Here, the loaded surface appeared slightly wavy. Reasons for these dissimilar surface modifications were found in the different pulse numbers and pulse durations. Especially, the varying power densities had a massive influence on the damage behaviour. More precisely, stainless steel will start to melt at $F_{HF} \sim 13$ MWm^{-2}s$^{0.5}$ [58], which correlates with the F_{HF} of tests A that showed the hill-valley structures. Since tests B were executed at $F_{HF} \sim 22$ MWm^{-2}s$^{0.5}$, the melting temperature was considerably exceeded. Thereby, the material experienced fast, intense melting within a minor pulse duration (1 ms) in comparison with long pulse duration tests A (3 ms) and also a faster cool down between single pulses. Therefore, it was assumed that the generated melt layers already started to solidify before significant melt motion could occur. Moreover, this can also be attributed to the lateral heat transfer, which was homogeneous for the whole exposed area in contrast to the heat transfer of the long pulse duration tests A.

Additionally, the surface roughness was measured by laser profilometry and compared. The R_a values confirmed the dissimilar surface evolution. In both test series, the R_a values increased with rising pulse numbers but the samples of tests A showed higher values at the same pulse number. All measured data can be found in table D.1 in appendix D. For the subsequent experiments at PSI-2, the samples with the strongest surface modifications were used from both test series. To investigate the worst case, specimens that were exposed to 1000 pulses in test A and 100 pulses in test B were used.

5.2 Subsequent sequential and simultaneous tests at PSI-2

At PSI-2, the preloaded samples, described in section 5.1, were exposed to simultaneous and sequential thermal and particle loads according to the loading sequence explained in section 4.2. The transient thermal events with ELM characteristics were executed by laser with a repetition frequency of 0.5 Hz, a pulse duration of 1 ms, pulse numbers of 100 and 1000, and absorbed power densities in the range of 160 - 660 MW/m². The particle exposure was realised by pure deuterium plasma with a flux of $\sim 6 \times 10^{21}$ $m^{-2}s^{-1}$ and a fluence corresponding to 100 laser pulses of up to $\sim 1.2 \times 10^{24}$ m^{-2} ($\sim 1.2 \times 10^{25}$ m^{-2} corresponding to 1000 laser pulses). The preloaded targets were mechanically clamped to a holder and heated to a base temperature of 400 °C. A summary of the experimental conditions is given in table 5.2.

Table 5.2: Overview of the loading conditions of subsequent sequential and simultaneous experiments at PSI-2.

loading conditions	preloaded **A** samples	preloaded **B** samples
loading sequence (4.2.1 figure 4.2)	1 - 4	1 - 3
pulse duration [ms]	1	1
repetition frequency [Hz]	0.5	0.5
pulse number	100 / 1000	100
power density [MW/m²]	160 - 660	160 - 660
base temperature [°C]	400	400
D flux [$m^{-2}s^{-1}$]	6×10^{21}	6×10^{21}

Furthermore, a bias voltage of 60 V accelerated the particles towards the sample, which resulted in an ion energy of around 35 eV. Another important parameter was the different size of the preloaded areas. This circumstance was taken into account

by adapting the loading sequence. In detail, the preloaded samples of test A were exposed according to the sequences in figure 4.2, while for the preloaded samples of test B sequence four (4th spot) was skipped because the preloaded area was to small. Figure D.1 in appendix D provides the loading scheme of both samples. Afterwards, the induced surface modifications and damages were analysed by light microscopy, SEM, and metallographic cross sections.

5.2.1 Results and discussion

As mentioned in the previous section, type A samples had a larger preloaded area, so four spots with a different loading sequence could be applied (see figure D.1 a) in appendix D). Figure 5.2 exemplarily illustrates different exposure spots for the highest tested power density based on SEM images in the top row and metallographic cross section images in the bottom row. In general, the sequentially exposed surfaces did not show tremendous differences of the morphology in comparison to the only electron beam exposed surface. Only by rising the power density as well as the pulse number, the surface morphology started to change discernibly. In particular, distinct melting and melt motion occured, which resulted in the merging of single hills. In summary, based on the analysis of SEM images, the loading order had no influence on the damage behaviour or surface modifications.

Furthermore, metallographic cross sections were prepared for a detailed analysis. Again, no influence of the loading sequence could be detected. Also, surface roughness measurements did not show any correlation between damage behaviour and loading order. Even a dependence of the R_a values (see appendix D table D.2) on the applied power density was not found. Instead, isolated cracks were located in the valleys but most of the cracks originated inside the hills. This result can be seen on the cross section images in the bottom row of figure 5.2.

Moreover, a correlation between the cracks and the loading parameters was not detected. In most instances, the cracks propagated perpendicular to the loaded surface both in the valleys and inside the hills. Here, the cracks in the valleys can be seen as artificial obstacles, which seemed to prevent further melt motion across the cracks and the formation of a liquid film that could cover the wavy surface. However, several horizontal cracks were found within the hills, in some cases they nearly extended through the entire width of the hill. The detrimental effects of such horizontal cracks are the disturbance of the heat transmission, which will result in overheating, melting, and/or the loss of material. All these effects have to be prevented in a fusion device. An explanation for the formation of cracks was either due to the stresses generated by the thermal shocks and the rapid cool down after each thermal shock and/or based on hydrogen accumulations that generated additional stresses inside the material. Besides, hydrogen affects the material adversely

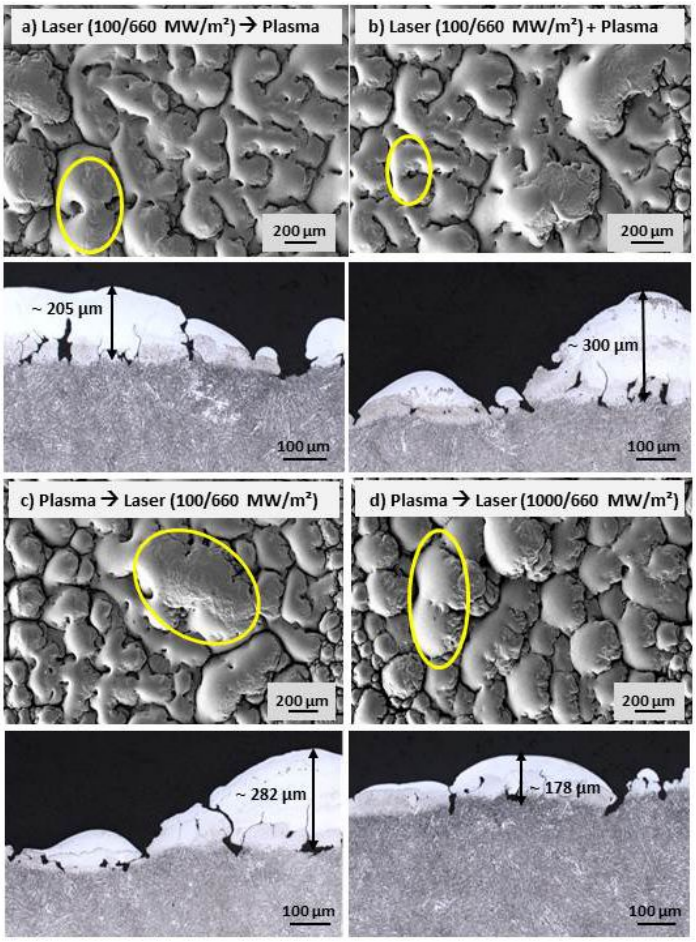


Figure 5.2: A preloaded sample of test series **A** after exposure in PSI-2 at the highest tested power density of 660 MW/m². The top row shows SEM images of the different loading spots and the bottom row illustrates related metallographic cross section images of areas within these loading spots. At some representative positions the merging of single hills is marked by circles.

because it drives embrittlement. In addition to cracks, cavities were ascertained in the hills, which could be a result of the repeated shallow melting of the top of the hills followed by a fast solidification and trapped deuterium. In some exceptional cases, it could have been also an effect of the cross section preparation if a crack entirely encircled material parts, which then dropped out. However, cavities just like horizontal cracks act as thermal barriers that disturb the heat transport, which in turn could cause overheating and melting, both consequences that have to be avoided.

Furthermore, the merging of single hills was also noticed on the cross section images. Certainly, an obvious dependence of the height of the hills on the power density was detected, the dependence of the loading sequence was slight. It can be stated that the lowest hills of 100 µm were detected after initial laser exposure followed by plasma loading at 160 and 380 MW/m². For the highest tested power density the sequence with 1000 laser pulses generated the lowest hills. Moreover, the highest hills occurred almost for all tested power densities after simultaneous exposure, e.g. 300 µm above the original surface after tests at 660 MW/m² (see figure 5.2 bottom row). These results were identified by height determinations via profilometry and metallography. Additionally, the interfaces between liquid and solid phases for the melt cycles were detected on metallographic cross sections. The cross sections showed the microstructural/phase transformation of the solidified melt that will e.g. reduce the mechanical strength considerably.

Different from the preloaded samples of tests A, the preloaded area on samples of tests B was smaller and, therefore, the fourth exposure spot, initial plasma loading followed by 1000 laser pulses, was not possible, while all other loading conditions remained the same (see figure D.1 b) in appendix D). The results revealed a significant difference to preloaded A samples. Here, the exposure sequence had a substantial impact on the surface modifications, which is displayed in figure 5.3 by SEM in the top row and metallographic cross section images in the bottom row.

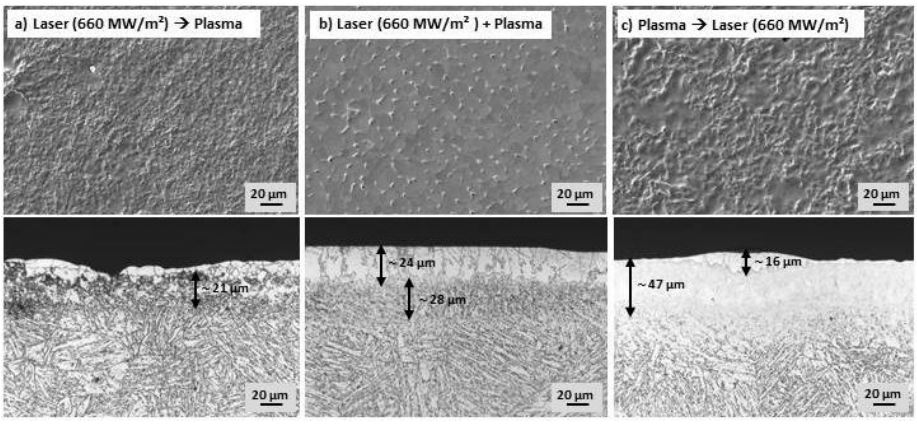


Figure 5.3: Representative SEM images (top row) and metallographic cross section images (bottom row) of preloaded B samples after sequential and simultaneous tests at 660 MW/m². The influence of the loading order is clearly differentiable on the SEM images.

First, the arithmetic mean roughness was measured, which showed an increase of

the surface roughness with rising power densities but not a correlation with the loading sequence. The R_a values can be found in appendix D table D.3. Moreover, small cracks were observed for each loading sequence at 160 MW/m². Above 160 MW/m² cracks were also detected in some cases but the occurrence seemed randomly. Only at the highest tested power density a slight connection between the crack formation and loading sequence was found. Here, small cracks originated only after initial laser exposure followed by plasma loading and were accompanied by partially molten parts. The reverse loading order did not generate small cracks but larger molten areas. This indicated that the plastic deformation was higher and/or the deuterium content in the near-surface region was higher due to the initial plasma loading. Consequentially, the thermal contact decreased and/or the heat transmission was disturbed by deuterium accumulations. Reasons for the formation of small cracks were tensile stresses, which exceeded the tensile strength of the material, embrittlement due to deuterium accumulations in the near-surface region, and altered mechanical properties of the solidified melt. These results emphasised the significant impact of the exposure sequence on the surface morphology. Furthermore, simultaneous exposure at 660 MW/m² led to small holes on the surface, which can be seen in figure 5.3 b) in the top row. These holes were evenly distributed within the entire loaded area and frequently at grain boundary junctions.

An explanation was found by taking the epitaxial grain growth at the near-surface region into account, which can be seen on the cross section images in the bottom row of figure 5.3. Due to the melting and subsequent thermal shock exposure, the microstructure changed and grains with straight and perpendicular boundaries to the surface grew. To illustrate this point, grain boundaries are the weakest points in the microstructure and, therefore, they are the preferential and easiest locations for deuterium to interact with the material. Moreover, the outgassing and/or accumulation of deuterium accompanied by the arising stresses could be an explanation of the observed formation of holes. Further investigations like weight loss measurements might be helpful to verify this assumption.

To complete, the influence of the loading order was reflected in the change of the microstructure. Metallographical cross sections revealed the transition between the original microstructure, an interlayer dominated by carbides, and the ferritic layer with epitaxial grains on the surface. The comparison of the microstructure after exposure at the same power density exhibited differences in the characteristics of the single interfaces. While the epitaxial grain growth was most pronounced for simultaneous loads, accompanied by a definite delimitation of the interfaces with varying microstructures, a clear distinction could not be easily detected for the subsequent loading orders. At this point, it is difficult to issue a statement about the driving mechanisms or responsible reasons for the observed differences in the microstructure. Therefore, further experiments would be helpful to gain deeper insights.

5.3 Conclusion

The experiments combining melting and the creation of solidified surfaces by pure thermal loads with sequential and simultaneous thermal and particle exposure revealed that the kind of preloading and associated with it the degree of pre-damage influenced the surface morphology significantly. In turn, this substantial change of the surface morphology had a substantial impact on the performance and damage behaviour of the tested ferritic martensitic steel. The results of the electron beam tests exhibited that with increasing pulse numbers for experiments with smaller F_{HF} (tests A), the sample surface developed a pronounced hill-valley structure. For tests B, which were executed at the higher F_{HF}, the specimens ended up with slightly wavy surfaces. This difference could be evoked by a complete cool down between two successive pulses, the lower amount of pulses in general, and the F_{HF}, which was considerably above $F_{HF} \sim 13$ MWm^{-2}s$^{0.5}$, where steel starts to melt. In conclusion, the electron beam experiments caused enhanced melting, the formation of melt-layers, and melt motion.

The second part of this experiment, the sequential and simultaneous exposure to thermal and deuterium particle loads, revealed that the sequential loading had no effect on the preloaded samples of test A. Here, only the applied power density as well as the pulse number showed an influence on the surface modifications. This influence was determined by the observation of the coalescence of single hills due to successive melting and melt motion. The arising consequences for applications in a fusion device could be continuous accumulations of material on the one hand and material removal on the other hand, which would change the properties/design of the components and raise the risk of material loss extensively.

The preloaded samples of tests B acted entirely different. In detail, the loading sequence had a significant impact on the surface modifications and damage behaviour, which became more distinct with increasing power densities. The surface roughness increased considerably accompanied by partially molten areas for sequences that started or ended with laser exposure. Thereby, the sequence ending with laser exposure generated the higher surface roughness and amount of molten areas. An explanation was found in arising stresses, generated by thermal shocks and deuterium concentrations in the near-surface region, which led to plastic deformation. Moreover, here the plastic deformation was more distinct because ending with laser exposure implied that at the beginning of the sequence, the amount of hydrogen in the near-surface region was higher than for the sequence vice versa and this caused additional stresses inside the material. Another important result was the detection of small holes after simultaneous exposure, which is the most important loading

sequence concerning future fusion devices, that could be an effect of outgassing hydrogen. If this effect would scale-up, tremendous material loss would be the consequence, which would pollute the plasma and degrade the material and component performance.

Regarding the operation of DEMO or a fusion device in general, these results, like the distinct surface roughness increase, indicate that fatigue effects could appear faster if higher pulse numbers are applied and, therefore, the risk of crack formation, origination of thermal barriers, melting, and erosion would rise [100]. All these effects would shorten the lifetime of the in-vessel components and/or negatively influence a smooth operation of the fusion device. To further support the conclusions and answer open questions, following experiments should aim on comparable, initial conditions for the electron beam test and, in addition, synergistic effects of steady state hydrogen/helium exposure and higher numbers of thermal shocks have to be characterised. To identify important threshold values and material parameters to make accurate forecasts about the lifetime and performance of the material, the exposure parameters have to be expanded.

6 Overall conclusion and outlook

This work focuses on the investigation of tungsten under varying thermal and particle exposure conditions in terms of plasma composition, absorbed power density, base temperature, and number of transient thermal events. In addition, the performance of ferritic martensitic steel was analysed with respect to melting and subsequent thermal and particle exposure of the solidified surfaces. The basis, for the investigations within this work, were previous experiments with pure thermal exposure, which are illustrated in chapter 4 section 4.1. The rest of chapter 4 is divided into 4 sections, which discuss the influence of sequential and simultaneous exposure with a pure deuterium plasma (section 4.2) and with a mixed deuterium helium plasma (section 4.3) at different base temperatures and relatively low pulse numbers on the thermal shock and damage performance of tungsten. In section 4.5, the impact of high pulse numbers ($\leq 100,000$) under equal loading conditions was investigated, whereas chapter 5 examined the effect of successive melting and sequential/simultaneous loads on steel. The results of the individual sections/chapters were illustrated at the end of the corresponding section/chapter (cf. section 4.5 and 5.3) or, like in the case of section 4.2 and section 4.3, the results/conclusions were presented in an own section 4.4. This short chapter exhibits a general overview of the material modifications and damages, which can be expected in future fusion devices like ITER and DEMO.

The ITER relevant sequential and simultaneous exposure of tungsten revealed that already at moderate pulse numbers (≤ 1000) the different base temperatures, variations of the power density, the microstructure of the test specimens, and the different plasma compositions (e.g. the deuterium to helium ratio) had a significantly deteriorating impact on the thermal shock response and on the damage performance. On the basis of the obtained results, synergistic effects have been evaluated in detail and were descrided. To illustrate, the base temperature has a strong impact on the ductility of the material and should be $>$ DBTT. However, higher base temperatures lower the yield and tensile strength, which in combination with high power densities and the varying performance of the different microstructures (as-received microstructures, especially transversal samples (T) with grains oriented perpendicular to the loaded surface and preferred for ITER), caused a remarkable increase of the surface modifications and damage evolution, whereas the damage evolution

of recrystallised tungsten was less severe as expected. Therefore, the power density must remain below the identified damage threshold, which could be managed by mitigation and/or suppression of transient events. Another consideration could be the evaluation of the impact of pre-damaged components on the plasma performance during the operation of fusion devices. Furthermore, the exacerbating impact of deuterium and helium on the material performance was highlighted. In comparison with pure thermal experiments [61], the performance of tungsten deteriorated considerably (e.g. crack formation) accompanied by significant surface modifications (e.g. blister formation). In addition, with rising pulse numbers, the surface roughness raised for all tested sample types and microstructural changes, like grain nucleation and recrystallisation, were observed. The experiments proved that the favored transversal grain orientation for applications in ITER could lead to extensive problems, like enhanced erosion, cracking, and melting.

The high pulse number experiments revealed that the damage increased tremendeously with the number of applied pulses, especially for samples with horizontal (L) and perpendicular (T) grain orientation to the exposed surface. Furthermore, fluence dependent microstructural changes as well as helium accumulations in near-surface regions that will alter the mechanical properties, were observed and quantified. Having in mind that ITER will experience several millions of ELMs with unmitigated power densities of approx. 1 GW/m² in addition to the higher and extented particle fluxes, this will lead to an irreversible material degradation and component failure, repectively.

Additionally, the performance of molten/solidified ferritic martensitic steel surfaces under sequential and simultaneous thermal and particle loads with deuterium plasma background was investigated. It was demonstrated that pre-damage substantially influenced the surface modifications during sequential/simultaneous loads and deteriorated the damage behaviour in general. Thereby, distinct surface roughening, melting, and pores were observed after sequential/simultaneous exposure in dependence on the applied power density and loading sequence. Regarding the operation in DEMO or commercial fusion devices beyond, fatigue effects and extensive damage formation, like melting, erosion, and cracking, will appear if the number of pulses increases, which will strike the plasma facing wall and if steel is not only exposed to deuterium but also to intense helium and neutron fluxes in the order of $\sim 10^{24}$ $m^{-2}s^{-1}$ [40].

The presented results within this work exhibit that not only tungsten but any other material that will be used as PFMs in future fusion reactors has to deal with extremely harsh synergistic loading conditions. Less demanding loading scenarios as they are expected in ITER at this point, will still bare the risk of tremendous surface and microstructural modifications, damages, and performance degradations. To

solve the problems, which arise due to steady state heat loads up to 20 MW/m², transient events with power densities above 1 GW/m², as well as high hydrogen, helium, and neutron fluxes collaborations between varying scientific and industrial fields are absolutely essential. Therefore, collaborative work on fields like material improvement and/or material strengthening (e.g. fibre reinforcement), the design of PFCs, and the prevention/limitation of normal and off-normal transient events or at least their mitigation, will assists to find enhancements and solutions. Furthermore, continuing experiments on pre-damaged samples would be helpful to study the impact of the induced damages on the material performance and to draw conclusions about the consequences for the plasma performance during the operation of future fusion reactors.

A Appendix: Detailed measurement results of sequential and simultaneous tests

A.1 Tests with deuterium plasma at 400 °C

The arithmetic mean roughness R_a and the average values for the crack width and the crack depth in µm were measured for each loading spot/sequence and all tested absorbed power densities. Thereby, the abbreviations 1 - 4 represent the loading sequence [1: laser → plasma, 2: laser + plasma, 3: plasma → laser, 4: plasma → laser (1000 pulses)] as described in figure 4.2.

In some cases, the observed cracks could not be detected on the metallographical cross sections. This circumstance can be explained by minor crack depth, deviation between metallographical cut line and crack position etc..

Table A.1: Arithmetic mean roughness R_a in µm for all sample types tested with pure deuterium plasma that were presented in subsection 4.2.1.

grain structure	L				T			
sequence	1	2	3	4	1	2	3	4
0.19 GW/m²	0.3	0.35	0.26	0.24	0.12	0.15	0.11	0.12
0.38 GW/m²	0.29	0.31	0.28	0.40	0.15	0.14	0.13	0.25
0.64 GW/m²	0.47	0.73	0.71	4.19	0.49	0.51	0.50	2.63

grain structure	R			
sequence	1	2	3	4
0.19 GW/m²	0.20	0.19	0.21	0.32
0.38 GW/m²	0.28	0.29	0.27	0.97
0.64 GW/m²	0.78	0.71	0.67	3.29

Table A.2: Average values of the crack width in µm for all cracked sample types that were presented in subsection 4.2.1.

grain structure	T				R			
sequence	1	2	3	4	1	2	3	4
0.19 GW/m²	-	-	-	-	0.17	0.11	0.07	0.20
0.38 GW/m²	1.25	4.00	3.24	3.70	0.35	0.21	0.61	1.00
0.64 GW/m²	2.18	5.96	11.19	-	10.90	-	-	-

Table A.3: Average values of the crack depth in µm for all cracked sample types that were presented in subsection 4.2.1.

grain structure	T				R			
sequence	1	2	3	4	1	2	3	4
0.19 GW/m²	-	-	-	-	51.55	7.24	8.02	19.26
0.38 GW/m²	7.65	13.68	17.18	66.67	36.84	70.00	126.56	110.12
0.64 GW/m²	511.70	51.30	86.98	-	-	-	-	-

A.2 Tests with deuterium plasma at 730 °C

The Sketch [79] depicts the high temperature sample holder with ceramic spacers and an ohmic heater. Again, the samples were circularly positioned to guarantee consistent plasma exposure.

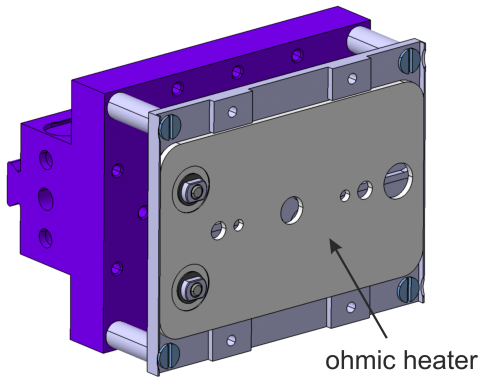


Figure A.1: Sketch of the high temperature sample holder for experiments at 730 °C base temperature.

Table A.4: Arithmetic mean roughness R_a in µm for all sample types tested with pure deuterium plasma that were presented in subsection 4.2.2.

grain structure	L				T			
sequence	1	2	3	4	1	2	3	4
0.19 GW/m²	0.12	0.14	0.12	0.13	0.13	0.11	0.13	0.14
0.38 GW/m²	0.13	0.13	0.12	0.22	0.12	0.12	0.13	0.14
0.76 GW/m²	0.26	0.25	0.24	0.89	0.20	0.20	0.17	0.72

grain structure	R			
sequence	1	2	3	4
0.19 GW/m²	0.15	0.15	0.15	0.29
0.38 GW/m²	0.20	0.20	0.20	0.65
0.76 GW/m²	0.38	0.41	0.40	1.95

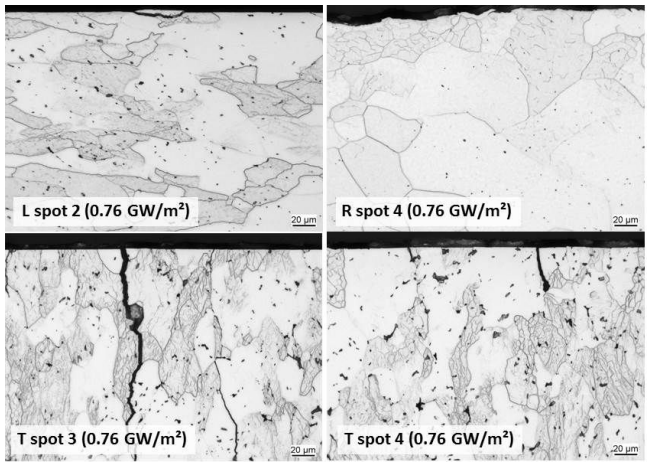


Figure A.2: This picture shows exemplarily metallographic cross section of all samples types after tests at 730 °C. Starting with an image of a L sample on the left side of the top row, a R sample on the right side of the top row and in the bottom row there are two images of T samples after different loading sequences at the same power density. These two images illustrade the diverse crack development after the same sequence, same power density but varying pulse number (spot 3 100 pulses, spot 4 1000 pulses). Furthermore, the cross sections indicate clearly the distinct grain nucleation that was detected for all sample types and almost each loading scenario.

Table A.5: Average values of crack width and crack depth for **T** samples presented in subsection 4.2.2.

crack parameter	width [µm]				depth [µm]			
sequence	1	2	3	4	1	2	3	4
0.19 GW/m²	-	-	-	-	-	-	-	-
0.38 GW/m²	0.18	0.11	0.17	0.42	-	-	-	20.58
0.76 GW/m²	0.92	0.88	3.61	2.33	20.81	14.80	57.74	17.63

A.3 Tests with deuterium helium(6 %) plasma at 400 °C

Table A.6: Arithmetic mean roughness R_a in µm for all sample types tested with mixed deuterium-helium plasma that were presented in subsection 4.3.1.

grain structure	L				T			
sequence	1	2	3	4	1	2	3	4
0.19 GW/m²	0.14	0.14	0.16	0.15	0.09	0.09	0.09	0.09
0.38 GW/m²	0.11	0.10	0.12	0.15	0.10	0.10	0.09	0.10
0.76 GW/m²	0.25	0.25	0.24	1.08	0.15	0.16	0.13	0.21

grain structure	R			
sequence	1	2	3	4
0.19 GW/m²	0.13	0.14	0.14	0.27
0.38 GW/m²	0.21	0.22	0.21	0.93
0.76 GW/m²	0.30	0.31	0.32	1.44

Table A.7: Average values of crack width and crack depth in µm for **L** samples presented in subsection 4.3.1.

crack parameter	width [µm]				depth [µm]			
sequence	1	2	3	4	1	2	3	4
0.19 GW/m²	-	0.13	0.16	-	-	7.39	15.95	-
0.76 GW/m²	0.51	-	-	-	16.25	-	-	-

Table A.8: Average values of crack width and crack depth for **T** samples presented in subsection 4.3.1.

crack parameter	width [µm]				depth [µm]			
sequence	1	2	3	4	1	2	3	4
0.19 GW/m²	< 0.13	< 0.13	0.13	0.20	4.62	8.21	1.72	7.53
0.38 GW/m²	-	-	< 0.13	0.22	-	-	< 0.13	5.10
0.76 GW/m²	0.19	2.82	0.39	3.41	16.94	54.41	19.70	28.26

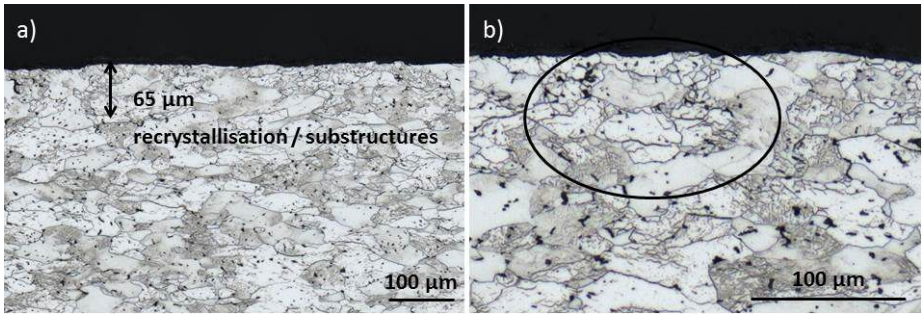


Figure A.3: The figure shows metallographical cross section images of an L samples after initial plasma exposure followed by 1000 laser pulses at 0.76 GW/m², which illustrate the microstructural changes within the exposed area. Image a) depicts an overview, whereas image b) shows a detail of the area, in which the microstructural changes are highlighted.

A.4 Tests with deuterium helium(6 %) plasma at 730 °C

Table A.9: Arithmetic mean roughness R_a in µm for all sample types tested with mixed deuterium-helium plasma that were presented in subsection 4.3.2.

grain structure	L				T			
sequence	1	2	3	4	1	2	3	4
0.19 GW/m²	0.42	0.38	0.36	0.51	0.09	0.10	0.11	0.09
0.38 GW/m²	0.57	0.50	0.50	0.95	0.11	0.13	0.13	0.26
0.76 GW/m²	0.37	0.42	0.36	2.13	0.19	0.27	0.27	0.93

grain structure	R			
sequence	1	2	3	4
0.19 GW/m²	0.14	0.16	0.13	0.38
0.38 GW/m²	0.21	0.23	0.22	0.87
0.76 GW/m²	0.46	0.50	0.45	2.53

Table A.10: Average values of crack width and crack depth for **L** samples presented in subsection 4.3.2.

crack parameter	width [µm]				depth [µm]			
sequence	1	2	3	4	1	2	3	4
0.38 GW/m²	0.16	-	0.05	0.09	10.67	-	5.41	14.43
0.76 GW/m²	0.32	1.80	-	-	8.82	7.79	-	-

Table A.11: Average values of crack width and crack depth for **T** samples presented in subsection 4.3.2.

crack parameter	width [µm]				depth [µm]			
sequence	1	2	3	4	1	2	3	4
0.19 GW/m²	0.02	-	-	0.08	-	-	-	4.95
0.38 GW/m²	0.12	0.26	0.17	1.07	7.18	8.32	2.76	3.17
0.76 GW/m²	1.08	3.12	3.21	7.13	23.63	118.26	48.6	92.86

Table A.12: Average values of crack width and crack depth for **R** samples presented in subsection 4.3.2.

crack parameter	width [µm]				depth [µm]			
sequence	1	2	3	4	1	2	3	4
0.19 GW/m²	-	0.52	0.30	0.34	-	18.98	14.89	4.53

B Appendix: Detailed analysis results of sequential and simultaneous tests

B.1 Tests with deuterium plasma at 400 °C

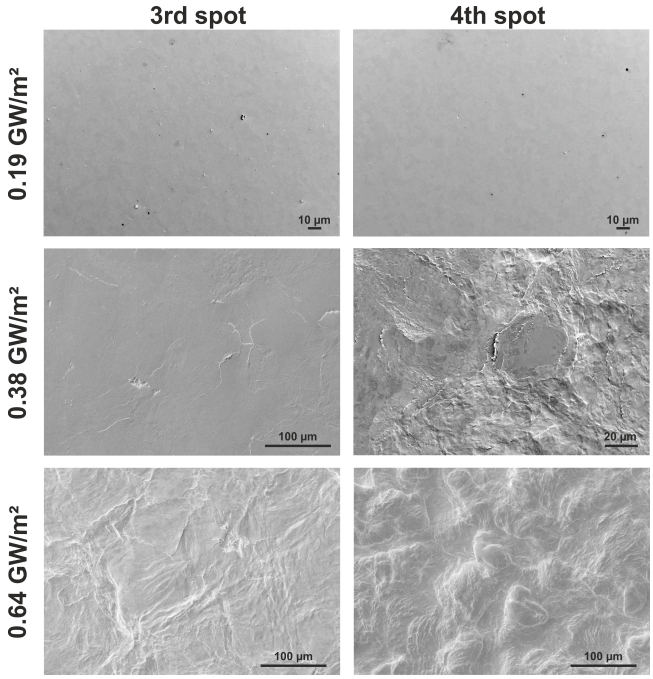


Figure B.1: Comparison of the damage evolution and categories of L samples after initial plasma exposure followed by 100 (3rd spot) and 1000 (4th spot) laser pulses at 400 °C on the basis of SEM images.

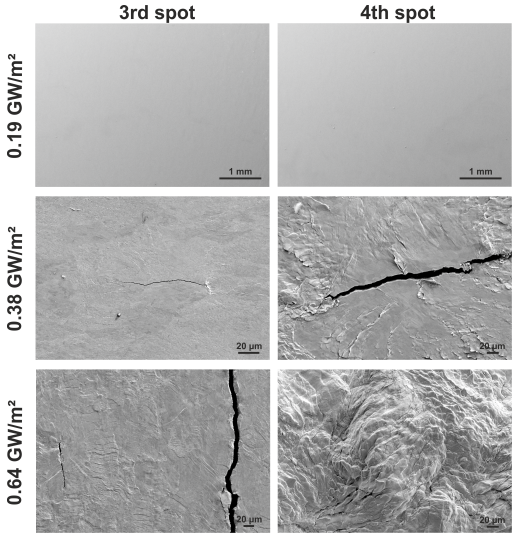


Figure B.2: Comparison of the surface modifications and damage categories of T samples after sequential exposure at 400 °C to deuterium plasma and 100 transient events (spot 3) and 1000 transient events (spot 4), respectively.

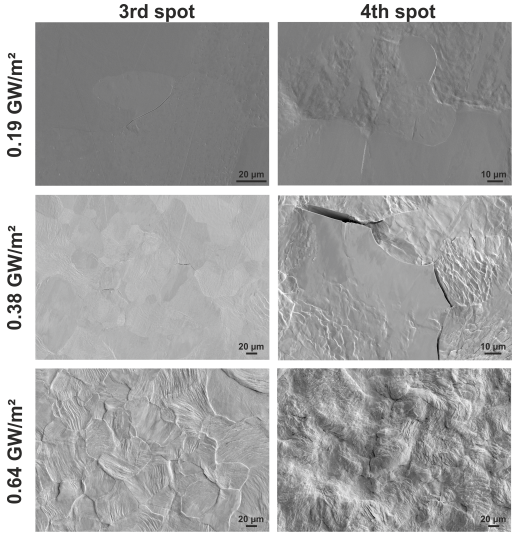


Figure B.3: Comparison of the surface modifications and damage categories of R samples after sequential exposure at 400 °C to deuterium plasma and 100 transient events (spot 3) and 1000 transient events (spot 4), respectively.

B.2 Tests with deuterium plasma at 730 °C

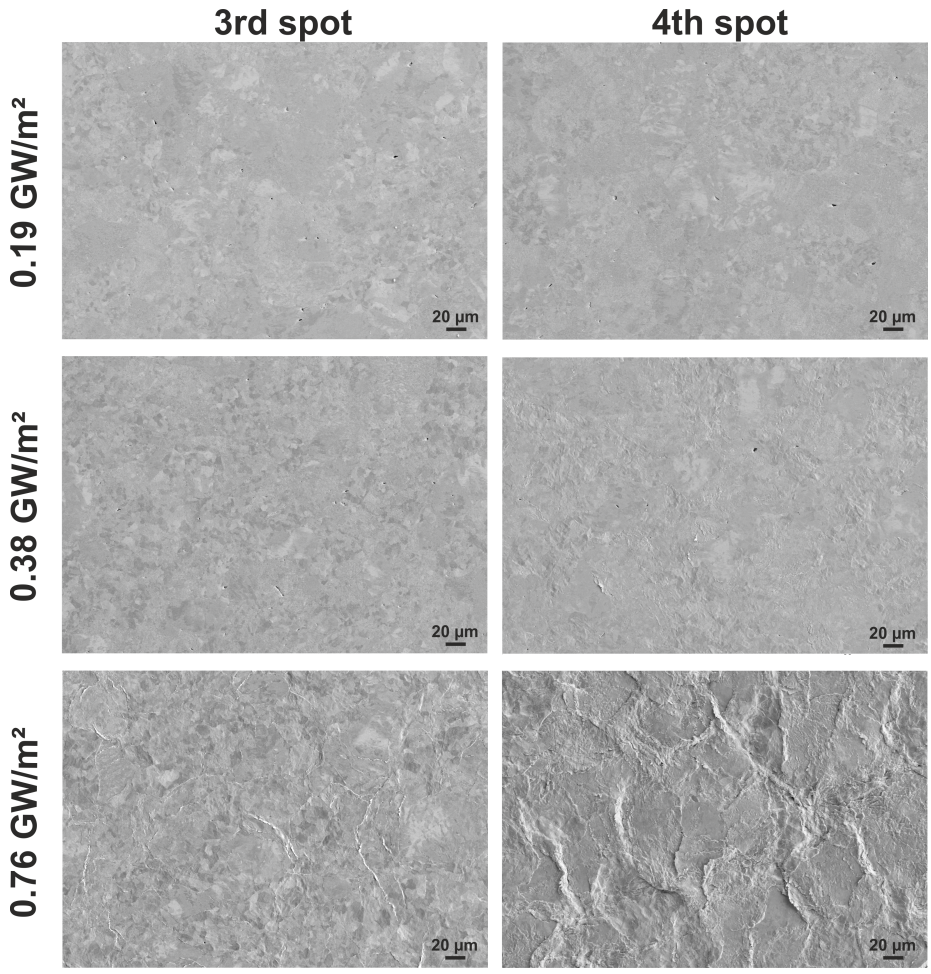


Figure B.4: Comparison of the surface modifications and damage categories of L samples after sequential exposure at 730 °C to deuterium plasma and 100 transient events (spot 3) and 1000 transient events (spot 4), respectively.

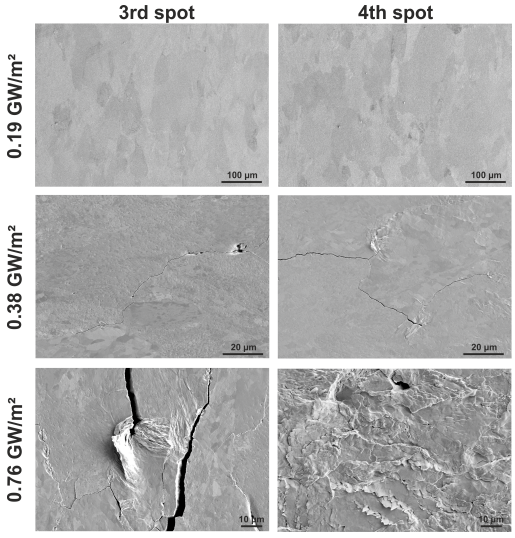


Figure B.5: Comparison of the surface modifications and damage categories of T samples after sequential exposure at 730 °C to deuterium plasma and 100 transient events (spot 3) and 1000 transient events (spot 4), respectively.

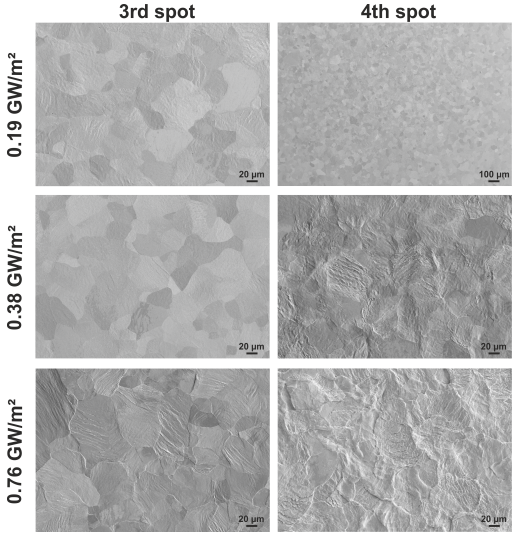


Figure B.6: Comparison of the surface modifications and damage categories of R samples after sequential exposure at 730 °C to deuterium plasma and 100 transient events (spot 3) and 1000 transient events (spot 4), respectively.

B.3 Tests with deuterium helium(6 %) plasma at 400 °C

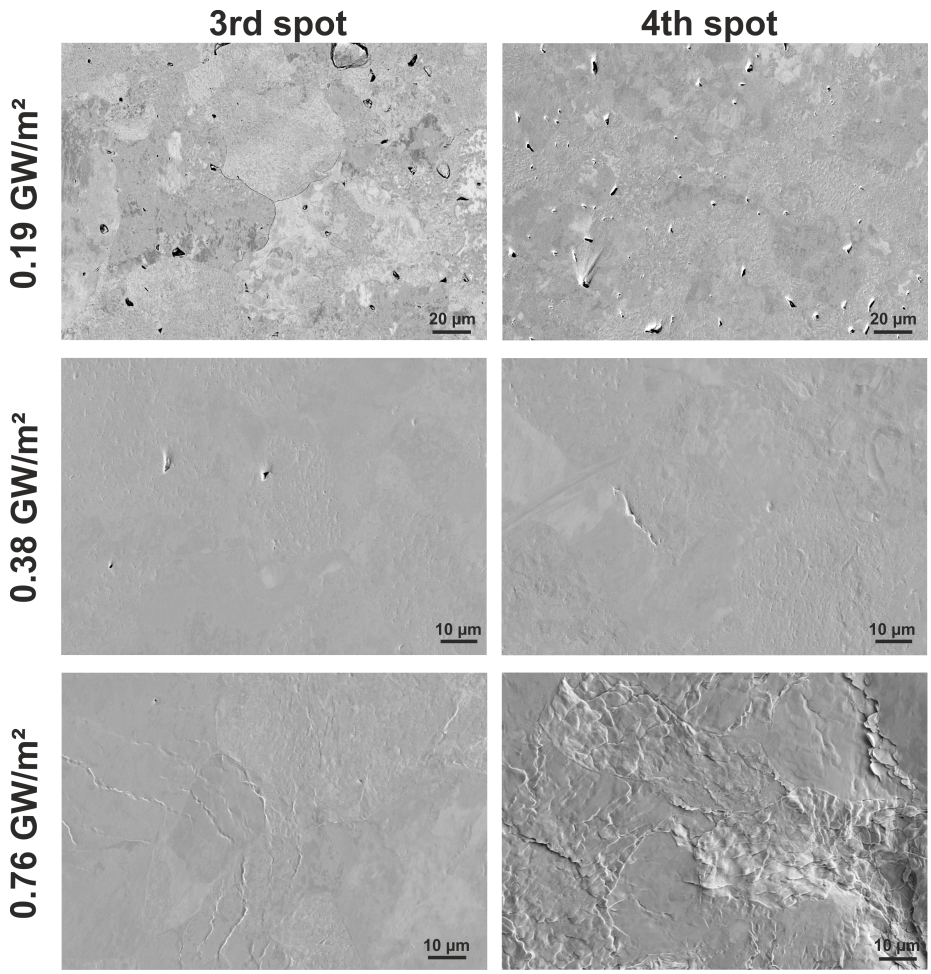


Figure B.7: Comparison of the surface modifications and damage categories of L samples after sequential exposure at 400 °C to deuterium helium plasma and 100 transient events (spot 3) and 1000 transient events (spot 4), respectively.

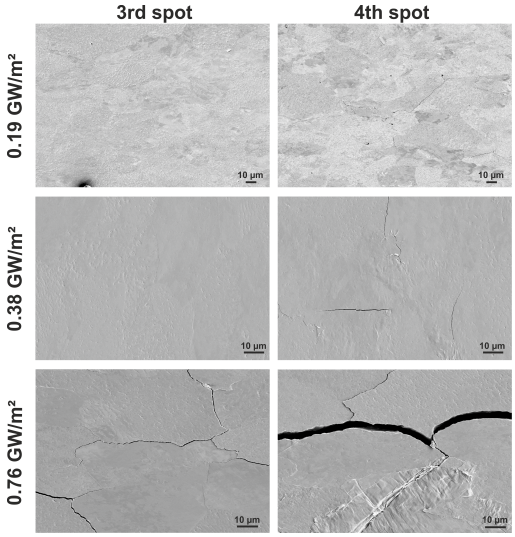


Figure B.8: Comparison of the surface modifications and damage categories of T samples after sequential exposure at 400 °C to deuterium helium plasma and 100 transient events (spot 3) and 1000 transient events (spot 4), respectively.

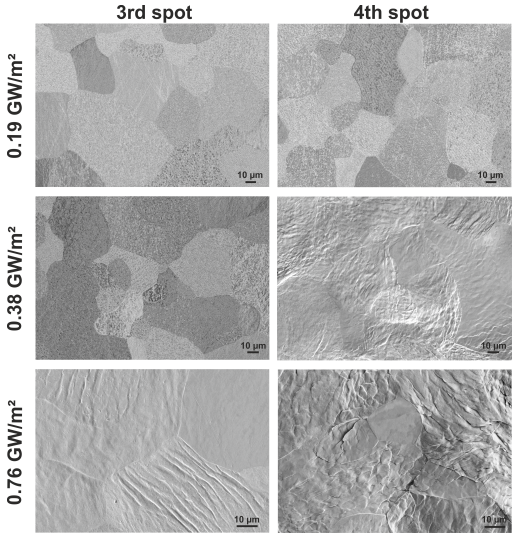


Figure B.9: Comparison of the surface modifications and damage categories of R samples after sequential exposure at 400 °C to deuterium helium plasma and 100 transient events (spot 3) and 1000 transient events (spot 4), respectively.

B.4 Tests with deuterium helium(6 %) plasma at 730 °C

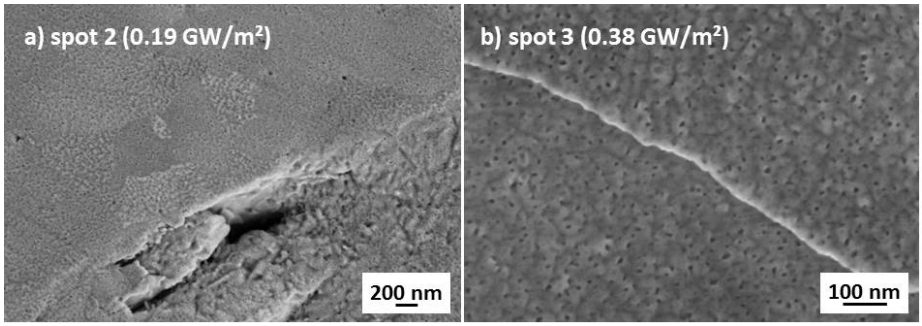


Figure B.10: Image a) depicts the initiation of tungsten fuzz after simultaneous exposure at 0.19 GW/m². The SEM image b) shows also the initiation of fuzz/spongy surface morphology after initial plasma exposure followed by laser loads at 0.38 GW/m².

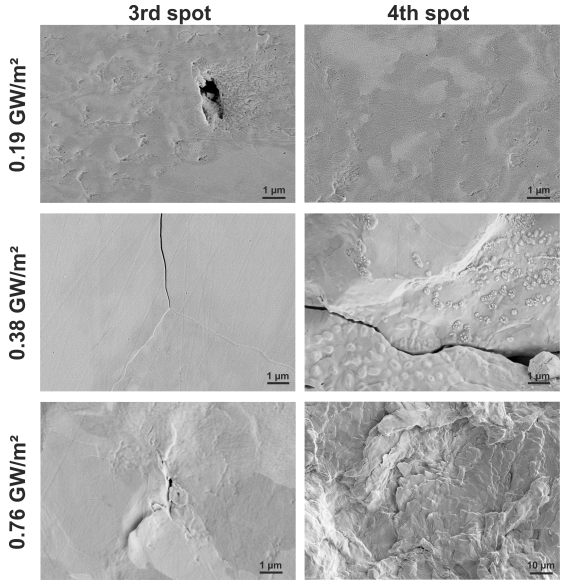


Figure B.11: Comparison of the surface modifications and damage categories of L samples after sequential exposure at 730 °C to deuterium helium plasma and 100 transient events (spot 3) and 1000 transient events (spot 4), respectively.

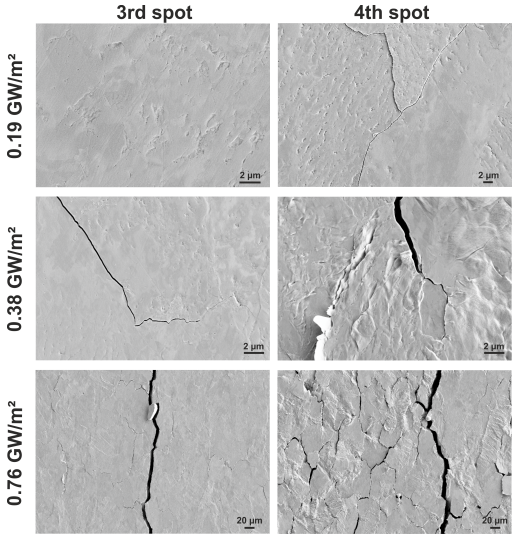


Figure B.12: Comparison of the surface modifications and damage categories of T samples after sequential exposure at 730 °C to deuterium helium plasma and 100 transient events (spot 3) and 1000 transient events (spot 4), respectively.

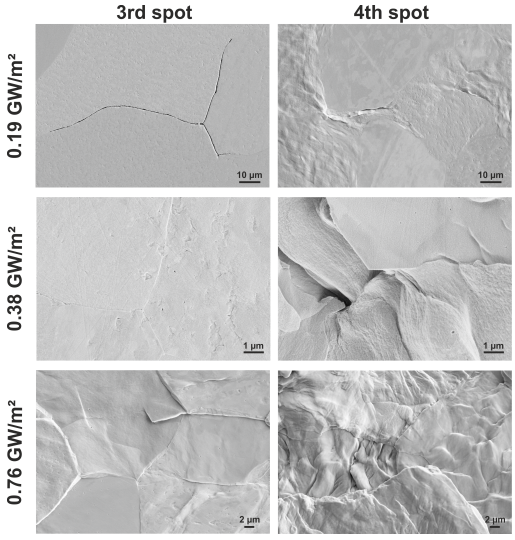


Figure B.13: Comparison of the surface modifications and damage categories of R samples after sequential exposure at 730 °C to deuterium helium plasma and 100 transient events (spot 3) and 1000 transient events (spot 4), respectively.

C Appendix: Detailed measurement results of high pulse number tests

Table C.1: Arithmetic mean roughness R_a in µm for all sample types measured after 10,000 and 100,000 ELM-like events that were presented in subsection 4.5.1.

	R_a [µm]		
sample type	L	T	R
after 10,000 pulses	2.34	1.37	4.16
after 100,000 pulses	36	22	6

Table C.2: Size of the region with microstructural changes for all sample types measured after 10,000 and 100,000 ELM-like events and presented in subsection 4.5.1.

sample type	L	T	R
size of the affected region after 10,000 pulses [µm]	75	95	100
size of the affected region after 100,000 pulses [µm]	480	340	240

Table C.3: Maximum magnitude, measured from the original surface, of the hills and valleys that were generated after 100,000 ELM-like events for all sample types.

sample type	L	T	R
size of the hills [µm]	145	87	53
size of the valleys [µm]	280	193	24

Table C.4: The table provides the size of the layer in nm, in which helium bubbles had formed after 10,000 ELM-like events as well as the maximum and minimum major axis of the bubbles.

sample type	L	T	R
size of layer [nm]	140	50	50
major axis of max. bubbles [nm]	106	30	21
major axis of min. bubbles [nm]	44	< 30	10

Table C.5: The table provides the size of the layer in nm, in which helium bubbles had formed after 100,000 ELM-like events below the loaded area and outside of the loaded area for all tested samples types.

sample type	L	T	R
layer below the exposure spot [nm]	240	290	400
layer outside the exposure spot [nm]	210	140	100

Table C.6: The table provides the values of the maximum and minimum major axis in nm of the helium bubbles that had formed after 100,000 ELM-like events below the loaded area and outside of the loaded area for all tested samples types.

sample type	L	T	R
major axis of max. bubbles below [nm]	110	170	97
major axis of max. bubbles outside [nm]	80	51	30
major axis of min. bubbles below [nm]	40	35	15
major axis of min. bubbles outside [nm]	40	20	< 15

D Appendix: Detailed measurement results of tests on steel

D.1 Melting tests at JUDITH 1

Table D.1: Arithmetic mean roughness R_a in µm measured by laser profilometry of samples exposed in JUDITH 1 presented in subsection 5.1.1.

	R_a [µm]
unloaded	0.03
tests A (1000 pulses)	29.7
tests B (100 pulses)	0.35

D.2 Subsequent sequential and simultaneous tests at PSI-2

Table D.2: Arithmetic mean roughness R_a in µm of preloaded samples of tests A and tests B after exposure at PSI-2 presented in subsection 5.2.1.

preloading	tests A R_a [µm]				tests B R_a [µm]		
sequence	1	2	3	4	1	2	3
0.19 GW/m²	34.2	39.1	37.5	37.3	0.36	0.36	0.38
0.38 GW/m²	33.8	38.2	36.2	34.2	0.53	0.45	0.43
0.66 GW/m²	35.8	32.2	34.9	32.1	1.18	0.66	0.99

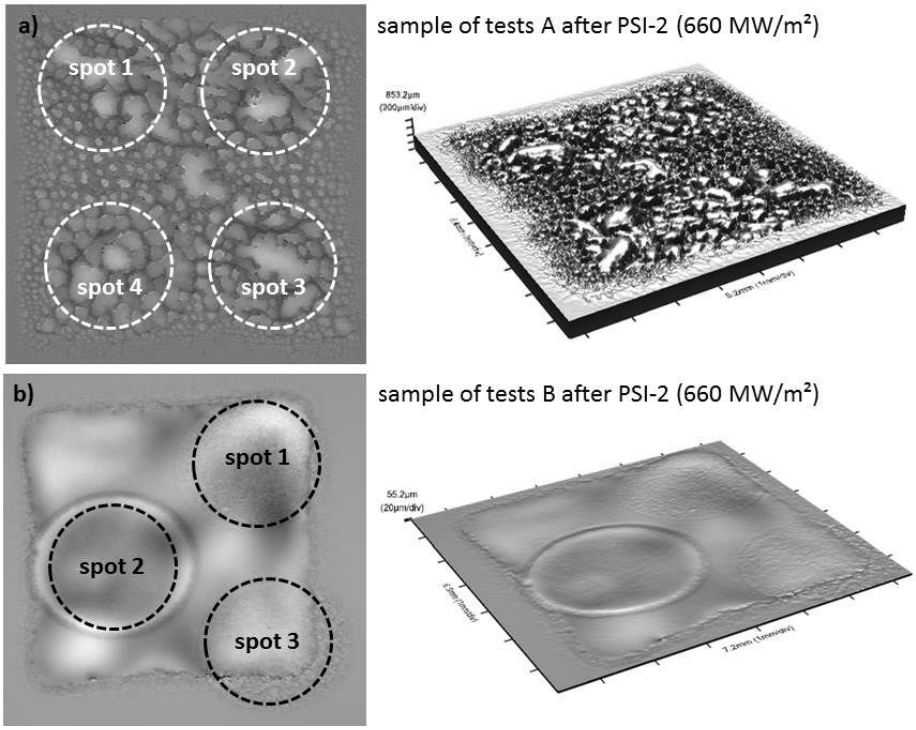


Figure D.1: This figure shows exemplary profilometer scans after sequential and simultaneous exposure at PSI-2. The top row a) shows the results of a preloaded sample of tests A after loading at PSI-2 and the bottom row b) illustrates the results of a preloaded sample of tests B. The single exposure spots are highlighted with striped cicles (spot 1: laser then plasma, spot 2: simultaneous, spot 3: plasma then laser, spot 4: plasma then laser (1000)). The right hand side illustrates a topography scan of the same sample.

Bibliography

[1] ITER Organisation (retrieved 2015); http://www.iter.org. (cited on page: 1, 6, 7, 8, 12 and 14)

[2] M. P. Fewell; The atomic nuclide with the highest mean binding energy; *American Journal of Physics* 63 (7) 653–658 (1995); doi: 10.1119/1.17828; http://ajp.aapt.org/resource/1/ajpias/v63/i7/p653_s1. (cited on page: 3)

[3] T. Mayer-Kuckuk; Kernphysik - Eine Einführung; Teubner, Stuttgart 7. Auflage (April 2002). (cited on page: 3)

[4] F. Ajzenberg-Selove; Energy levels of light nuclei A = 5-10; *Nuclear Physics A* 490 (1) 1–225 (1988); ISSN 0375-9474; doi: 10.1016/0375-9474(88)90124-8; http://www.sciencedirect.com/science/article/pii/0375947488901248. (cited on page: 4)

[5] EUROfusion (retrieved 2014); https://www.euro-fusion.org. (cited on page: 4)

[6] R. A. Gross; Fusion Energy; John Wiley & Sons Inc (1984). (cited on page: 4)

[7] W. M. Stacey; Fusion - An Introduction to the Physics and Technology of Magnetic Confinement Fusion; Wiley-VCH Verlag GmbH & Co. KGaA second, completely revised and enlarged edition Auflage (2010). (cited on page: 5 and 9)

[8] D. Reiter; Introduction to edge plasma modelling; Published online on conference website (retrieved 2012); https://www-amdis.iaea.org/Workshops/ICTP2012/Detlev.Reiter-Lecture2-ICTP-2012-01-26.pdf; Joint ICTP-IAEA Workshop on Fusion Plasma Modelling Using Atomic and Molecular Data. (cited on page: 6)

[9] M. Shimada, A. Costley et al.; Overview of goals and performance of ITER and strategy for plasma–wall interaction investigation; *Journal of Nuclear Materials* 337–339 (0) 808 – 815 (2005); ISSN 0022-3115; doi: http://dx.doi.org/10.1016/j.jnucmat.2004.09.063; http://www.sciencedirect.com/science/article/pii/S0022311504009675; PSI-16. (cited on page: 6)

[10] J. J. Martinell, J. E. Vitela; Thermal stability studies of an experimental nuclear fusion reactor; *Journal of Physics* 511 (2014); doi: 10.1088/1742-6596/511/1/012043. (cited on page: 6)

[11] ITER Physics Expert Group on Confinement and Transport, I. P. E. G. on Confinement Modelling et al.; Chapter2: Plasma confinement and transport; *Nuclear Fusion* 39 (12) 2175 (1999); http://stacks.iop.org/0029-5515/39/i=12/a=302. (cited on page: 7)

[12] H. Zohm; Edge localized modes (ELMs); *Plasma Physics and Controlled Fusion* 38 (2) 105 (1996); http://stacks.iop.org/0741-3335/38/i=2/a=001. (cited on page: 7)

[13] T. Eich, A. Herrmann et al.; Power deposition onto plasma facing components in poloidal divertor tokamaks during type-I {ELMs} and disruptions; *Journal of Nuclear Materials* 337–339 669 – 676 (2005); ISSN 0022-3115; doi: http://dx.doi.org/10.1016/j.jnucmat.2004.09.051; http://www.sciencedirect.com/science/article/pii/S0022311504009390; PSI-16. (cited on page: 7 and 11)

[14] IPP- Max Planck Institut fuer Plasmaphysik (retrieved 2013); http://www.ipp.mpg.de/ippcms/de/index.html. (cited on page: 8)

[15] R. E. Clark, D. H. Reiter; Nuclear Fusion Research - Understanding Plasma-Surface Interactions; Springer (2005). (cited on page: 9 and 11)

[16] R. Pitts, S. Carpentier et al.; A full tungsten divertor for ITER: Physics issues and design status; *Journal of Nuclear Materials* 438, Supplement (0) S48 – S56 (2013); ISSN 0022-3115; doi: http://dx.doi.org/10.1016/j.jnucmat.2013.01.008; http://www.sciencedirect.com/science/article/pii/S0022311513000160; Proceedings of the 20th International Conference on Plasma-Surface Interactions in Controlled Fusion Devices. (cited on page: 9, 11, 14, 16, 40, 82 and 102)

[17] G. S. Was; Fundamentals of Radiation Material Science - Metals and Alloys; Springer (2007). (cited on page: 9)

[18] R. Sakamoto, T. Muroga et al.; Plasma-Surface Interactions in Controlled Fusion Devices Microstructural evolution induced by low energy hydrogen ion irradiation in tungsten; *Journal of Nuclear Materials* 220 819 – 822 (1995); ISSN 0022-3115; doi: http://dx.doi.org/10.1016/0022-3115(94)00622-9; http://www.sciencedirect.com/science/article/pii/0022311594006229. (cited on page: 9 and 53)

[19] A. Haasz, J. Davis et al.; Deuterium retention in tungsten for fusion use; *Journal of Nuclear Materials* 258–263, Part 1 889 – 895 (1998); ISSN 0022-3115; doi: http://dx.doi.org/10.1016/S0022-3115(98)00072-5; http://www.sciencedirect.com/science/article/pii/S0022311598000725. (cited on page: 9)

[20] M. Shimada, R. Pitts et al.; In-vessel dust and tritium control strategy in ITER; *Journal of Nuclear Materials* 438, Supplement (0) S996 – S1000 (2013); ISSN 0022-3115; doi: http://dx.doi.org/10.1016/j.jnucmat.2013.01.217; http://www.sciencedirect.com/science/article/pii/S0022311513002250; Proceedings of the 20th International Conference on Plasma-Surface Interactions in Controlled Fusion Devices. (cited on page: 9)

[21] J. Roth, E. Tsitrone et al.; Recent analysis of key plasma wall interactions issues for ITER; *Journal of Nuclear Materials* 390-391 (0) 1 – 9 (2009); ISSN 0022-3115; doi: 10.1016/j.jnucmat.2009.01.037; http://www.sciencedirect.com/science/article/pii/S0022311509000506. (cited on page: 10, 14 and 40)

[22] M. Wirtz, J. Linke et al.; Influence of high flux hydrogen-plasma exposure on the thermal shock induced crack formation in tungsten; *Journal of Nuclear Materials* 420 (1-3) 218–221 (2012); doi: 10.1016/j.jnucmat.2011.09.035. (cited on page: 10)

[23] A. Huber, G. Sergienko et al.; Impact on the deuterium retention of simultaneous exposure of tungsten to a steady state plasma and transient heat cycling loads; *Physica Scripta* 2016 (T167) 014046 (2016); http://stacks.iop.org/1402-4896/2016/i=T167/a=014046. (cited on page: 10, 32, 44, 64 and 69)

[24] G. de Temmerman, T. Morgan et al.; Effect of high-flux H/He plasma exposure on tungsten damage due to transient heat loads; *Journal of Nuclear Materials* 463 198 – 201 (2015); ISSN 0022-3115; doi: http://dx.doi.org/10.1016/j.jnucmat.2014.09.075; http://www.sciencedirect.com/science/article/pii/S0022311514006758; Plasma-Surface Interactions 21Proceedings of the 21st International Conference on Plasma-Surface Interactions in Controlled Fusion Devices Kanazawa, Japan May 26-30, 2014. (cited on page: 10)

[25] H. Xu, G. Luo et al.; Enhanced modification of tungsten surface by nanostructure formation during high flux deuterium plasma exposure; *Journal of Nuclear Materials* 447 (1–3) 22 – 27 (2014); ISSN 0022-3115; doi: http://dx.doi.org/10.1016/j.jnucmat.2013.12.010; http://www.sciencedirect.com/science/article/pii/S0022311513012968. (cited on page: 10)

[26] J. Yu, M. Baldwin et al.; Transient heating effects on tungsten: Ablation of Be layers and enhanced fuzz growth; *Jour-*

nal of Nuclear Materials 463 299 – 302 (2015); ISSN 0022-3115; doi: http://dx.doi.org/10.1016/j.jnucmat.2014.10.035; http://www.sciencedirect.com/science/article/pii/S0022311514007193; Plasma-Surface Interactions 21Proceedings of the 21st International Conference on Plasma-Surface Interactions in Controlled Fusion Devices Kanazawa, Japan May 26-30, 2014. (cited on page: 10)

[27] V. Barabash, G. Federici et al.; Material/plasma surface interaction issues following neutron damage; *Journal of Nuclear Materials* 313–316 (0) 42 – 51 (2003); ISSN 0022-3115; doi: http://dx.doi.org/10.1016/S0022-3115(02)01330-2; http://www.sciencedirect.com/science/article/pii/S0022311502013302; Plasma-Surface Interactions in Controlled Fusion Devices 15. (cited on page: 10 and 16)

[28] J. Linke; High heat flux performance of plasma facing components under service conditions in future fusion reactors; *Transactions of Fusion Science and Technology* 49 455–464 (2006); http://www.carolusmagnus.net/papers/2005/docs/linke_plasma_facing_materials.pdf. (cited on page: 11, 13 and 14)

[29] A. Loarte, G. Saibene et al.; Characteristics of type I ELM energy and particle losses in existing devices and their extrapolation to ITER; *Plasma Physics and Controlled Fusion* 45 1549–1569 (2003). (cited on page: 11)

[30] A. Leonard, A. Herrmann et al.; The impact of ELMs on the ITER divertor; *Journal of Nuclear Materials* 266–269 (0) 109 – 117 (1999); ISSN 0022-3115; doi: http://dx.doi.org/10.1016/S0022-3115(98)00522-4; http://www.sciencedirect.com/science/article/pii/S0022311598005224. (cited on page: 11)

[31] M. Wirtz, J. Linke et al.; Thermal shock behaviour of tungsten after high flux H-plasma loading; *Journal of Nuclear Materials* (2011). (cited on page: 12)

[32] M. Merola, G. Vieider et al.; European achievements for ITER high heat flux components; *Fusion Engineering and Design* 56–57 (0) 173 – 178 (2001); ISSN 0920-3796; doi: http://dx.doi.org/10.1016/S0920-3796(01)00253-8; http://www.sciencedirect.com/science/article/pii/S0920379601002538. (cited on page: 12)

[33] J. Linke, P. Lorenzetto et al.; EU development of high heat flux components; *Fusion Science and Technology* 47 678–658 (2005). (cited on page: 12)

[34] O. Gruber, K. Lackner et al.; Vertical Displacement Events and Halo Currents; *Plasma Phys. Controls* 35 B191–B204 (1993). (cited on page: 12)

[35] A. Hassanein, T. Sizyuk et al.; Vertical displacement events: A serious concern in future ITER operation; *Fusion Engineering and Design* 83 1020–1024 (2008). (cited on page: 12)

[36] A. Hassanein, G. Federici et al.; Materials effects and design implications of disruptions and off-normal events in {ITER1}; *Fusion Engineering and Design* 39–40 (0) 201 – 210 (1998); ISSN 0920-3796; doi: http://dx.doi.org/10.1016/S0920-3796(97)00135-X; http://www.sciencedirect.com/science/article/pii/S092037969700135X. (cited on page: 12)

[37] U. Kruezi, M. Lehnen et al.; Massive gas injections in {JET} – Impact on wall conditions; *Journal of Nuclear Materials* 415 (1, Supplement) S828 – S831 (2011); ISSN 0022-3115; doi: http://dx.doi.org/10.1016/j.jnucmat.2010.11.069; http://www.sciencedirect.com/science/article/pii/S0022311510007774; Proceedings of the 19th International Conference on Plasma-Surface Interactions in Controlled Fusion. (cited on page: 12)

[38] M. Lehnen, A. Alonso et al.; Disruption mitigation by massive gas injection in JET; *Nuclear Fusion* 51 (12) 123010 (2011); http://stacks.iop.org/0029-5515/51/i=12/a=123010. (cited on page: 12)

[39] M. Merola, F. Escourbiac et al.; Overview and status of ITER internal components; *Fusion Engineering and Design* 89 (7–8) 890 – 895 (2014); ISSN 0920-3796; doi: http://dx.doi.org/10.1016/j.fusengdes.2014.01.055; http://www.sciencedirect.com/science/article/pii/S0920379614000568; Proceedings of the 11th International Symposium on Fusion Nuclear Technology-11 (ISFNT-11) Barcelona, Spain, 15-20 September, 2013. (cited on page: 13 and 16)

[40] H. Bolt, V. Barabash et al.; Plasma facing and high heat flux materials – needs for ITER and beyond; *Journal of Nuclear Materials* 307–311, Part 1 (0) 43 – 52 (2002); ISSN 0022-3115; doi: http://dx.doi.org/10.1016/S0022-3115(02)01175-3; http://www.sciencedirect.com/science/article/pii/S0022311502011753. (cited on page: 13, 14, 37, 101 and 112)

[41] H. Bolt, V. Barabash et al.; Materials for the plasma-facing components of fusion reactors; *Journal of Nuclear Materials* 29–333 66–73 (2004). (cited on page: 13, 14 and 15)

[42] V. Barabash, M. Akiba et al.; Selection, development and characterisation of plasma facing materials for ITER; *Journal of Nuclear Materials* 233–237, Part 1 718 – 723 (1996); ISSN 0022-

3115; doi: http://dx.doi.org/10.1016/S0022-3115(96)00323-6; http://www.sciencedirect.com/science/article/pii/S0022311596003236. (cited on page: 13, 15 and 16)

[43] J. P. Gunn, S. Carpentier-Chouchana et al.; Surface Heat Load Modelling on Tungsten Monoblocks in the ITER Divertor; *Proceedings of the 25th IAEA Fusion Energy Conference, Russia* FIP/1-2 499 (2014). (cited on page: 14)

[44] G. Pintsuk; 4.17 - Tungsten as a Plasma-Facing Material; In R. J. Konings, editor, Comprehensive Nuclear Materials pp. 551 – 581. Elsevier, Oxford (2012); ISBN 978-0-08-056033-5; doi: http://dx.doi.org/10.1016/B978-0-08-056033-5.00118-X; http://www.sciencedirect.com/science/article/pii/B978008056033500118X. (cited on page: 14, 43, 44, 52, 64, 70, 78, 79 and 80)

[45] D. Stork, P. Agostini et al.; Materials R&D for a timely DEMO: Key findings and recommendations of the EU Roadmap Materials Assessment Group; *Fusion Engineering and Design* (0) – (2014); ISSN 0920-3796; doi: http://dx.doi.org/10.1016/j.fusengdes.2013.11.007; http://www.sciencedirect.com/science/article/pii/S0920379613007059. (cited on page: 15, 16 and 101)

[46] R. Lässer, N. Baluc et al.; Structural materials for DEMO: The EU development, strategy, testing and modelling; *Fusion Engineering and Design* 82 (5–14) 511 – 520 (2007); ISSN 0920-3796; doi: http://dx.doi.org/10.1016/j.fusengdes.2007.06.031; http://www.sciencedirect.com/science/article/pii/S0920379607003377; <ce:title>Proceedings of the 24th Symposium on Fusion Technology</ce:title> <ce:subtitle>SOFT-24</ce:subtitle>. (cited on page: 15, 16 and 17)

[47] V. Philipps; Tungsten as material for plasma-facing components in fusion devices; *Journal of Nuclear Materials* 415 (1, Supplement) S2 – S9 (2011); ISSN 0022-3115; doi: 10.1016/j.jnucmat.2011.01.110; http://www.sciencedirect.com/science/article/pii/S0022311511001589; Proceedings of the 19th International Conference on Plasma-Surface Interactions in Controlled Fusion. (cited on page: 15 and 16)

[48] J. Linke, M. Akiba et al.; Performance of beryllium, carbon, and tungsten under intense thermal fluxes; *Journal of Nuclear Materials* 241–243 (0) 1210–1216 (1997); ISSN 0022-3115; doi: 10.1016/S0022-3115(97)80222-X; http://www.sciencedirect.com/science/article/pii/S002231159780222X. (cited on page: 15 and 16)

[49] M. Rieth, S. Dudarev et al.; Recent progress in research on tungsten materials for nuclear fusion applications in Europe; *Journal*

of Nuclear Materials 432 (1–3) 482 – 500 (2013); ISSN 0022-3115; doi: http://dx.doi.org/10.1016/j.jnucmat.2012.08.018; http://www.sciencedirect.com/science/article/pii/S0022311512004278. (cited on page: 15 and 37)

[50] R. Lindau, A. Möslang et al.; Present development status of EUROFER and ODS-EUROFER for application in blanket concepts; *Fusion Engineering and Design* 75–79 (0) 989 – 996 (2005); ISSN 0920-3796; doi: http://dx.doi.org/10.1016/j.fusengdes.2005.06.186; http://www.sciencedirect.com/science/article/pii/S0920379605003534; Proceedings of the 23rd Symposium of Fusion Technology {SOFT} 23. (cited on page: 15 and 24)

[51] N. Baluc, K. Abe et al.; Status of R&D activities on materials for fusion power reactors; *Nuclear Fusion* 47 (10) S696 (2007); http://stacks.iop.org/0029-5515/47/i=10/a=S18. (cited on page: 15, 17, 25 and 101)

[52] L. Singheiser, T. Hirai et al.; Plasma-facing materials for thermo-nuclear fusion devices; *Transactions of The Indian Institute of Metals* 62 (2) 123–128 (2009). (cited on page: 16)

[53] D. Maisonnier, I. Cook et al.; The European power plant conceptual study; *Fusion Engineering and Design* 75–79 1173 – 1179 (2005); ISSN 0920-3796; doi: http://dx.doi.org/10.1016/j.fusengdes.2005.06.095; http://www.sciencedirect.com/science/article/pii/S0920379605002218; Proceedings of the 23rd Symposium of Fusion TechnologySOFT 23. (cited on page: 16 and 24)

[54] K. Yakushiji, H. T. Lee et al.; Influence of helium on deuterium retention in reduced activation ferritic martensitic steel (F82H) under simultaneous deuterium and helium irradiation; *Physica Scripta* 2016 (T167) 014067 (2016); http://stacks.iop.org/1402-4896/2016/i=T167/a=014067. (cited on page: 16 and 24)

[55] V. Mukhovatov, M. Shimada et al.; Chapter 9: ITER contributions for Demo plasma development; *Nuclear Fusion* 47 (6) S404 (2007); http://stacks.iop.org/0029-5515/47/i=6/a=S09. (cited on page: 16)

[56] J. Brooks, J. Allain et al.; Plasma–surface interaction issues of an all-metal ITER; *Nuclear Fusion* 49 (3) 035007 (2009); http://stacks.iop.org/0029-5515/49/i=3/a=035007. (cited on page: 16)

[57] M. Sugihara, S. Putvinski et al.; Disruption Impacts and Their Mitigation Target Values for ITER Operation and Machine Protection; *Proceedings of the 24th IAEA Fusion Energy Conference* (ITR/P1-14) (2013); http://www-naweb.iaea.org/napc/physics/FEC/FEC2012/html/proceedings.pdf. (cited on page: 18 and 101)

[58] N. Klimov, J. Linke et al.; Stainless steel performance under ITER-relevant mitigated disruption photonic heat loads; *Journal of Nuclear Materials* 438, Supplement (0) S241 – S245 (2013); ISSN 0022-3115; doi: http://dx.doi.org/10.1016/j.jnucmat.2013.01.036; http://www.sciencedirect.com/science/article/pii/S0022311513000445; <ce:title id=>Proceedings of the 20th International Conference on Plasma-Surface Interactions in Controlled Fusion Devices</ce:title>. (cited on page: 18 and 103)

[59] E. Lassner, W.-D. Schubert; Tungsten: Properties, Chemistry, Technology of the Element, Alloys, and Chemical Compounds; Kluwer Academic / Plenum Plublishers, New York (1999); ISBN 978-0-306-45053-2. (cited on page: 21, 22 and 59)

[60] Plansee Östereich (retrieved 2013); http://www.plansee.com. (cited on page: 22)

[61] G. Pintsuk, A. Prokhodtseva et al.; Thermal shock characterization of tungsten deformed in two orthogonal directions; *Journal of Nuclear Materials* 417 481–486 (2011). (cited on page: 22, 37, 38, 40, 58, 78 and 112)

[62] I. Steudel; Einflüsse unterschiedlicher Belastungsarten auf das Thermoschockverhalten von Wolfram; Diploma Thesis - Rheinische Friedrich-Wilhelms-Universität Bonn (October 2013). (cited on page: 23, 37, 38, 40 and 58)

[63] O. M. Wirtz; Thermal shock behaviour of different tungsten grades under varying cionditions; Doktorarbeit (2012). (cited on page: 23, 29, 30 and 39)

[64] K. Ehrlich; Materials research towards a fusion reactor; *Fusion Engineering and Design* 56–57 71 – 82 (2001); ISSN 0920-3796; doi: http://dx.doi.org/10.1016/S0920-3796(01)00236-8; http://www.sciencedirect.com/science/article/pii/S0920379601002368. (cited on page: 24)

[65] W. Yan, W. Wang et al.; 9-12Cr Heat-Resistant Steels; Engineering Materials. Springer International Publishing 1. Auflage (2015); doi: 10.1007/978-3-319-14839-7. (cited on page: 24)

[66] BGH; Boschgotthardshütte Edelstahl Freital GmbH (retrieved 2016); http://www.bgh.de/de/. (cited on page: 24 and 25)

[67] R. Duwe, W. Kuehnlein et al.; The new Electron Beam Facility for Materials Testing in Hot Cells; *Fusion Technology* pp. 356–358 (1995). (cited on page: 27 and 29)

[68] M. Rödig, E. Ishitsuka et al.; High heat flux performance of neutron irradiated plasma facing components; *Journal of Nuclear*

Materials 307–311, Part 1 (0) 53 – 59 (2002); ISSN 0022-3115; doi: http://dx.doi.org/10.1016/S0022-3115(02)01030-9; http://www.sciencedirect.com/science/article/pii/S0022311502010309. (cited on page: 27 and 29)

[69] T. Loewenhoff; Combined steady state and high cycle transient heat load simulation with the electron beam facility JUDITH 2; Doktorarbeit Rheinisch-Westfaelische Technische Hochschule Aachen (2012). (cited on page: 29)

[70] E. Wessel; personal communication (2009). (cited on page: 30)

[71] S. Schiller, U. Heisig et al.; Elektronenstrahltechnologie; Wissenschaftliche Verlagsgesellschaft Stuttgart, Lizenz des Verlag Technik, VEB Berlin (1977). (cited on page: 30)

[72] S. Flügge; Handbuch der Physik, Band XXI; Springer-Verlag (1956). (cited on page: 30)

[73] A. Kreter, C. Brandt et al.; Linear Plasma Device PSI-2 for Plasma-Material Interaction Studies; *Fusion Science and Technology* 68 (1) 8–14 (July 2015); doi: dx.doi.org/10.13182/FST14-906. (cited on page: 30 and 31)

[74] M. Wirtz, S. Bardin et al.; Impact of combined hydrogen plasma and transient heat loads on the performance of tungsten as plasma facing material; *Nuclear Fusion* 55 (12) 123017 (2015); http://stacks.iop.org/0029-5515/55/i=12/a=123017. (cited on page: 33)

[75] G. Federici, A. Zhitlukhin et al.; Effects of ELMs and disruptions on ITER divertor armour materials; *Journal of Nuclear Materials* 337–339 684 – 690 (2005); ISSN 0022-3115; doi: http://dx.doi.org/10.1016/j.jnucmat.2004.10.149; http://www.sciencedirect.com/science/article/pii/S0022311504009353; PSI-16. (cited on page: 37)

[76] ITER Physics Basis Editors and ITER Physics Expert Group Chairs, Co-Chairs et al.; Chapter 1 - Overview and summary; *Nuclear Fusion* 39 (12) 2137 (1999); http://stacks.iop.org/0029-5515/39/i=12/a=301. (cited on page: 37)

[77] M. Wirtz, G. Cempura et al.; Thermal shock response of deformed and recrystallised tungsten; *Fusion Engineering and Design* (2013); ISSN 0920-3796; doi: http://dx.doi.org/10.1016/j.fusengdes.2013.05.077; http://www.sciencedirect.com/science/article/pii/S0920379613005176. (cited on page: 40, 48 and 50)

[78] M. Wirtz, J. Linke et al.; Comparison of thermal shock damages induced by different simulation methods on tungsten; *Journal of Nuclear Materials* 438, Supplement (0) S833 – S836 (2013); ISSN 0022-3115; doi: http://dx.doi.org/10.1016/j.jnucmat.2013.01.180; http://www.sciencedirect.com/science/article/pii/S0022311513001888. (cited on page: 40)

[79] M. Vogel, A. Terra et al.; PSI-2 Experiment Build; power point file (2015). (cited on page: 41 and 116)

[80] H. Xu, Y. Zhang et al.; Observations of orientation dependence of surface morphology in tungsten implanted by low energy and high flux D plasma; *Journal of Nuclear Materials* 443 (1–3) 452 – 457 (2013); ISSN 0022-3115; doi: http://dx.doi.org/10.1016/j.jnucmat.2013.07.062; http://www.sciencedirect.com/science/article/pii/S0022311513009501. (cited on page: 45)

[81] M. Miyamoto, D. Nishijima et al.; Observations of suppressed retention and blistering for tungsten exposed to deuterium–helium mixture plasmas; *Nuclear Fusion* 49 (6) 065035 (2009); http://stacks.iop.org/0029-5515/49/i=6/a=065035. (cited on page: 45)

[82] M. Poon, R. Macaulay-Newcombe et al.; Flux dependence of deuterium retention in single crystal tungsten; *Journal of Nuclear Materials* 307–311, Part 1 723 – 728 (2002); ISSN 0022-3115; doi: http://dx.doi.org/10.1016/S0022-3115(02)00946-7; http://www.sciencedirect.com/science/article/pii/S0022311502009467. (cited on page: 46)

[83] F. J. Humphreys, M. Hatherly; Recrystallization and Related Annealing Phenomena; Pergamon 2. Auflage (2003). (cited on page: 48)

[84] W. Shu, K. Isobe et al.; Temperature dependence of blistering and deuterium retention in tungsten exposed to high-flux and low-energy deuterium plasma; *Fusion Engineering and Design* 83 (7–9) 1044 – 1048 (2008); ISSN 0920-3796; doi: http://dx.doi.org/10.1016/j.fusengdes.2008.05.006; http://www.sciencedirect.com/science/article/pii/S0920379608001038; Proceedings of the Eight International Symposium of Fusion Nuclear Technology ISFNT-8. (cited on page: 50)

[85] C. García-Rosales, P. Franzen et al.; Re-emission and thermal desorption of deuterium from plasma sprayed tungsten coatings for application in ASDEX-upgrade; *Journal of Nuclear Materials* 233 803 – 808 (1996); ISSN 0022-3115; doi: http://dx.doi.org/10.1016/S0022-3115(96)00185-7; http://www.sciencedirect.com/science/article/pii/S0022311596001857. (cited on page: 53)

[86] O. Ogorodnikova, J. Roth et al.; Deuterium retention in tungsten in dependence of the surface conditions; *Journal of Nuclear Materials* 313–316 469

– 477 (2003); ISSN 0022-3115; doi: http://dx.doi.org/10.1016/S0022-3115(02)01375-2; http://www.sciencedirect.com/science/article/pii/S0022311502013752; Plasma-Surface Interactions in Controlled Fusion Devices 15. (cited on page: 53)

[87] G.-N. Luo, W. Shu et al.; Influence of blistering on deuterium retention in tungsten irradiated by high flux deuterium 10–100 eV plasmas; *Fusion Engineering and Design* 81 (8–14) 957 – 962 (2006); ISSN 0920-3796; doi: http://dx.doi.org/10.1016/j.fusengdes.2005.09.023; http://www.sciencedirect.com/science/article/pii/S0920379605006125; Proceedings of the Seventh International Symposium on Fusion Nuclear Technology ISFNT-7. (cited on page: 53)

[88] R. Causey, R. Doerner et al.; Defects in tungsten responsible for molecular hydrogen isotope retention after exposure to low energy plasmas; *Journal of Nuclear Materials* 390–391 717 – 720 (2009); ISSN 0022-3115; doi: http://dx.doi.org/10.1016/j.jnucmat.2009.01.300; http://www.sciencedirect.com/science/article/pii/S0022311509002177; Proceedings of the 18th International Conference on Plasma-Surface Interactions in Controlled Fusion Devices. (cited on page: 53)

[89] B. Cipiti, G. Kulcinski; Helium and deuterium implantation in tungsten at elevated temperatures; *Journal of Nuclear Materials* 347 (3) 298 – 306 (2005); ISSN 0022-3115; doi: http://dx.doi.org/10.1016/j.jnucmat.2005.08.009; http://www.sciencedirect.com/science/article/pii/S0022311505004113; Laser Fusion Materials. (cited on page: 53)

[90] H. Eleveld, A. van Veen; Fusion Reactor Materials Void growth and thermal desorption of deuterium from voids in tungsten; *Journal of Nuclear Materials* 212 1421 – 1425 (1994); ISSN 0022-3115; doi: http://dx.doi.org/10.1016/0022-3115(94)91062-6; http://www.sciencedirect.com/science/article/pii/0022311594910626. (cited on page: 55)

[91] Y. Ueda, H. Peng et al.; Helium effects on tungsten surface morphology and deuterium retention; *Journal of Nuclear Materials* 442 (1–3, Supplement 1) S267 – S272 (2013); ISSN 0022-3115; doi: http://dx.doi.org/10.1016/j.jnucmat.2012.10.023; http://www.sciencedirect.com/science/article/pii/S0022311512005582; 15th International Conference on Fusion Reactor Materials. (cited on page: 62 and 64)

[92] M. Wirtz, M. Berger et al.; Influence of helium induced nanostructures on the thermal shock performance of tungsten; *Nuclear Materials and Energy* pp. – (2016); ISSN 2352-1791; doi: http://dx.doi.org/10.1016/j.nme.2016.07.002; http://www.sciencedirect.com/science/article/pii/S2352179115301198. (cited on page: 68, 69 and 72)

[93] S. Kajita, W. Sakaguchi et al.; Formation process of tungsten nanostructure by the exposure to helium plasma under fusion relevant plasma conditions; *Nuclear Fusion* 49 (9) 095005 (2009); http://stacks.iop.org/0029-5515/49/i=9/a=095005. (cited on page: 69)

[94] N. Yoshida, H. Iwakiri et al.; Impact of low energy helium irradiation on plasma facing metals; *Journal of Nuclear Materials* 337–339 (0) 946 – 950 (2005); ISSN 0022-3115; doi: http://dx.doi.org/10.1016/j.jnucmat.2004.10.162; http://www.sciencedirect.com/science/article/pii/S0022311504009316; PSI-16. (cited on page: 72)

[95] Y. Ueda, J. Coenen et al.; Research status and issues of tungsten plasma facing materials for ITER and beyond; *Fusion Engineering and Design* 89 (7–8) 901 – 906 (2014); ISSN 0920-3796; doi: http://dx.doi.org/10.1016/j.fusengdes.2014.02.078; http://www.sciencedirect.com/science/article/pii/S0920379614001859; Proceedings of the 11th International Symposium on Fusion Nuclear Technology ISFNT-11. (cited on page: 79)

[96] A. Loarte, G. Saibene et al.; Transient heat loads in current fusion experiments, extrapolation to ITER and consequences for its operation; *Physica Scripta* 2007 (T128) 222 (2007); http://stacks.iop.org/1402-4896/2007/i=T128/a=043. (cited on page: 82)

[97] Y. Igitkhanov, B. Bazylev et al.; Applicability of tungsten/EUROFER blanket module for the DEMO first wall; *Journal of Nuclear Materials* 438, Supplement S440 – S444 (2013); ISSN 0022-3115; doi: http://dx.doi.org/10.1016/j.jnucmat.2013.01.089; http://www.sciencedirect.com/science/article/pii/S0022311513000974; Proceedings of the 20th International Conference on Plasma-Surface Interactions in Controlled Fusion Devices. (cited on page: 101)

[98] I. Steudel, A. Huber et al.; Melt-layer formation on PFMs and the consequences for the material performance; *Nuclear Materials and Energy* pp. – (available online 4 August 2016); ISSN 2352-1791; doi: http://dx.doi.org/10.1016/j.nme.2016.08.002; http://www.sciencedirect.com/science/article/pii/S2352179115301150; In Press, Corrected Proof. (cited on page: 101)

[99] B. Spilker, J. Linke et al.; Investigation of damages induced by ITER-relevant heat loads during massive gas injections on Beryllium; *Nuclear Materials and Energy* pp. – (2016); ISSN 2352-1791; doi: http://dx.doi.org/10.1016/j.nme.2016.06.006; http://www.sciencedirect.com/science/article/pii/S2352179115301149. (cited on page: 102)

[100] T. Loewenhoff, J. Linke et al.; Tungsten and CFC degradation under combined high cycle transient and steady state heat loads; *Fusion Engineering and Design* 87 (7–8) 1201 – 1205 (2012); ISSN 0920-3796; doi: http://dx.doi.org/10.1016/j.fusengdes.2012.02.106; http://www.sciencedirect.com/science/article/pii/S0920379612001809; Tenth International Symposium on Fusion Nuclear Technology (ISFNT-10). (cited on page: 110)

Danksagung

Ich möchte mich bei meinem Doktorvater Prof. Dr. L. Singheiser für die Möglichkeit bedanken, dass ich diese Arbeit am Institut für Energie- und Klimaforschung (IEK-2) durchführen und beenden konnte.

Des Weiteren bedanke ich mich herzlich bei Prof. Dr. Bernhard Unterberg für die bereitwillige Übernahme des Koreferates sowie den stets herzlichen und freundlichen Umgang und die netten Gespräche.

Mein Dank gilt auch Dr. Jochen Linke, dessen Bürotür immer offen stand für alle großen und kleinen Fragen/Probleme, der mit seinem umfangreichen Wissen, konstruktiver Kritik aber auch Lob, Herzlichkeit und Vertrauen eine harmonische Arbeitsatmosphäre geschaffen hat, innerhalb derer ich mich weiterentwickeln konnte und sehr wohl gefühlt habe. Auch die geselligen Zusammentreffen außerhalb der Arbeitsumgebung werden mir stets in positiver Erinnerung bleiben.

Ein großer und herzlicher Dank gilt meinem wissenschaftlichen Betreuer Dr. Marius Wirtz. Seine freundschaftliche, kompetente und ermutigende Art gestaltete die Zusammenarbeit überaus angenehm und unkompliziert und ließ Raum für eigene Ideen. Sein fundiertes Wissen stellte er bereitwillig zur Verfügung und nahm sich immer Zeit für Diskussionen und Gedankenaustausche. Ich habe mich sehr gut betreut gefühlt und hätte es mir nicht besser wünschen können.

Weiterhin möchte ich mich ganz herzlich bei Michael Vogel und Sebastian Kraus für die kompetente Unterstützung und Hilfe bei der Durchführung meiner Experimente an PSI-2 bedanken sowie für ihre sympathische Art und all die netten und lustigen Gespräche, die die Wartezeiten während der Experimente zwar nicht verkürzt aber definitiv erträglicher gemacht haben.

Auch Dr. A. Kreter, Dr. A. Huber und Dr. G. Sergienko gilt mein Dank für Ihre freundliche und kompetente Unterstützung und die nette Zusammenarbeit an PSI-2.

Für die gute Zusammenarbeit bei der Durchführung der Elektronenstrahlexperimente möchte ich mich bei Michael Hühnerbein und Matthias Diederichs bedanken.

Auch den Mitarbeitern des IEK-2 gilt mein Dank. Hier möchte ich mich besonders bei Dr. E. Wessel, D. Grüner, V. Gutzeit, J. Bartsch und D. Esser für ihre Hilfe bei den REM und FIB Untersuchungen sowie der Metallografie sehr, sehr vieler Wolframproben bedanken. Gerade auch in der Endphase der Doktorarbeit haben sie mich sehr unterstützt, damit ich meinen Zeitplan einhalten konnte. Dafür noch einmal meinen herzlichen Dank. G. Knauf und G. Böling danke ich für die Unterstützung bei der Probenfertigung. K. Leipertz möchte ich für die schnelle und unkomplizierte Art bei der Bearbeitung aller Druckaufträge danken. Außerdem gilt mein Dank P. Joecken und M. Hucko, die in allen IT-Angelegenheiten immer hilfreich zur Stelle waren.

Weiterer Dank gilt meinen Kollegen Dr. Thorsten Loewenhoff und Dr. Gerald Pintsuk, die immer ein offenes Ohr für alle Fragen, Probleme und Ideen hatten, stets ihre Erfahrung und ihr Wissen geteilt haben und immer freundlich und kollegial waren. Ein besonderer Dank geht an Gerald für die gewinnbringenden Gespräche und Anmerkungen gerade in der Endphase der Arbeit. Dadurch habe ich gewisse Ergebnisse aus einem anderen Blickwinkel betrachtet, was mich zu weiteren Erkenntnissen geführt hat. Speziell bedanken möchte ich mich bei Benjamin Spilker, er war nicht nur der beste Bürokollege, den man sich wünschen kann, sondern auch uneingeschränkt hilfsbereit und liebenswürdig. Außerdem danke ich Dr. Juan Du, Dr. Thomas Weber, Jennifer Lopez und Matthias Berger, die ebenso ihren wertvollen Beitrag zum angenehmen, produktiven und lustigen Arbeitsklima geleistet haben.

Abschließend möchte ich mich bei meiner Familie bedanken, die immer an mich geglaubt und mich bekräftigt hat. Besonderer Dank gilt hier meinem Onkel Holger Siedel, der immer reges Interesse an meiner Arbeit gezeigt hat, uneingeschränkt an mich und meine Fähigkeiten geglaubt hat und immer da war, wenn ich ihn brauchte. Du bist großartig und unersetzbar. Meinen Freunden möchte ich für ihren Zuspruch danken und dafür, dass sie auch Tunnelblick und Stimmungsschwankungen geduldig ertragen haben. Am Schluss gilt mein spezieller Dank meinem Puppi, der leider viel zu oft das Ventil für aufgestaute Sorgen, Ängste, Stress und Zweifel war. Danke, dass du bist wie du bist, danke für halbvolle Gläser, danke für Realitätsabgleiche, danke für den Wahnsinn und vor allem danke für deine Liebe.

Band / Volume 357
Korrosion metallischer Bipolarplatten in Hochtemperatur-Polymerelektrolyt-Brennstoffzellen
V. Weißbecker (2017), viii, 194 pp
ISBN: 978-3-95806-205-4

Band / Volume 358
Realistic Bandwidth Estimation in the Theoretically Predicted Radionuclide Inventory of PWR-UO2 Spent Fuel Derived from Reactor Design and Operating Data
I. Fast (2017), XI, 129 pp
ISBN: 978-3-95806-206-1

Band / Volume 359
Light Trapping by Light Treatment
Direct Laser Interference Patterning
For the Texturing of Front Contacts in Thin-Film Silicon Solar Cells
T. Dyck (2017), vi, 172, XI pp
ISBN: 978-3-95806-208-5

Band / Volume 360
Interface and Topography Optimization for Thin-Film Silicon Solar Cells with Doped Microcrystalline Silicon Oxide Layers
C. Zhang (2017), VII, 156 pp
ISBN: 978-3-95806-209-2

Band / Volume 361
Calibration and large-scale inversion of multi-configuration electromagnetic induction data for vadose zone characterization
C. von Hebel (2017), ix, 123 pp
ISBN: 978-3-95806-210-8

Band / Volume 362
Process-based modelling of regional water and energy fluxes taking into account measured neutron intensities by cosmic-ray probes
R. Baatz (2017), xvi, 135 pp
ISBN: 978-3-95806-211-5

Band / Volume 363
Quantitative Analyse der Lithiumverteilung in Kathoden- und Elektrolyt-Dünnschichten für Festkörperbatterien
C. Dellen (2017), vi, 161 pp
ISBN: 978-3-95806-214-6

Band / Volume 364
Intragruppentrennung Seltener Erden mittels neuer phosphororganischer Liganden
S. Hadić (2017), VIII, 164 pp
ISBN: 978-3-95806-215-3

Band / Volume 365
Automated Magnetic Divertor Design for Optimal Power Exhaust
M. Blommaert (2017), xxiv, 220 pp
ISBN: 978-3-95806-216-0

Band / Volume 366
PEM-Elektrolyse-Systeme zur Anwendung in Power-to-Gas Anlagen
G. Tjarks (2017), IV, 135 pp
ISBN: 978-3-95806-217-7

Band / Volume 367
Fundamental Insights into the Radium Uptake into Barite by Atom Probe Tomography and Electron Microscopy
J. Weber (2017), IX, 160 pp
ISBN: 978-3-95806-220-7

Band / Volume 368
Entwicklung von elektronenleitenden Schutzschichten gegen die anodische Auflösung von Stromsammlern in neuartigen „Dual-Ionen"-Energiespeichern
G. Teucher (2017), VIII, 120 pp
ISBN: 978-3-95806-222-1

Band / Volume 369
Herstellung und Charakterisierung oxiddispersionsverstärkter Haftvermittlerschichten
J. Bergholz (2017), V, 133, II pp
ISBN: 978-3-95806-223-8

Band / Volume 370
Performance of Plasma Facing Materials under Thermal and Plasma Exposure
I. Steudel (2017), XVI, 150 pp
ISBN: 978-3-95806-226-9

Weitere ***Schriften des Verlags im Forschungszentrum Jülich*** unter
http://wwwzb1.fz-juelich.de/verlagextern1/index.asp

Energie & Umwelt /
Energy & Environment
Band / Volume 370
ISBN 978-3-95806-226-9

